UNIVERSITÀ DEGLI STUDI DI PALERMO

Industrial PhD program in

"Technology and Science for Human Health"

XXXIII Cycle

Department of Health Promotion, Mother and Child Care, Internal Medicine and Medical Specialties (PROMISE)

Micromechanical Modeling of Aortic Pathologies

CANDIDATE

Eng. Marzio Di Giuseppe

PHD COORDINATOR

Prof. Maurizio Leone

ACADEMIC TUTOR

Prof. Massimiliano Zingales

INDUSTRIAL TUTORS

Prof. Salvatore Pasta

Prof. Gaetano Burriesci

Summary

According to the reports of the World Health Organisation (WHO), cardiovascular diseases are the main cause of death worldwide. Specifically, arterial disease and tissue degeneration are the major reasons for cardiovascular failure and disability.

The human aorta is the biggest artery in the body and consists of three main parts: ascending aorta, aortic arch, and descending aorta. The walls of the arteries consist of three layers: the intima, media, and adventitia; each layer has a different physiological function and therefore distinct mechanical properties.

Ascending thoracic aortic aneurysm (ATAA) is a life-threatening cardiovascular disease leading to weakening of the aortic wall and permanent dilation associated with a high risk of adverse events [1]. To avoid aortic complications, the current clinical management of ATAA is mainly based on monitoring of aneurysms size as well as elective repair when aortic diameter enlarges upon a critical size. However, aortic diameter is not a sufficient predictor of the ATAA failure risk [2]. Alternative risk strategies are being developed by evaluating changes in the aortic stiffness of the ATAA wall [3-5].

Aortic stiffness is associated with progressive aortic dilatation and aneurysm formation as shown by imaging modalities [6, 7], computational analysis [4, 5, 8], and biomechanical studies [9, 10]. Ascending thoracic aortic aneurysm (ATAA) in patients with bicuspid aortic valve (BAV) can present an asymmetrical aortic dilatation compared with patients with tricuspid aortic valve (TAV).

Aortic dissection (AD) is typically described by a primary intimal tear on the aortic wall [11]. Dissections are commonly described as first propagating in the radial direction towards the medial layer, then within the media, or between the media and the adventitia, causing the layers of the aortic wall to separate[12]. A better understanding of the biomechanical effects preceding ADs initiation is essential for predicting adverse events on a patient-specific basis. The predisposition of thoracic aortic aneurysms (TAA) to ADs can be related to the degradation of biomechanically important constituents in the aortic wall of TAAs.

This project aimed to investigate and analyze the micromechanical mechanisms responsible for aortic failure/dissection through local mechanical characterization on *pathological tissues* coupled with advanced imaging techniques to collect qualitative and quantitative information about aortic microstructure and material parameters.

The first study (Chapter 3) aimed to characterize the mechanical properties and associated aortic tissue stiffness changes along the circumferential direction of aortic rings collected from surgically repaired patients with ATAA. Equibiaxial material testing was performed on tissue specimens extrapolated from all aortic quadrants (i.e. anterior, posterior, major, and minor curvature of the aorta), and then the tissue stiffness was quantified at both physiological and supra-physiological stress levels (i.e. 142 kPa and 242 kPa, respectively). Tissue stiffness revealed that the major curvature of BAV ATAA is statistically less stiff than the anterior quadrant and to that of the major curvature of TAV ATAA, suggesting a local weakening of the bicuspid aortic wall. Multiphoton imaging revealed local changes on elastic fiber networks. Material parameters for the Fung-type constitutive model were extracted.

The aim of the second study (Chapter 4) was to determine the most sensitive markers of local ATAA stiffness estimation with the hypothesis that direct measures of local ATAA stiffness could better detect the high-risk patients. The analysis was performed using the LESI (local extensional stiffness identification) methodology, recently established to quantify non-invasively local stiffness properties of ATAAs using electrocardiographic-gated computed tomography (ECG-gated CT) scans [4]. For 30 patients, the extensional stiffness was evaluated by the LESI methodology whilst computational flow analyses were also performed to derive hemodynamics markers such as the wall shear stress (WSS). A strong positive correlation was found between the extensional stiffness and the aortic pulse pressure. Interestingly, a significant positive correlation was also found between the extensional stiffness and patients' age for BAV ATAAs, but not for TAV ATAAs. No significant correlation was found between the extensional stiffness and WSS evaluated locally. There was no significant difference either in the extensional stiffness between BAV ATAAs and TAV ATAAs.

The goal of the third study (Chapter 5) was to develop a new methodology to measure strain fields in aortic tissues subjected to radial tensile loading, combining optical coherence tomography (OCT) and digital image correlation (DIC). Radial tensile tests were performed on 5 samples collected from a healthy porcine descending thoracic aorta and 2 samples collected from a human ascending thoracic aortic aneurysm. At each step of the radial tensile test, the OCT technique was used to acquire images of the sample presenting a speckle pattern generated by the optical signature of the tissue. The speckle pattern was used to quantify displacement and strain fields using DIC. Stress-strain data were also measured throughout the analyzed range. Results showed that strain commonly localizes very early during tensile tests, at the location where the crack onset occurs. Aneurysm samples showed a sharper localization than healthy porcine tissues.

Finally, the aim of the last study (Chapter 6) was to identify non-linear hereditariness material parameters in terms of fractional-order calculus of healthy aortic tissues. Fifty-five creep tests were performed on aortic tissues in the two main directions and at different load values. Average failure stress was obtained by tensile testing. Viscoelastic parameters obtained by power-law fitting of experimental data were extracted and compared.

Acknowledgments

First and foremost I am extremely grateful to my tutors, Prof. Salvatore Pasta and Prof. Massimiliano Zingales for their advice. I would also like to thank prof. Stephane Avril for hosting me at the Ecole des Mines de Saint-Étienne, it is his kind help and support that have made my study and life in France a wonderful time. I would like to thank all the members of ISMETT for providing the tissues and data requested for the development of this project. I would like to thank Aten Center for making equipment available and providing technical support for all the experimental activities. I would like to express my gratitude to my parents, sisters, family, and friends, for their continuous support and patience during my PhD study. Finally, thank you to my girlfriend Carola, for all her love and support; without hers tremendous understanding and encouragement in the past few years, it would have been impossible for me to complete my study.

Contents

List of Figures

List of Tables

Chapter 1

Introduction

1.1 Cardiovascular Disease

Cardiovascular disease (CVD) is the leading cause of death worldwide and is expected to account for more than 23 million deaths by 2030 [21]. Among these pathologies, aortic aneurysms (AA) and aortic dissections (AD) are rare but life-threatening events with poorly understood pathophysiologies. With the aging population, CVD prevalence is expected to increase and often co-exist with other diseases, leading to multi-morbidity. Major risk factors for CVD including obesity and diabetes are becoming more prevalent. CVD is also a heavy economic burden for both public and private institutions. By 2030, the total global cost of CVD is set to rise from approximately US$ 863 billion in 2010 to a staggering US$ 1,044 billion (World Heart Federation, 2020), as shown in Figure 1.
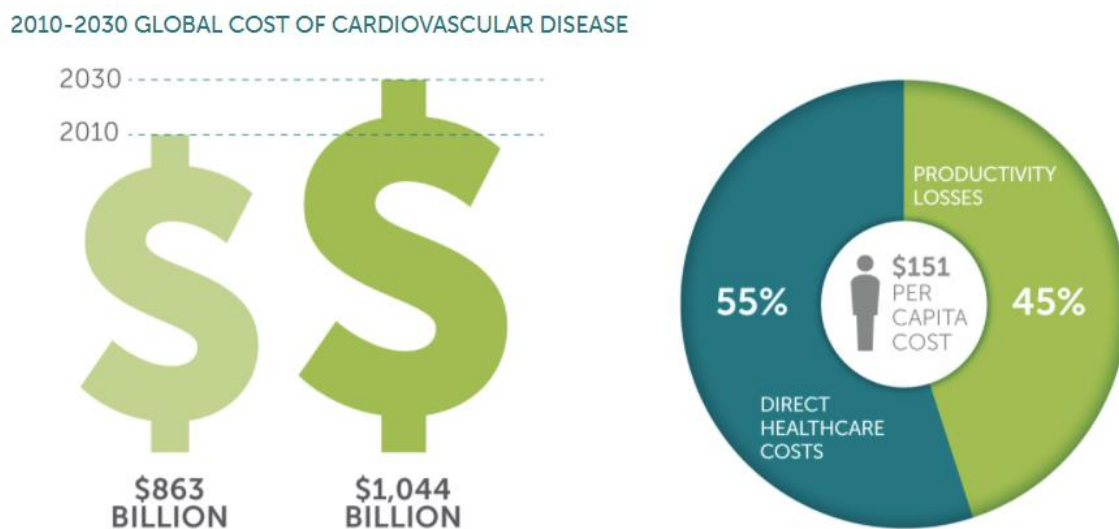
Figure 1 - The economic costs (Source: WEF/Harvard School of Public Health -The Global Economic Burden of Non-communicable Diseases).

The projected increase in healthcare costs is illustrated in Figure 2, which displays the total healthcare costs from CVD for the period through to 2020. By the end of the decade, the six countries combined will face CVD-related healthcare costs of €98.7 billion. Hence, there is a rise in per capita costs in each of the individual countries. Sweden and Germany face a per capita cost of €455 and €417, respectively. Costs will also rise in Italy (€297), the UK (€264), and France (€244).
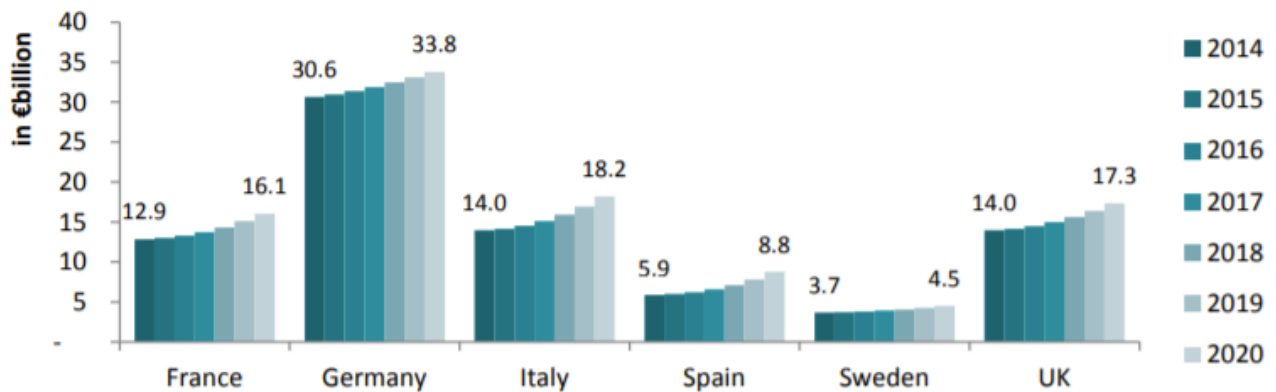
Figure 2 - Healthcare cost of CVD, forecast 2014-220, in €billion (Source: WEF/Harvard School of Public Health - The Global Economic Burden of Non-communicable Diseases).

Among the diseases affecting the cardiovascular system (CVS), it is possible to distinguish between those affecting the heart (i.e. cardiomyopathies, heart failure, heart valve diseases) and those affecting the aorta and the other vessels of the CVS (i.e. aortic aneurysm, aortic dissection, coronary artery diseases).

Here we present the main cardiovascular diseases:

- *Atherosclerosis* is characterized by a focal accumulation of lipids, extra cells, proteins, calcium, and necrotic debris within the intimal layer of arteries. In most cases, this accumulation causes a narrowing of the lumen (i.e., stenosis) which thereby compromises distal blood flow. One of the primary complications, however, is that atherosclerotic plaques can rupture and then clot - this can result in either the complete occlusion of the blood vessel or the shedding of a clot occluding a smaller, distal vessel. Consequences can include myocardial infarction (heart attack) or stroke (brain attack).

- *Heart Failure* is characterized by a marked decrease in cardiac output, increased venous pressures, or both; this results in elevated ventricular pressures that over distend the ventricles and thereby diminish their ability to pump blood. Heart failure is generally classified according to whether the right or left ventricle is affected. Left heart failure leads, for example, to pulmonary edema and hence breathlessness - sometimes called congestive heart failure.

- *Hypertension* is defined as the persistent elevation of blood pressure. Normal systemic pressure is ≈ 120/80 mmHg (systolic/diastolic) and systemic hypertension is generally defined as pressures above 160/90 mmHg. Hypertension may not have a known cause (called essential or idiopathic) or it may result from other diseases (then called secondary hypertension), such as renal, endocrine, or central nervous system diseases. The primary

importance of hypertension is that it is a major risk factor for other, potentially fatal, diseases, including aneurysms, end-stage renal disease, stroke, sudden cardiac death, etc.

- *Myocardial infarction*, or heart attack, is defined as the death of myocardium (necrosis) due to a lack of oxygen (ischemia). If one survives a heart attack, the necrotic tissue is generally removed and replaced with a 'collagen patch', which in some cases may form an aneurysm. As noted above, atherosclerosis is the most common cause of heart attacks.

- *Stroke*, strictly speaking, is any sudden or severe attack, as, for example, a sun-stroke or heat-stroke. Commonly, however, by the term stroke, we imply the death of a portion of the brain due to the lack of oxygen, and thus it is sometimes referred to as a brain attack in analogy with a heart attack. As noted above, strokes are often caused by the rupture and clotting of an atherosclerotic plaque. In addition, however, strokes may also be caused by the shedding of an embolus from the heart or a proximal vessel or by the rupture of an intracranial malformation or aneurysm.

- *Valvular heart disease* is any cardiovascular disease process involving one or more of the four valves of the heart shown in Figure 3. Diseases of the aortic and mitral valve are more prevalent than the disease of the pulmonary or tricuspid valve due to the higher pressures the left heart experiences. These conditions occur largely as a consequence of aging, but may also be the result of congenital abnormalities or a specific disease. Stenosis and insufficiency/regurgitation represent the dominant functional and anatomic consequences associated with valvular heart disease. The valvular disease often necessitates surgical replacement of the associated heart valves; prosthetic heart valves are among the most successful implants in cardiovascular surgery. The most common valvular disease is the *bicuspid aortic valve* (BAV) in which two of the leaflets of the aortic valve are fused. BAV is the most common cause of heart disease present at birth and affects about 1.3% of adults [20].

- *Aneurysms* are focal dilatations resulting from a local weakening of a pressure-distended organ. Within the vasculature, the two most common forms are abdominal aortic aneurysms (AAA), ascending thoracic aortic aneurysm (ATAA), and intracranial saccular aneurysms. These types of diseases have very different etiologies, the former often related to atherosclerosis and the latter not; both generally involve the proteolytic breakdown of portions of the extracellular matrix.
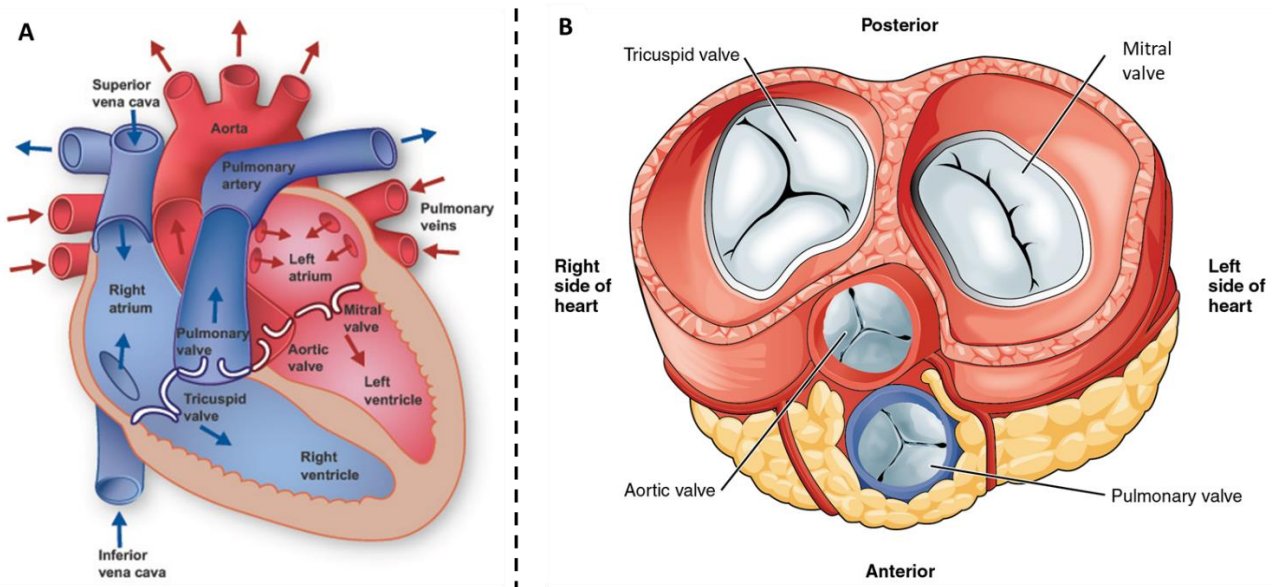
Figure 3 – Anatomical representation of (A) longitudinal section of the heart (from www.texasheart.org) and (B) circumferential section of the heart showing heart valves (from www.aatb.org).

1.2 Soft tissues

Biological tissues are roughly divided into (i) hard tissues like bone and tooth, and (ii) soft tissues such as skin, muscle, blood vessel, and lung. Hard tissues contain minerals, whereas soft tissues do not. Because of this, they have very different mechanical properties.

One of the major differences in mechanical properties is that soft tissues are much more deformable than hard tissues. Therefore, infinitesimal deformation theories that are applied to metals and hard plastics cannot be used for soft tissues; instead, finite (large) deformation theories that are useful for rubber elasticity are often used to describe the mechanical behavior of soft tissues [22]. This section deals with the basic mechanical properties of biological soft tissues and their mathematical formulation, including several biomechanical features unique to soft tissues.

Soft connective tissues of our body are complex fiber-reinforced composite structures. Their mechanical behavior is strongly influenced by the concentration and structural arrangement of constituents such as collagen and elastin, the hydrated matrix of proteoglycans (PGs), and the topographical site and respective function in the organism.

Collagen is a very protein important for vertebrate physiology. It is a macromolecule with a length of about 280 nm. The rod-like shape of the collagen molecule comes from three polypeptide chains which are composed in a right-handed triple-helical conformation. Most of the collagen molecule consists of three amino acids: glycine (33%), which enhances the stability of the molecule, proline

4

(15%), and hydroxyproline (15%). Collagen molecules are linked to each other by covalent bonds building collagen fibrils, as illustrated in Figure 4. Depending on the primary function and the requirement of the strength of the tissue the diameter of collagen fibrils varies (the order of magnitude is 1.5 nm; see [23]). Collagen appears as concentrically arranged fibers in the structure of blood vessels. More than 12 types of collagen have been identified [24]. The most common collagen is type I, which can be isolated from any tissue. It is the major constituent in blood vessels. The intramolecular crosslinks of collagen give strength to the connective tissues, which varies with age, pathology, etc. Collagen fibers represent the main load-carrying elements of arterial walls that render the material properties anisotropic.
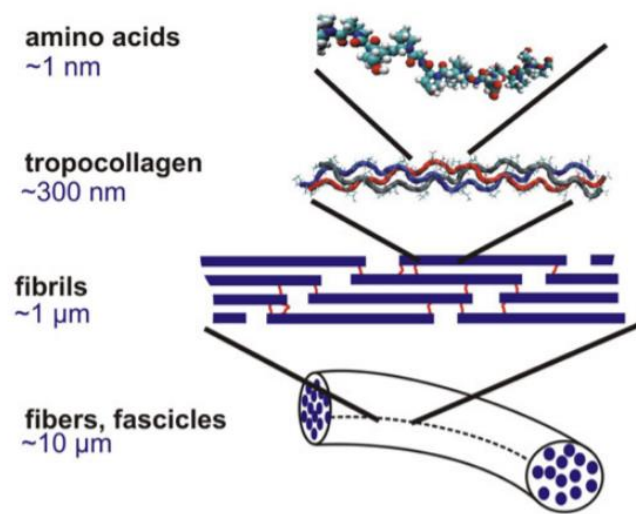
Figure 4 - Schematic view of the hierarchical features of collagen (from [13]).

Elastin is another major component of certain soft tissues, such as arterial walls and ligaments. It is a protein, which is a major constituent of the extracellular matrix of connective tissue. It is present as thin strands in soft tissues. The long flexible elastin molecules build up a three-dimensional (rubber-like) network, shown in Figure 5, which may be stretched to about 2.5 of the initial length of the unloaded configuration. In contrast to collagen fibers, this network does not exhibit a pronounced hierarchical organization. As for collagen, 33% of the total amino acids of elastin consist of glycine. However, the proline and hydroxyproline contents are much lower than in collagen molecules. The mechanical behavior of elastin may be explained within the concept of entropic elasticity. Elasticity arises through entropic straightening of the chains, i.e. a decrease of entropy, or an increase of internal energy (see, for example [25]). Elastin is essentially a linearly elastic material (tested for the ligamentum nuchae of cattle). It displays very small relaxation effects (larger for collagen).

For a more detailed account of the different mechanical characteristics, the structure (distribution and orientation) of the interrelated arterial components, the morphological structure, and the overall functioning of the blood vessel refer to [26], and [27].
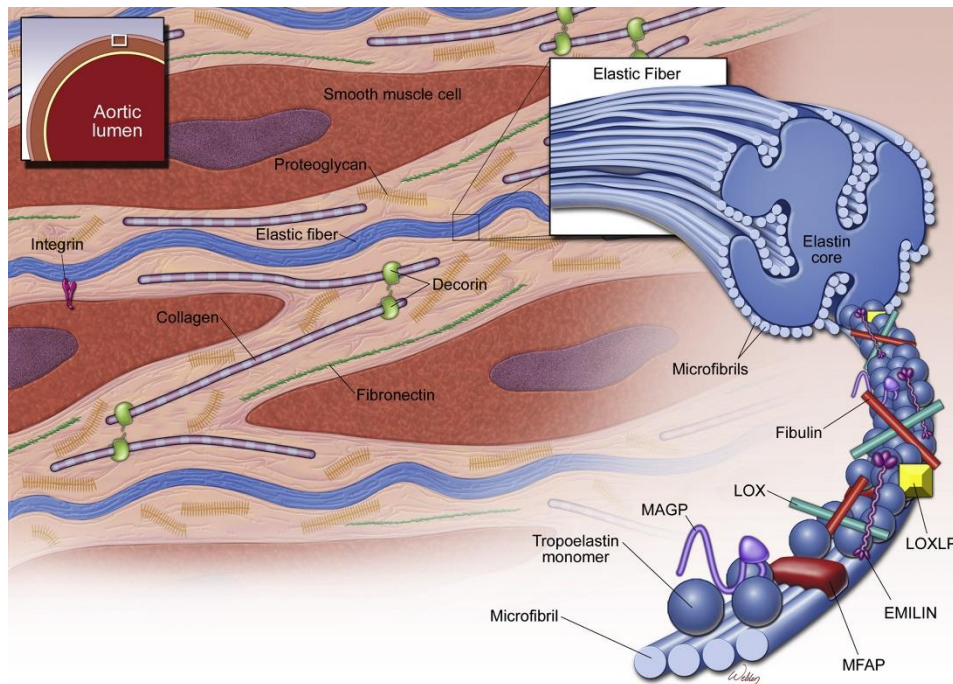
Figure 5 - Elastic fiber structure in the medial layer of the aorta (from [14]).

Proteoglycans (PGs) consist of glycosaminoglycans (GAGs) that are linked to a core protein as shown in Figure 6 and are mainly found in the extracellular matrix (ECM), although some PGs extend across the cell membrane or are directly attached to it by anchors [28]. GAGs are negatively charged and hydrophilic unbranched polysaccharide chains composed of repeating disaccharide units. They can be divided into four groups by their sugars and links between the sugars: (i) chondroitin sulfate and dermatan sulfate, (ii) heparan sulfate, (iii) keratan sulfate, and (iv) hyaluronan (also known as hyaluronic acid or hyaluronate). PGs take part in ECM remodeling and cell adhesion-migration-proliferation by interacting with or functioning as cell surface receptors to growth factors, matrix remodeling enzymes, and other ECM components [29]. PGs secreted by vascular endothelial cells can serve as structural organizers of the basal lamina by attaching to the other constituents or contribute to the selective filtration of the basal lamina. Proteoglycans can either promote or prevent processes depending on the type of cells they are interacting with and the environment [29].
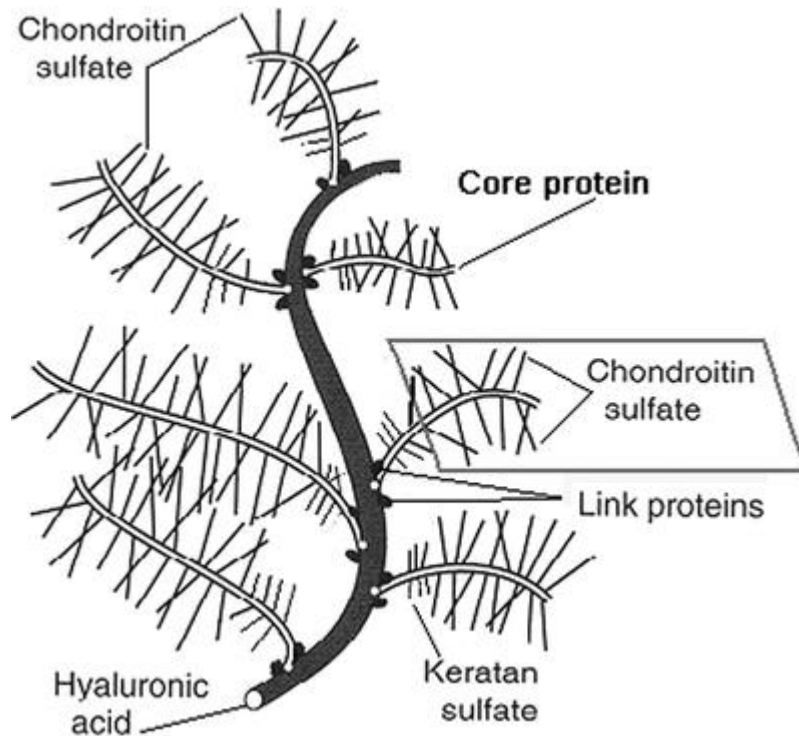
Figure 6 - Sketch depicting the structure of a large proteoglycan aggregate consisting of keratan sulfate and chondroitin sulfate attached to the core protein, for example, aggrecan or versican, that are attached to hyaluronan molecule via linking proteins [15].

1.3 Healthy aortic wall

The aorta, the main artery of the human circulatory system, carries oxygenated blood from the heart to the periphery of the human body. The aorta is spanned by a unidirectional blood flow ejected by the left ventricle (LV); flow direction is maintained constant by the aortic valve, which opens and closes allowing blood flow from the LV to the ascending aorta ad avoiding the blood backflow inside the heart.

The aorta can be divided into different parts, including the aortic root, ascending aorta, aortic arch, and descending aorta. The aortic root is directly connected to the left ventricle of the heart, and it comprises the aortic valve, interleaflet triangles, sinuses of Valsalva, and sino-tubular junction [30], as illustrated in Figure 7. The sinuses (right, left, and non-coronary) are aortic root bulges connected to the three aortic valve leaflets and the sino-tubular junction. The aortic valve leaflets separate the LV volume to aortic volume and with their motion, allow the blood to flow from the LV to the aorta, during systole and prevent the backflow of blood into the LV during diastole when the pressure inside the aorta becomes higher than the intra-ventricular pressure.
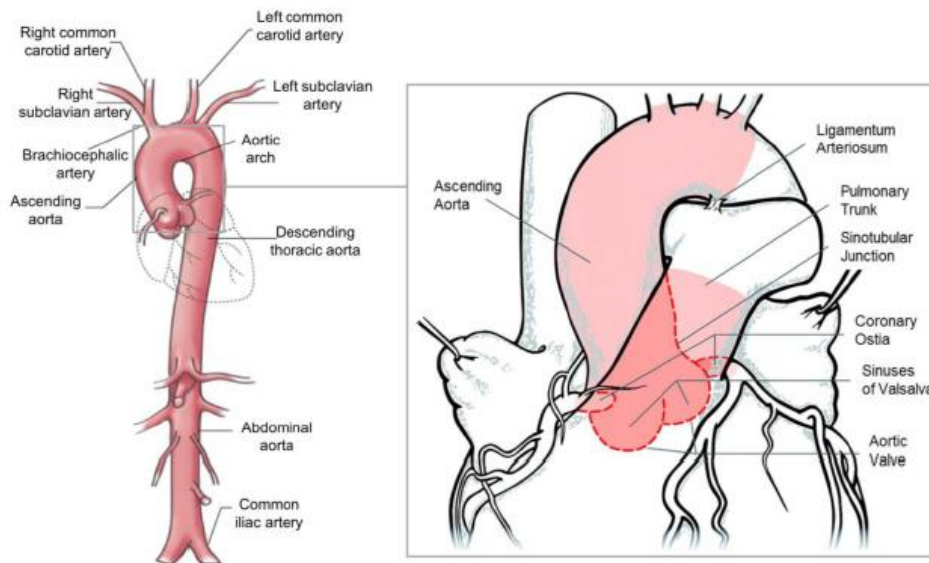
Figure 7 – The structure of the human aorta (modified from [16]).

Microscopic examination has revealed that arterial tissue is heterogeneous and consists of three main layers: intima (the innermost layer), media, and adventitia (the outermost layer), as illustrated in Figure 8. The mechanical properties of arterial walls are strongly influenced by the concentration and structural arrangement of constituents such as collagen and elastin, the hydrated matrix of proteoglycans, and the topographical site and respective function in the organism as shown in Figure 9.
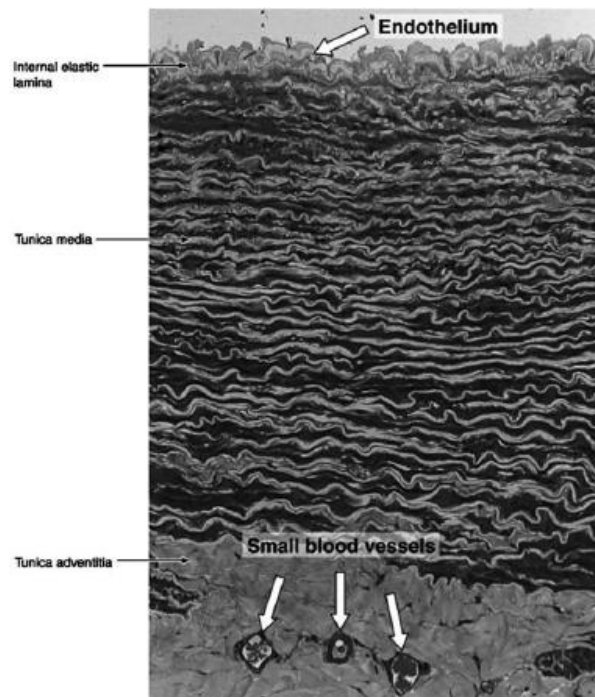
Figure 8 - Transverse section of the wall of a large elastic artery demonstrating the well-developed tunica media containing elastic lamellae (from [31]).
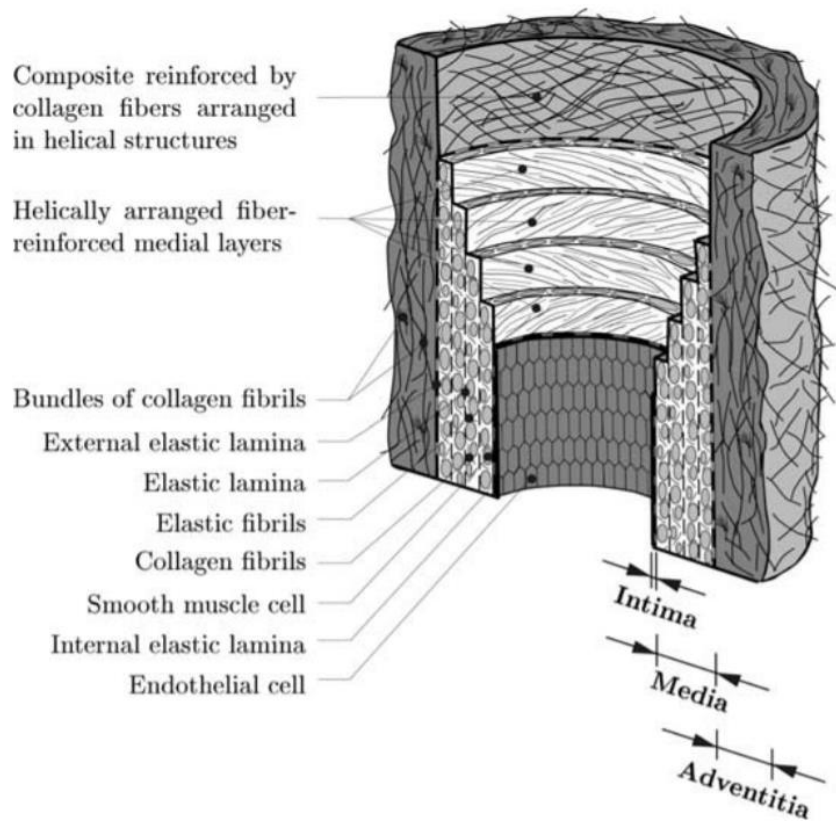
Figure 9 - Schematic representation of an elastic artery (from [17]).

- The <u>tunica intima</u> is the innermost layer of the artery. It consists of a single layer of endothelial cells and a portion of connective tissue. In general, the endothelial cells tend to be elongated in the direction of the blood flow. It acts as a semipermeable membrane, through which nutrients and chemical signals can reach the cells in the vessel wall from the bloodstream. The intima has also a key role in regulating the active response of the vessel: as a membrane, it is the conduit through which pressure regulating agents reach the media. Additionally, it is known that the intima produces NO (nitric oxide), which relaxes smooth muscle cells in the media and thus helps control the vascular tone. Despite its great functional importance, due to its small thickness ($\sim$80 nm) in young arteries, the intima is usually neglected when considering the different layer contributions to the global mechanical resistance of the vessel wall. The mechanical contribution of the intima may become significant for aged arteries (arteriosclerosis) (the intima becomes thicker and stiffer); see, for example [32]. In addition, it is important to note that pathological changes of the intimal components (atherosclerosis) are associated with significant alterations in the mechanical properties of arterial walls, differing significantly from those of healthy arteries.

- The <u>tunica media</u> is the middle layer of the artery and consists of a complex three-dimensional network of smooth muscle cells, elastin, and collagen fibrils. It is responsible for aortic behavior. The media is separated from the intima and adventitia by the so-called internal elastic lamina and

external elastic lamina (absent in cerebral blood vessels), respectively. In muscular arteries, these laminae appear as prominent structures, whereas in elastic arteries they are hardly distinguishable from the regular elastic laminae. The close interconnection between the elastic and collagen fibrils, elastic laminae, and smooth muscle cells together constitute a continuous fibrous helix. The helix has a small pitch so that the smooth muscle cells in the media are almost circumferentially oriented. This structured arrangement gives the media high strength, resilience, and the ability to resist loads in both the longitudinal and circumferential directions. From the mechanical perspective, the media is the most significant layer in a young healthy artery. Due to the high content of smooth muscle cells, it is the media that is believed to be mainly responsible for the viscoelastic behavior of an arterial segment.

- The adventitia is the outermost layer of the artery. It consists of a dense network of type I collagen fibers with scattered fibroblasts, elastin, and nerves. The adventitia is surrounded continuously by loose connective tissue. The fibers of the adventitia confirming the hypothesis that the adventitia serves as a protective sheath, preventing rupture of the vessel due to an acute increase in pressure. The wavy collagen fibrils are arranged in helical structures and serve to reinforce the wall. They contribute significantly to the stability and strength of the arterial wall. The adventitia is much less stiff in the load-free configuration and at low pressures than the media. However, at higher levels of pressure, the collagen fibers reach their straightened lengths and the adventitia changes to a stiff 'jacket-like tube which prevents the artery from overstretching and rupture.

1.4 Aortic Aneurysm

The average normal aortic diameter lies between 20 and 25 mm [33] but can reach up to 35 mm and still considered normal [34]. Typically, an ascending aorta diameter equal to or greater than 40 mm indicates dilatation, while a diameter equal to or exceeding 1.5 times the normal expected diameter is considered an aneurysm [14, 28]. According to the morphology, aneurysms can be either saccular or fusiform, the latter being more common in the aorta. They can also be classified according to the aortic segment involvement as thoracic, thoracic- abdominal, or abdominal as shown in Figure 10.

A thoracic aortic aneurysm is asymptomatic in the vast majority of patients, usually being diagnosed via an imaging study carried out for another purpose (echocardiogram (ECHO) or CT scan). In the few patients who do have premonitory symptoms, these usually take the form of chest pain; if no other causes for chest pain are found, the pain can fairly be presumed to originate from the thoracic aneurysm. Ascending thoracic aortic aneurysms are perceived as a 'silent killer' with 95% of the

incidents not diagnosed until complications such as dissection or rupture occur [18]. Possible causes or symptoms for ATAA development are shown in Figure 11. ATAAs are particularly lethal with an estimated mortality rate as high as 62% in patients with ATAAs larger the 6 cm [35].
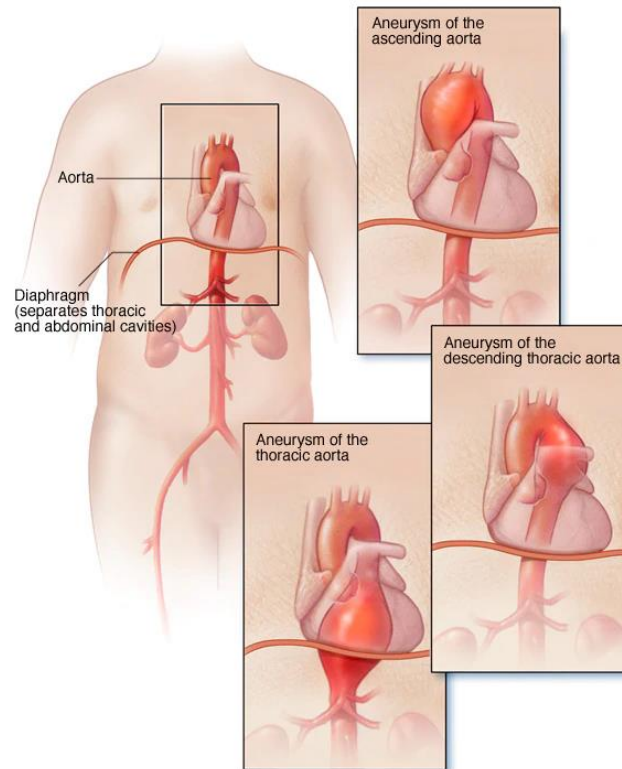
Figure 10 – Representation of various types of aortic aneurysm (Adapted from https://www.mayoclinic.org).

The aortic aneurysm occurs when the arterial wall loses its structural integrity due to medial degeneration and gives way to the distending forces of the pulsatile intraluminal pressure (as in Marfan syndrome) or excessive stress (hypertension). The formation of the aortic aneurysm is associated with the local production of enzymes and matrix metalloproteinases (MMPs), which are capable of degrading the extracellular matrix of the aortic wall, including elastic fibers and interstitial collagens. This results in medial degeneration, characterized by elastic fiber loss from the medial layer, loss of vascular smooth muscle cells, and proteoglycans deposition. ATAAs are associated with several predisposing factors, such as the presence of a congenital defect like the bicuspid aortic valve (BAV), or the presence of connective tissue disorder such as Marfan or Ehlers syndrome.
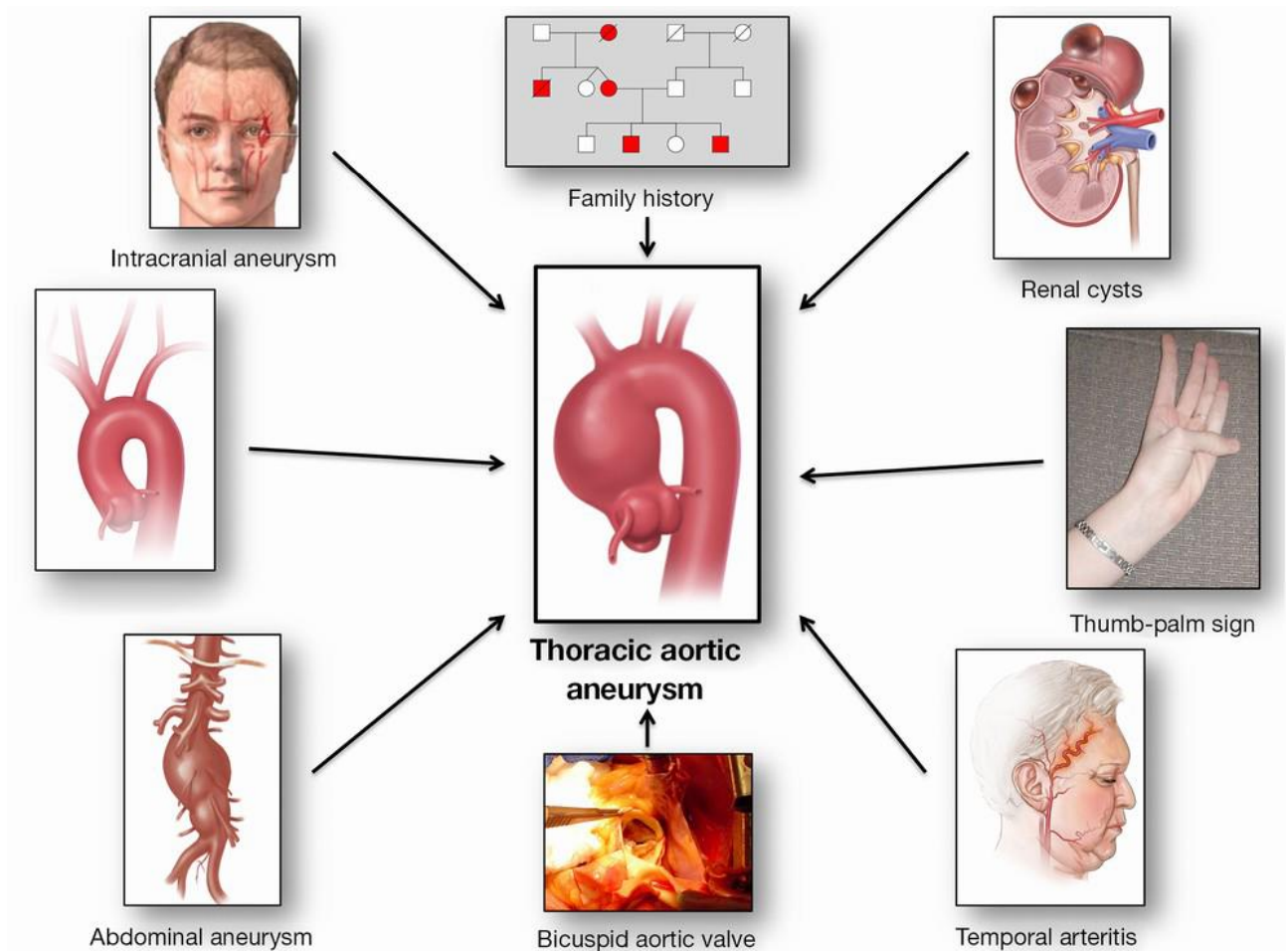
Figure 11 - Paradigm of "Guilt by Association" for the detection of silent thoracic aortic aneurysms [18].

The choice of the best treatment for ATAA is an ongoing debate since the physician has to deal with the risk of leaving the aneurysm untreated and the risk connected to treat the aneurysms surgically. Elective surgical procedures are often contraindicated due to a high risk connected to surgery and patients' general condition; adversely, if left untreated, ATAAs may suddenly rupture or dissect leading to a mortality rate as high as 96%. Understanding when these complications may happen is the most critical part of the clinical decision process about elective surgical repair. Currently, the gold standard to evaluate the timing of operation for patients with ATAA is based on the maximum aortic diameter criterion suggested by [36]. This criterion prescribes that if AoAs diameter is above 6 centimeters, for both ATAA and AAA, an elective surgical procedure should be operated. The clinical decision is also supported by the evaluation of aneurysm growth rate; it has been reported an average aneurysm growth of 0.1cm/year for TAAs, with an average of 0.19 cm/year for descending thoracic aortic aneurysms and 0.07 cm/year for ATAAs [37].

Despite the diameter criterion is widely used in clinical practice worldwide, aneurysm rupture with a diameter value below 6 centimeters is not infrequent. Moreover, following the European guidelines, ATAA associated with BAV should be replaced at 5.0 cm if ATAA grows more than 0.2 cm/year or in presence of risk factors like hypertension [37]. Della Corte et al. [38] proposed a classification scheme of the dilated aorta in which the aortas were divided on the base of their dilatation pattern (i.e. non-dilated, ascending phenotype, and root phenotype). Another classification proposed by Schaefer et al. [19] classifies the aorta into three groups (i.e. Type N, Type A, and Type E) according to the commonly observed shapes of aortic dilatations, shown in Figure 12.
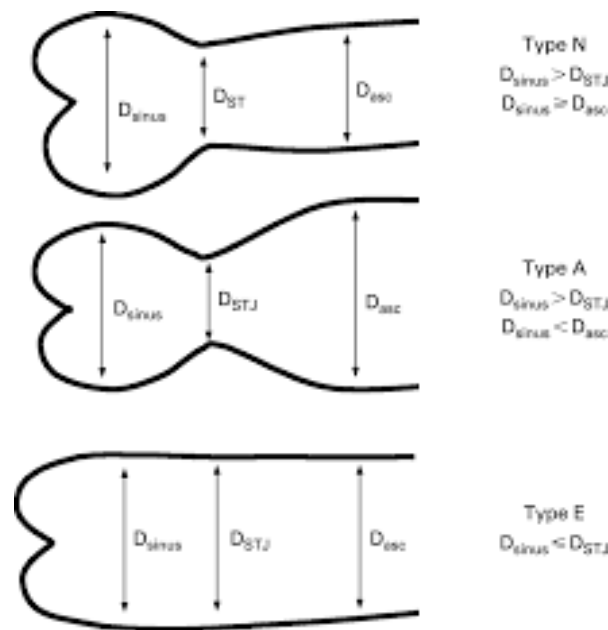
Figure 12 – Aortic shapes. Schematic of three aortic shapes that are all-inclusive. Dsinus, diameter at the sinus of Valsalva; DSTJ, diameter at the sino-tubular junction; Dasc, diameter in the mid ascending aorta [19].

Several attempts have been made to establish if the mechanism based on ATAA is genetic or hemodynamic in origin. Both theories are illustrated in Figure 13. The genetics theory supports the idea that ATAA is a direct consequence of aortic wall weakness and that this weakness is due to abnormal regulatory pathways of extracellular matrix degeneration within the aortic media. This idea is supported by the observation that BAV and TAV had histological and molecular differences. On the other hand, the hemodynamic theory is based on the idea that abnormal flows inside the aorta, like those introduced by BAV, may impose high loads on the aortic wall that promote aneurysm development and growth. This theory is supported by the observation that different phenotype of BAV leads to different aortic dimension. However, it is possible to speculate that both hemodynamic and genetic may be responsible for aneurysm growth.
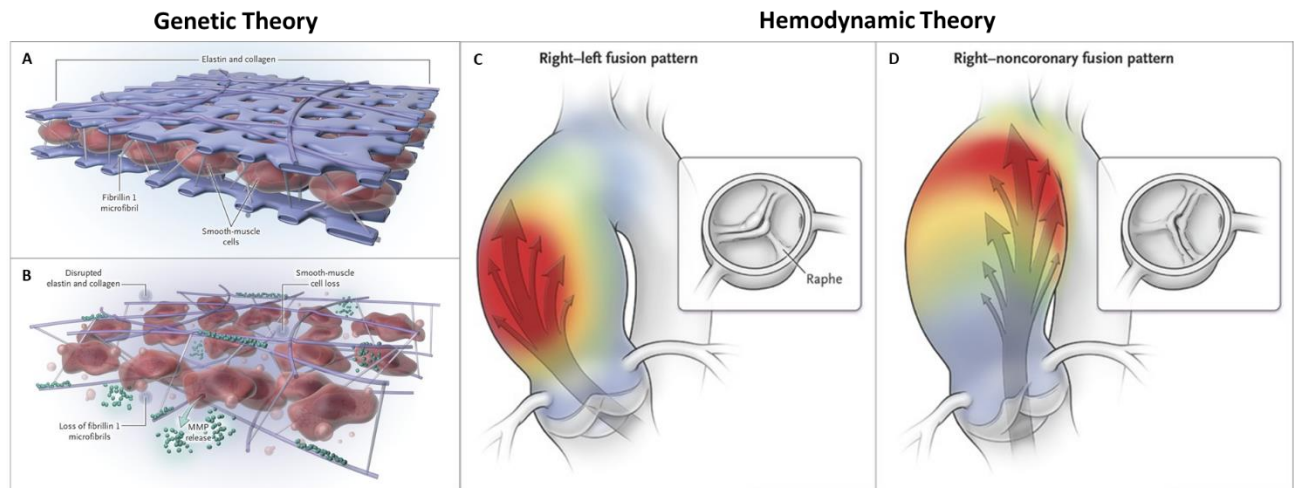
Figure 13 – Representation of the genetic and hemodynamic theory based on ascending thoracic aortic aneurysms [20].

1.5 Arterial Mechanics

The mechanical behavior of blood vessels has been a subject of research for over 100 years, with the first report of Roy [39] dating back to the late 19th century.

1.5.1 Residual Stresses

A salient characteristic of the vascular mechanical behavior is the existence of residual stresses in an otherwise unloaded vessel. If an arterial ring is cut radially it springs open and an axial strip excised from the artery bends away from its vessel axis. These observations expose the existence of residual stresses in the wall, both in the axial and circumferential directions. It was Bergel in 1960 [40], who first reported about residual stresses in arteries. The fact that the vascular ring opens when cut radially implies that the luminal part is under compression, while the external part is under tension. In vivo, however, the internal pressure equilibrates these stresses, and the whole wall supports a more uniform level of stress throughout the radius [1, 18]. It has been demonstrated that elastin is largely responsible for residual stress [41]. These effects are manifested externally, in that the internal elastic lamina is wavier in histological samples of the load-free state than those of the stress-free configuration or under in vivo conditions [42]. The existence of residual stresses immediately suggests the question about a stress-free configuration and its measure. Chuong and Fung [43] suggest the opening angle of the vascular sample as the only measure to quantify the residual circumferential deformation of the vessel. This is a popular measure due to its simplicity and is routinely found in the literature. Besides, it has been shown that a single cut releases most of the residual stresses, and that the opening angle is relatively insensitive to the exact location [35,

36, 38]. Contrasting these findings, it has been shown that the opening angle is different for each layer [30, 38]. Matsumoto et al. [44] have found that even in this macroscopic stress-free configuration, the lamellar unit in the aorta is subject to residual stresses at the microscopic level. All these results are mutually compatible if the stress-free configuration is considered as a boundary value problem: if the boundary conditions change (for example, the vessel layers are separated), the equilibrium configuration will change accordingly.

1.5.2 Anisotropy

One fundamental characteristic of the soft tissue is its marked anisotropy, indicated by different behavior in the circumferential and axial directions. Most researchers agree that the mechanical response of arterial tissue is anisotropic with respect to the load-free configuration, based on the comparison of the material parameters associated with circumferential and axial directions [20, 39, 40, 45].

1.5.3 Incompressibility, Viscoelasticity, and Pseudo elasticity

Most biological soft tissues have a water content of more than 70 – 80% justifying the usual assumption that it is incompressible. Therefore, they hardly change their volume (isovolumetric) even if the load is applied, and they are almost incompressible. The incompressibility assumption is applied to most biological soft tissues [43]). The incompressibility assumption is very important in the formulation of constitutive laws for soft tissues because the sum of all principal (logarithmic) strains is always zero.

1.5.4 Mechanical Behavior

The tensile response of soft tissue is nonlinear stiffening and tensile strength depends on the strain rate. In contrast to hard tissues, soft tissues may undergo large deformations. Some soft tissues show viscoelastic behavior (relaxation and/or creep), which has been associated with the shear interaction of collagen with the matrix of proteoglycans [46] (the matrix provides viscous lubrication between collagen fibrils).

Figure 14 shows a schematic diagram of a typical J-shaped stress-strain (traction) curve for soft tissue. In detail, the curve describes the stress-strain behavior for the skin which is representative of the mechanical behavior of many soft connective tissues (collagenosis).
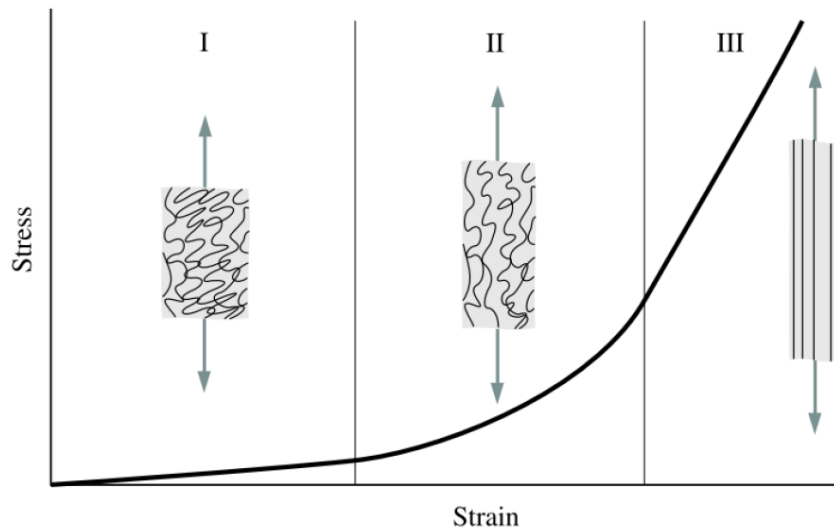
Figure 14 – Schematic diagram of a typical (tensile) stress-strain curve for skin showing the associated collagen fiber morphology.

This form, representative of many soft tissues, differs significantly from stress-strain curves of hard tissues or other types of (engineering) materials. Also, Figure 14 shows how the collagen fibers straighten with increasing stress. The deformation behavior for skin may be studied in three phases I, II, and III:

▪ Phase I. In the absence of loading the collagen fibers, which are woven into the rhombic-shaped pattern, are in relaxed conditions and appear wavy and crimped. Unstretched tissue behaves approximately isotropically. Initially, low stress is required to achieve large deformations of the individual collagen fibers without requiring a stretch of the fibers. In phase I the tissue behaves like a very soft (isotropic) rubber sheet, and the elastin fibers are mainly responsible for the stretching mechanism. The stress-strain relation is approximately linear, the elastic modulus of tissue in phase I is low (0.1-2 MPa).

▪ Phase II. In phase II, as the load is increased, the collagen fibers tend to line up with the load direction and bear loads. The crimped collagen fibers gradually elongate and they interact with the hydrated matrix. With deformation, the crimp angle in collagen fibrils leads to a sequential uncrimping of fibrils.

▪ Phase III. In phase III, at high tensile stresses, the crimp patterns disappear and the collagen fibers become straighter. They are primarily aligned with one another in the direction in which the load is applied. The straightened collagen fibers resist the load strongly and the tissue

becomes stiff at higher stresses. The stress-strain relation becomes linear again. Beyond the third phase, the ultimate tensile strength is reached and fibers begin to break.

The mechanical properties of soft tissues strongly depend on topography, risk factors, age, species, strain rate, physical and chemical environmental factors such as temperature, osmotic pressure, pH. The material properties are strongly related to the quality and completeness of experimental data, which come from in vivo or in vitro tests having the aim of mimicking real loading conditions. Therefore, presenting specific values for the ultimate tensile strength and strain of a specific tissue is a difficult task.

Table 1 attempts to present ranges of values of mechanical properties and collagen/elastin contents (% dry weight) in some representative organs mainly consisting of soft connective tissues.

Table 1 – Mechanical properties [47] and associated biochemical data of some representative organs mainly consisting of soft connective tissues.

Material	Ultimate tensile strength [Mpa]	Ultimate tensile strain [%]	Collagen (% dry weight)	Elastin (% dry weight)
Tendon	\	10-15	75 - 85	< 3
Ligament	50-100	10-15	70-80	ott-15
Aorta	0.3 – 0.8	50-100	25-35	40-50
Skin	1-20	30-70	60-80	05-10
Articular Cartilage	9 – 40	60 -120	40-70	-

This PhD project aimed to investigate and analyze the micromechanical mechanism responsible for aortic failure/dissection through local mechanical characterization on pathological tissues. This approach was coupled with advanced imaging and numerical techniques to collect qualitative and quantitative information about aortic tissue's microstructure.

Chapter II

Background Knowledge

2.1 Remarks on Continuum Mechanics

Continuum mechanics is the branch of mechanics dealing with the analysis of the kinematics and the mechanical behaviors of materials in terms of strain and stress. The purpose of continuum mechanics is to provide a macroscopic model for fluids, solids, and organized structures. A fundamental assumption is the "continuous medium hypothesis": namely, that the real space occupied by a fluid or a solid can be approximately regarded as continuous without voids between the particles of matter. In the following section, a short introduction to continuum mechanics is given based on the work of Holzapfel et al.[25], which does help in explaining the theories in a clear and intelligible way. For further information and reading material concerning the topics covered, the works from Cowin and Doty [48] and Ogden [49] are warmly suggested.

Macroscopic systems often can be described successfully with a continuum approach (macroscopic approach). The fundamental assumption therein states that a body, denoted by $\mathfrak{b}$, may be viewed as having a continuous (or a piecewise continuous) distribution of matter in time and space. The body is imagined as being a composition of a (continuous) set of particles (or continuum particles or material points), represented by $P \in \mathfrak{b}$ as shown in Figure 15.

It is important to mention that the notion "particle" (or 'continuum particle' or 'material point') refers to a part of a body, which does not imply any association with the point mass of Newtonian or the discrete particle of the atomistic theory. A typical continuum particle is an accumulation of a large. A typical continuum particle is an accumulation of a large number of molecules, yet is small enough to be considered as a particle. The behavior of a continuum particle is a result of the collective behavior of all the molecules constituting that particle.

In the field of continuum mechanics, it is defined a continuum body $\mathfrak{b}$ with particle $P \in \mathfrak{b}$ which is embedded in the three-dimensional Euclidean space at a given time t, as indicated in Figure 15. To characterize this body It is defined a rectangular coordinate system with origin 0. While the continuum body $\mathfrak{b}$ moves in space from one instant of time to another, it occupies a continuous sequence of geometrical regions denoted by $\Omega_0,\ldots, \Omega$. As a result, every particle P of $\mathfrak{b}$ corresponds to a so-called geometrical point owning a position in regions $\Omega_0,\ldots, \Omega$. Region $\Omega 0$ corresponds at the undeformed configuration of the body $\mathfrak{b}$ and at initial time t=0 is referred to as the initial

configuration. Assuming that the region Ω_0 of space moves to a new region Ω which is occupied by the continuum body ϐ at a subsequent time t>0. The configuration of ϐ at t is the so-called deformed configuration.
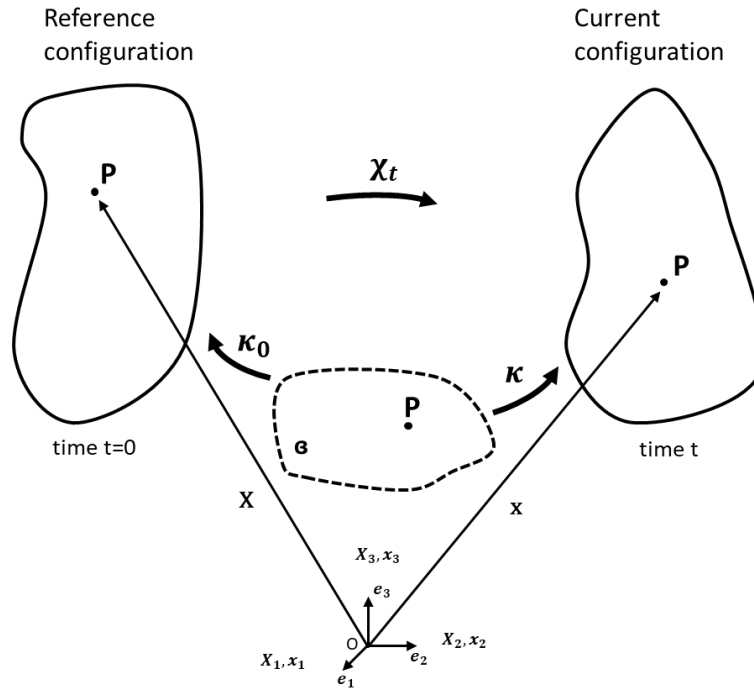
Figure 15 – Configuration and motion of a continuum body.

By Assuming that the map $X=k_0(P,t)$ is a one-to-one correspondence between a particle P∈ϐ and the point $X \in \Omega_0$ that ϐ occupies at the given instant of time t=0. Moreover, let the map к act on ϐ to produce the region Ω at time t. The place $x=\kappa(P,t)$ that the particle P (evidently identified with X and t) occupies at t is described by (in symbolic and index notation):

$$x = k[k_0^{-1}(X,t)] = \chi(X,t) \tag{1}$$

for all $X \in \Omega_0$ and for all times t. In Eq. 1, χ is a vector field that specifies the place x of X for all fixed t and is called the motion of the body ϐ. The motion χ carries points X located at Ω_0 to places x in the current configuration Ω. Assuming subsequently that χ possesses continuous derivatives with respect to space and time.

The motion χ is assumed to be uniquely invertible. Consider (x,t), the position of point X, which is associated with the place x at time t, is specified uniquely be Eq.1 as:

$$X = \chi^{-1}(x,t) \tag{2}$$

with the inverse motion denoted by χ^{-1}. For a given time t, the inverse motion Eq.2 carries points located at Ω to points in the reference configuration Ω_0. In Eq.1 and Eq.2, respectively, the pairs (X, t) and (x, t) denoted independent variables.

A motion χ of a body will generally change its shape, position, and orientation. A continuum body that can change its shape is said to be deformable. By a deformation χ (or inverse deformation χ^{-1}) of a body which is meant a motion (or inverse motion) of a body that is independent of time.

2.1.1 Deformation Gradient and Strain Tensor

In continuum mechanics, the matter is assumed to be continuously distributed. Therefore, multiple phases can have coinciding positions. To describe the deformation of an arbitrary body with volume Ω and surface $\partial\Omega$, a tensor called deformation gradient **F** is introduced. Thus, we distinguish between the referential (undeformed) $\Omega0$ and the current (deformed) Ω configuration with coordinates X(t) and x (X;t), respectively. The deformation gradient is given by:

$$\boldsymbol{F} = \frac{\delta\chi(\boldsymbol{X},t)}{\delta\boldsymbol{X}} = Grad(\boldsymbol{x}(\boldsymbol{X},t)) \tag{3}$$

where Grad **x**(**X**, t) represents the gradient operator applied to the map χ(**X,** t).

The quantity **F** is crucial in nonlinear continuum mechanics and is a primary measure of deformation, called the deformation gradient. In general, **F** has nine components, and it characterizes the behavior of motion in the neighborhood of a point. It is well known that the determinant of **F**, commonly noted J, represents the volume change between the reference and the current configurations:

$$\boldsymbol{J} = \det(\boldsymbol{F}) = \frac{dV}{dV_0} > 0 \tag{4}$$

In Eq. 4, dV and dV_0 denote infinitesimal volume elements defined in the reference and current configurations called material (or undeformed) and spatial (or deformed) volume elements, respectively. Further, it can be assumed that the volume is a continuous (or at least a piecewise continuous) function of continuum particles so that $dV=dX_1dX_2dX_3$ and $dv=dx_1dx_2dx_3$ (continuum idealization). The deformation gradient can be further decomposed into two tensors, one related to pure rotation and another to pure deformation. This decomposition, defined as polar decomposition, can be written as:

$$\boldsymbol{F} = \boldsymbol{RU} = \boldsymbol{VR} \tag{5}$$

Here, $R \, \epsilon Orth^+$ is a unique rotation tensor (with the property that $R^T R = R R^T = I$), while U is the right stretch tensor and V is the left stretch tensor. The two stretch tensors, both positive definite and symmetric (i.e. $U = U^T$ and $V = V^T$) and represent a pure deformation. Moreover, they can be diagonalized, and their spectral decomposition is given by:

$$U = \lambda_1 N_1 \otimes N_1 + \lambda_2 N_2 \otimes N_2 + \lambda_3 N_3 \otimes N_3 \tag{6}$$

$$V = \lambda_1 n_1 \otimes n_1 + \lambda_2 n_2 \otimes n_2 + \lambda_3 n_3 \otimes n_3 \tag{7}$$

They measure local stretching or contraction alone their mutually orthogonal eigenvectors, which is a change of local shape. The right stretch tensor U is defined with respect to the reference configuration while the left stretch tensor V acts on the current configuration.

As seen also through the polar decomposition of F, the deformation gradient tensor, although containing all the useful information needed to describe the deformation behavior of a body, is not a suitable deformation measure due to the presence of rotation. For this reason, it is necessary to define other measures, based only on its pure deformation part, as the left and right Cauchy-Green tensors, respectively C and b. These two tensors are defined as:

$$C = F^T F = U^T R^T R U = U^2 \tag{8}$$
$$b = F^T F = V \; R R^T V^T = V^2 \tag{9}$$

C and b are a Lagrangian and an Eulerian strain tensor, respectively. It is possible to introduce the mutually orthogonal and normalized set of eigenvectors N_a and their corresponding eigenvalues λ_a, a = 1, 2, 3, of the material tensor U as:

$$U N_a = \lambda_a N_{a'} |N_a| = 1 \tag{10}$$

Furthermore, by means of the combination of Eq.8, Eq.9, and Eq.10, it is possible to obtain the eigenvalue problem for right Cauchy-Green tensor C as:

$$C N_a = U^2 N_a = \lambda_a^2 N_a \tag{11}$$

It is necessary to solve homogeneous algebraic equations for the unknown eigenvalues λ_a with a = 1, 2, 3, and unknown eigenvectors N_a with a = 1, 2, 3, in the form:

$$(C - \lambda_a^2 I) N_a = 0 \tag{12}$$

To obtain the eigenvalues, the characteristic polynomial of $\mathbf{C}$ must be solved:

$$\lambda_a^3 - I_1\lambda_a^2 + I_2\lambda_a - I_3 \, , a = 1,2,3 \tag{13}$$

with the three principal invariants Ia of the right Cauchy-Green deformation tensor $\mathbf{C}$:

$$I_1(\mathbf{C}) = tr(\mathbf{C}) \tag{14}$$

$$I_2(\mathbf{C}) = \frac{1}{2}[tr(\mathbf{C})^2 + tr(\mathbf{C}^2)] \tag{15}$$

$$I_3(\mathbf{C}) = det(\mathbf{C}) \tag{16}$$

In these equations, the right Cauchy-Green deformation tensor $\mathbf{C}$ can be replaced by the left Cauchy-Green deformation tensor $\mathbf{b}$. The eigenvalues of the symmetric tensor $\mathbf{U}$ are λ_a, called the principal stretches, while for the symmetric tensor $\mathbf{C}$, which is found to be the squares of the principal stretches denoted by λ_a.

Stretch ratios are defined as the square root of the eigenvalues of $\mathbf{C}$ (equal to those of $\mathbf{b}$) and are classically denoted as λ_a, a = 1, 2, 3. By using this ratio, principal invariants can be expressed as:

$$I_1\ (\mathbf{C}) = tr(\mathbf{C}) = \lambda_1^2 + \lambda_2^2 + \lambda_3^2 \tag{17}$$

$$I_2\ (\mathbf{C}) = \frac{1}{2}[tr(\mathbf{C})^2 + tr(\mathbf{C}^2)] = \lambda_1^2\lambda_2^2 + \lambda_1^2\lambda_3^3 + \lambda_2^2\lambda_3^2 \tag{18}$$

$$I_3\ (\mathbf{C}) = \det(\mathbf{C}) = \lambda_1^2\lambda_2^2\lambda_3^2 \tag{19}$$

There are other adoptable deformation measures, such as the Green-Lagrange strain tensor or the Euler-Almansi strain tensor, respectively defined as:

$$\mathbf{E} = \frac{1}{2}(\mathbf{C} - \mathbf{I}) \tag{20}$$

$$\mathbf{e} = \frac{1}{2}(\mathbf{I} - \mathbf{b}^{-1}) \tag{21}$$

One of the major advantages arising from the use of this particular strain measure derives directly from the logarithm properties and is based on the additive decomposition of the applied deformation history. In fact, by considering a deformation of a fiber, say λ, as the result of the combination of two stretches (in this case $\lambda_1 = l/l_1$ and $\lambda_0 = l_1/l_0$, where l_1 can be considered as an intermediate length of the fiber in its change of length from l_0 to l), it is possible to write that $\lambda_1 = \lambda_0\lambda_1$ while the correspondent Hencky (true strain) is defined as:

$$\varepsilon = \ln\left(\frac{l}{l_0}\right) = \ln\left(\frac{l}{l_1}\frac{l_1}{l_0}\right) = \ln\lambda_1 + \ln\lambda_0 \tag{22}$$

2.1.2 Stress Measures

Motion and deformation give rise to interactions between the material and neighboring material in the interior part of the body. One of the consequences of these interactions is stress, which has a physical dimension force per unit of area. The notion of stress, which is responsible for the deformation of materials, is crucial in continuum mechanics.

By focusing the attention on a deformable body $\mathfrak{b}$ which occupies an arbitrary region Ω with a boundary $\partial\Omega$ at a time t, it is at first necessary to define external forces as forces acting on parts of the boundary, and as internal forces the ones within the interior part of the domain, in a distributed way (such as gravity). Now, let the body be cut by a plane passing through a given point $x \in \Omega$; this plane, which can be indicated as π, cuts the body into two parts. By considering the interaction of the two portions, it is possible to realize that forces are transmitted across the plane surface, see Figure 16.
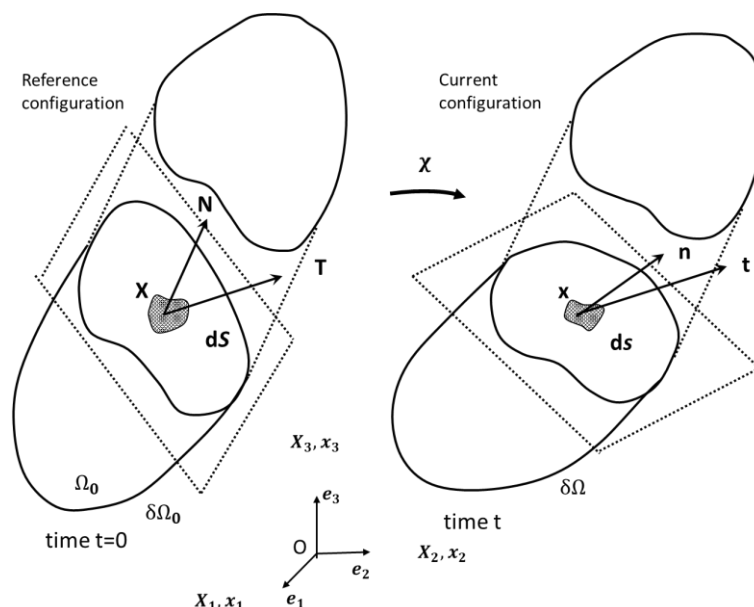
Figure 16 – Traction vectors acting on infinitesimal surface elements with outward unit normal.

The infinitesimal resultant force acting on a surface element of the area dS will then be df so that, in the point X the Cauchy surface traction can be defined as:

$$t(x,t) = \lim_{\Delta S \to 0} \frac{\Delta f}{\Delta S} = \frac{df}{dS} \tag{23}$$

The traction vector in Eq.23 persists on all surfaces passing through the point P that have the same normal vector **n**. It is possible at this point to recall the Cauchy stress theorem, which asserts that there exists a second-order tensor $\sigma(x,t)$ so that the traction vector **t** is a linear function of **n**, so that:

$$t(x,t,n) = \sigma(x,t)n \tag{24}$$

Through equilibrium of the angular momentum, it also is possible to show that the second-order tensor $\sigma(x,t)$, generally called Cauchy stress tensor, is symmetric. It is defined through the Eulerian description, and can be represented as:

$$\sigma(x,t) = \sigma_{ij} n_i \otimes n_j \tag{25}$$

where $\otimes$ stands for the tensor product defined by $(\mathbf{p} \otimes \mathbf{q})\,\mathbf{r} = \mathbf{p}\,(\mathbf{q} . \mathbf{r})$.

Multiplying the Cauchy stress tensor by the Jacobian J it is possible to obtain the Kirchhoff stress tensor, τ:

$$\tau = J\sigma \tag{26}$$

Instead, by following the same treatise as for the Cauchy stress tensor through an Eulerian description, it is possible to obtain the first Piola-Kirchhoff stress tensor by doing so through a Lagrangian description:

$$P = P_{ij} n_i \otimes N_j \tag{27}$$

It is important to notice also that the first Piola-Kirchhoff stress tensor is not symmetric. The second Piola-Kirchhoff stress tensor, instead, is symmetric and defined as:

$$S = F^{-1}P \tag{28}$$

A fundamental relationship between the first Piola-Kirchhoff stress tensor **P** and the second Piola-Kirchhoff stress tensor **S** is found as follows:

$$P = FS \tag{29}$$

To obtain the stress tensors, we need a material law describing the relation of stress and strain. The deformation gradient $\boldsymbol{F}$ is a stretch tensor. The invariant I_1 and I_2 are used as quantities for isotropic deformation whereas I_3 is used for volumetric change descriptions. Furthermore, so-called pseudo-invariants can be used to describe anisotropic behavior caused by fibers. Within the scope of this thesis, we focus on the fourth, sixth pseudo-invariant as these are used for modeling fibers of aortic tissue. They are given by the direction of fibers f_0 and sheets s_0 in the referential configuration Ω_0 as well as their corresponding stretch parameters λ_f and λ_s via:

$$I_4 = f_0 . \mathbf{C} f_0 = f_0 \boldsymbol{C} : (\boldsymbol{f_0} \otimes \boldsymbol{f_0}) = \boldsymbol{C} : F_0 = \lambda_f^2$$

(30)

$$I_6 = s_0 . \mathbf{C} \, s_0 = s_0 \boldsymbol{C} : (\boldsymbol{s_0} \otimes \boldsymbol{s_0}) = \boldsymbol{C} : s_0 = \lambda_s^2$$

where the notation (.) stands for the inner product between two tensors, and (:) stands for the double inner product. In these equations, F_0 and S_0 are the fiber and second-order tensors defined in Ω_0, respectively.

2.1.3. Use of Strain–Energy Functions

When a body is loaded with force the body will deform in some way. The energy is stored in the volume which we assume to be continuous. The stored energy per unit reference volume is called Helmholtz free-energy and denoted as $\boldsymbol{\Psi}$. The Helmholtz free-energy function can be defined to be a function of $\mathbf{F}$ and its scalar invariants and forms a scalar function:

$$\Psi = \Psi(\boldsymbol{F}) = \psi(I_1, I_2, I_3, I_4, I_5, I_6)$$

(31)

If we neglect the change of area for the body, we call this the nominal stress or first Piola-Kirchhoff stress tensor $\mathbf{P}$. The first Piola-Kirchhoff stress tensor is a quantity with its force defined in the actual configuration and its area defined in the referential configuration Ω_0. Thus, the first Piola-Kirchhoff stress tensor is unsymmetrical and defined via:

$$\boldsymbol{P} = \frac{\delta \Psi}{\delta \boldsymbol{F}} = \sum_i \frac{\delta \Psi}{\delta I_i} \frac{\delta I_i}{\delta \boldsymbol{F}}$$

(32)

Finally, the true stress tensor also called Cauchy stress tensor $\boldsymbol{\sigma}$ describes the actual stress referred to the actual surface. The Cauchy stress is obtained through:

$$\boldsymbol{\sigma} = J^{-1} \boldsymbol{P} \boldsymbol{F}$$

(33)

The strain-energy function $\mathbf{\Psi}$ can be composed of various energy functions as long as the laws of thermodynamics are fulfilled. The second law of thermodynamics states that energy can never be created and dissipation is either zero or positive. Neglecting thermal effects the internal dissipation is given by:

$$D_{int} = \mathbf{P} : \dot{\mathbf{F}} - \dot{\psi} \geq 0 \tag{34}$$

If the internal dissipation is zero, the process is completely reversible without entropic effects. Hence, a lossless Clausius-Planck equation occurs:

$$\dot{\psi} = \mathbf{P} : \dot{\mathbf{F}} \tag{35}$$

2.2 Constitutive model for arteries

A constitutive model is a mathematical characterization of materials intrinsic relationship between force and deformation (or stress and strain), and along with appropriate governing equations, capable of describing the mechanical behavior of the material under specific conditions. Appropriate constitutive relations are needed for computational modeling of stress-strain states in arteries.

A hyperelastic material is a special case of elastic materials, with the property that the work is independent of the load path. That is, the work done depends only on the initial and final states. Hyperelasticity theory states that for any solid there exists a strain energy function W which depends only on the deformation. So, hyperelastic constitutive relations represent a mathematical description of stress and strain components that are derived from strain energy density function W. For a hyperelastic material, the second Piola-Kirchhoff stress is derived from the strain energy as (Belytschko, Liu and Moran, 2000 [50]):

$$\mathbf{S} = 2 \frac{\delta W(\mathbf{C})}{\delta \mathbf{C}} = \sum_i \frac{\delta \Psi(\mathbf{E})}{\delta \mathbf{E}} \tag{36}$$

where W and Ψ are the strain energy functions; $\mathbf{C}$ and $\mathbf{E}$ are the right Cauchy-Green deformation tensor and the Green strain, respectively. The relationship between these two tensors is given in Eq.20. Thus, the relation between the two scalar functions is given as W($\mathbf{C}$)=Ψ(2$\mathbf{E}$+$\mathbf{I}$). According to Eq.33, the Cauchy stress for hyperelastic material can be written as:

$$\boldsymbol{\sigma} = 2J^{-1}\boldsymbol{F}\frac{\delta W(\boldsymbol{C})}{\delta \boldsymbol{C}}\boldsymbol{F}^T \tag{37}$$

Hyperelastic models can be classified into two types of formulation, depending on the approach used to develop the strain energy function. The first formulation arises from the mathematical developments of the strain energy function W. They are classically referred to as phenomenological models. Material parameters a generally difficult to determine and such models can lead to an error when they are used out of the deformation range in which their parameters were identified. These include:

1. The Mooney-Rivlin Model

$$W = C_1(I_1 - 3) + C_2(I_2 - 3) \tag{38}$$

2. The Yeoh Model

$$W = C_1(I_1 - 3) + C_2(I_1 - 3)^2 + C_3(I_1 - 3)^2 \tag{39}$$

3. The Biderman Model

$$W = C_{10}(I_1 - 3) + C_{01}(I_1 - 3) \quad + C_{01}(I_1 - 3)^2 + C_{30}(I_1 - 3)^2 \tag{40}$$

4. The Ogden Model

$$W = \sum_{n=1}^{N}\frac{\mu_n}{\alpha_n}(\lambda_1^{\alpha_n} + \lambda_2^{\alpha_n} + \lambda_3^{\alpha_n} + 3) \tag{41}$$

The phenomenological based models are summarized in Table 2:

Table 2 - List of the phenomenological-based models by the year of publication.

Model	Year	Number of material parameters	Equation
Mooney-Rivlin	1940	2	Eq. 38
Yeoh	1990	3	Eq. 39
Biderman	1958	4	Eq. 40
Ogden	1972	6	Eq. 41

The second models are referred to as "Physical models". The main models being discussed in this section will be Neo-Hookean, Fung's, Guccione's, and Holzapfel-Gasser-Ogden's strain energy models. The strain energy equations can be modified for 2-D as well as 3-D analysis. The following models will be presented in their 3-D form except for the Fung model.

The Neo-Hookean model. The Neo-Hookean model is the simplest strain energy model; it describes the behavior of rubber and takes a form that is closest to the typical stress-strain relationship seen in many metals. Assuming incompressibility:

$$W = c_1(tr\boldsymbol{C} - \boldsymbol{3}) \tag{42}$$

where

$$tr\boldsymbol{C} = 2(E_{11} + E_{22} + E_{33}) + 3 \tag{43}$$

and E_{11}, E_{22}, and E_{33} are the Green strains in the fiber and two cross-fiber directions. The Neo-Hookean model only has one material constant and displays a linear relationship between the Cauchy stress and right Cauchy-Green deformation, hence the name that is in reference to Hooke's Law. The Neo-Hookean has been shown to describe the isothermal behavior of rubber for up to 30% deformation whereas Hooke's Law only applies for linear elastic behavior of engineering metals, generally up to 0.2% strain. However, the Neo-Hookean model only describes the behavior for isotropic materials, and therefore cannot be used to describe most soft tissue materials.

Fung Model. The Fung strain energy model was initially developed to describe the behavior of skin tissue; however, it has also been determined that variations of this model can reliably describe other soft tissue behavior such as heart valvular tissue [47]. The following is the generalized pseudo-elastic 2D Fung strain energy model. The strain energy function takes on an exponential form:

$$W = \frac{c_1}{2}[\exp(Q_F) - 1] \tag{44}$$

where Q_F is a quadratic function of the two principal strains of the material and shear strain:

$$Q_F = c_2 E_{11}^2 + c_3 E_{22}^2 + 2c_4 E_{22}E_{11} + c_5 E_{12}^2 + 2c_6 E_{11}E_{12} + 2c_7 E_{22}E_{12} \tag{45}$$

E_{11} is the Green strain along the fiber direction of the soft tissue while E_{22} is the Green strain in the cross-fiber direction. Shear strains E_{12} and E_{21} are equal because the Green strain tensor is symmetric by definition. The Fung model assumes soft tissue to be orthotropic and contains seven material constants; c_1 is a scaling factor usually in terms of membrane tension (N/m) or stress (N/m^2) while the other six constants are dimensionless. These parameters have no direct physical meaning.

<u>The Holzapfel, Gasser, and Ogden model.</u> The Holzapfel, Gasser, and Ogden (HGO) strain energy function was developed to model arterial behavior [17]. While the Fung model is considered phenomenological, i.e. not derived directly from first principles and the material's microstructure, the HGO model was developed from theory regarding the mechanics of fiber-reinforced composites. The HGO strain energy function assumes the material to be orthotropic and was determined by modeling an artery as a thick-walled cylinder, with two families of collagen arranged in helices along its length [17]. The model is made from different layers with separated strain-energy functions [17]. Each layer is considered a composite with the collagen fibers acting as reinforcement. As each layer displays similar mechanical behavior the same strain energy function was used but with different material constants [17]. The HGO model is split into two parts: the strain energy stored from isotropic deformations ψ_{iso} (the mechanical response from the non-collagenous matrix), and the strain energy from anisotropic deformations ψ_{aniso} from the collagen fibres [17]. The 3-D HGO strain energy equation for a layer of material is shown:

$$\psi(\boldsymbol{C}, \boldsymbol{A_1}, \boldsymbol{A_2}) = \psi_{iso}(I_1, I_2) + \psi_{aniso}(I_1, I_2, \dots, I_8) \tag{46}$$

where the families of collagenous fibers are characterized by the two (reference) direction vectors $a_{0,i}$, i= 1,2, with $|a_{0,i}|$= 1. Note that the invariants I_4 and I_6 are the squares of the stretches in the directions of a_{01} and a_{02}, respectively, so that they are stretch measures for the two families of (collagen) fibers and therefore have a clear physical interpretation. The anisotropy then arises only through the invariants I_4 and I_6, but this is sufficiently general to capture the typical features of arterial response. Finally, the two contributions ψ_{iso} and ψ_{aniso} to the function, ψ must be particularized to fit the material parameters to the experimentally observed response of the arterial layers. They used the (classical) neo-Hookean model to determine the isotropic response in each layer:

$$\psi_{iso}(I_1) = \frac{c}{2}(I_1 - 3) \tag{47}$$

where c>0 is a stress-like material parameter. The strong stiffening effect of each layer observed at high pressures motivates the use of an exponential function for the description of the strain energy stored in the collagen fibers, and for this, they proposed:

$$\psi_{aniso}(I_1, I_2) = \frac{k_1}{2k_2}\sum_{i=4,6}\{\exp[k_2(I_1 - 1)^2] - 1\} \tag{48}$$

where k_1>0 is a stress-like material parameter and k_2>0 is a dimensionless parameter.

2.3 Multiphoton Microscopy

The mechanical behavior of the arterial wall is mainly governed by the organization and composition of the three major micro-structural components: collagen, elastin, smooth muscle cells. Their influence on cardiovascular function in health and disease has been the subject of extensive research.

Research indicates that changes in the mechanical properties of healthy arterial walls play a role in arterial disease and degeneration (e.g., increased stiffening of vessel walls with age, atherosclerosis, etc.). Meaningful quantifications of these components in human arteries, therefore, are fundamental to a better understanding of the underlying mechanical principles governing the biomechanical response of vessel walls. Previous studies have quantitatively shown increased collagen fiber straightness as a result of mechanical loading [51-53]. The changes in both collagen and elastin orientation have also been evaluated [44, 54, 55]. Recent advances in multiphoton technology have allowed the investigation of the structure of the tissue.

Multiphoton microscopy is suitable for high-resolution and long-term imaging of living cells. The beneficial characteristics are its intrinsic three-dimensional resolution, high penetration depth, negligible out-of-focus photobleaching, and reduced photodamage [56].

Multiphoton microscopy simultaneously uses two non-linear optical effects, two-photon excitation and second harmonic generation, for imaging of biological tissues. Both types of nonlinear interactions occur in biological tissues without the addition of exogenous contrast agents. Two-photon excited fluorescence has been widely used for imaging cells and tissues [57-62]. The second-harmonic generation has recently been employed for biological imaging applications [63, 64]. The combination of TPF and SHG has been implemented for the study of cells [65, 66], thin tissue sections [65], and for the more practical case of thick, unstained living specimens [64, 67].

Collagen is a well-documented source of tissue SHG [65]. Elastin is also a significant source of extracellular matrix autofluorescence [68]. Collagen and elastin are important determinants of the mechanical properties of blood vessels. Their selective visualization is of fundamental interest for the determination of the microstructural origins of mechanical properties.

In this project, TPF and SHG were used to accomplish the selective visualization of the structural components of the arterial wall. Specifically, it was used TPF and SHG microscopy to selectively monitor the structural changes of collagen and elastin. This approach will establish a microstructural foundation for the observed mechanical properties of blood vessels and shows the potential of MPM

as a non-invasive technique for the characterization of vascular physiology and pathology. However, the interactions of collagen and elastin on vascular function are not well understood.

2.3.1 Two-Photon Laser Scanning Microscopy

Two-photon laser scanning microscopy (TPLSM) has become a powerful method to image living cells with high submicron resolution [57]. Two-photon absorption was first predicted by Maria Goppert-Mayer in 1931 [69]. She showed that photons of lower energy together can produce excitation similarly obtained by the absorption of a single photon of higher energy. This process is called two-photon excitation. Two-photon microscopy put into practice the simplest version of the theoretical prediction: two photons, each having the same amount of energy (from the same laser), interact with a molecule and the excitation corresponds to the absorption of a single photon possessing twice the energy, this process is illustrated in Figure 17.
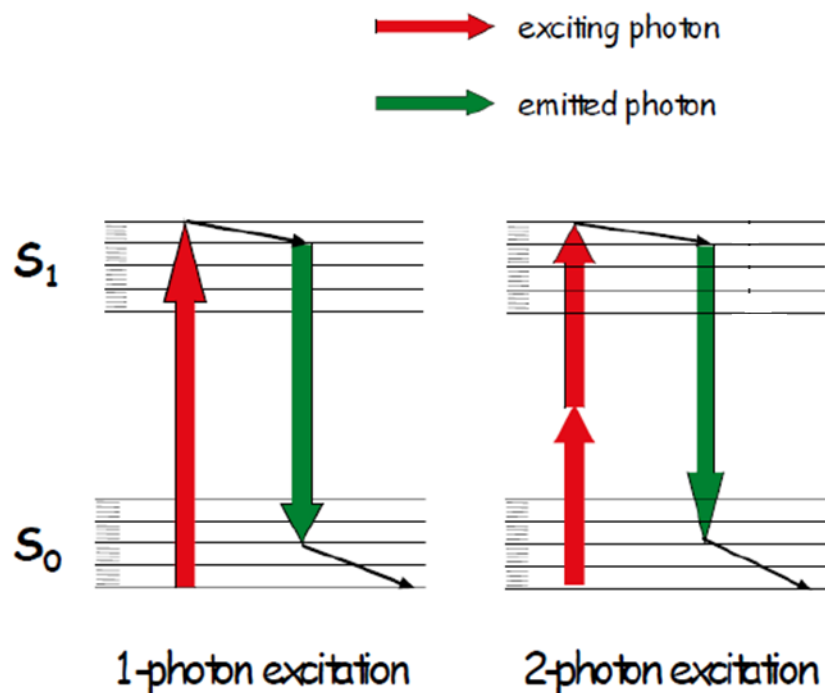
Figure 17 – Energy transition for one-photon and two-photon excitation. (www.leica-microsystems.com).

A fluorescent excited molecule emits a single photon of fluorescence as if it were excited by a single higher energy photon. This event occurs because both the two photons interact with the excited molecule nearly simultaneously (about 10-16s). The result is a quadratic dependence on the light intensity rather than the typical linear dependence of conventional fluorescence. Two-photon processes are called non-linear for this reason: the rate at which they occur depends non-linearly on

the intensity of the radiation. The intensity squared dependence is the basis of the localized nature of two-photon excitation: doubling the intensity produces four times the fluorescence [70].

Two-photon microscopy has been used to image the elastin in vascular tissue [56-59, 61, 62, 67]. Elastin fibers contain a fluorophore, believed to be the pyridinoline molecule that causes it to be intrinsically fluorescent. Traditional single-photon absorption uses an excitation wavelength of 340nm [71] and an emission maximum near 400nm [70]. Therefore, for two-photon excitation laser light of 700-740nm is required. Imaging of elastin in arteries by TPLSM has been accomplished by several researchers [56-59, 61, 62, 67]. The elastin in the aorta was examined using TPLSM by Parasassi et al. [72]. More recently, Megens et al. [73] demonstrated the use of TPLSM for examining elastic and muscular arteries of mice. They showed that the fenestrae are visible in the internal elastic laminae as non-fluorescent cylindrical patches. The mean diameter of fenestrae was found to be larger in the muscular arteries, 2.1±0.2 μm than in elastic ones, 1.3±0.4 μm. Similarly, there was a significantly higher density of fenestrae in the muscular artery than in the elastic artery. These results indicate that it is possible to use TPF to provide reliable images of elastin structure for the examination of the fenestrae, not only in healthy tissue but in diseased vessels as well.

2.3.2 Second Harmonic Generation Microscopy

Second-harmonic generation (SHG) is the process of two photons being annihilated to obtain one photon with twice the energy [74]. The distinction of SHG from two-photon fluorescence is mainly due to the fact that the signal is not produced by the absorption of the photons by a fluorophore, but due to light interaction as a result of the medium through which it is traveling. For SHG to occur the medium must lack inversion symmetry. This requires the molecules themselves and the molecules in bulk form to be non-centrosymmetric [63, 64]. Imaging of collagen by SHG provides a maximum signal when an excitation wavelength of 700—740nm is applied, although higher wavelengths, above 900nm, increase the penetration depth into the sample. Because of the agreement of the wavelength of the applied laser light, SHG and TPLSM are used simultaneously for the imaging of aortic tissue, Figure 18.
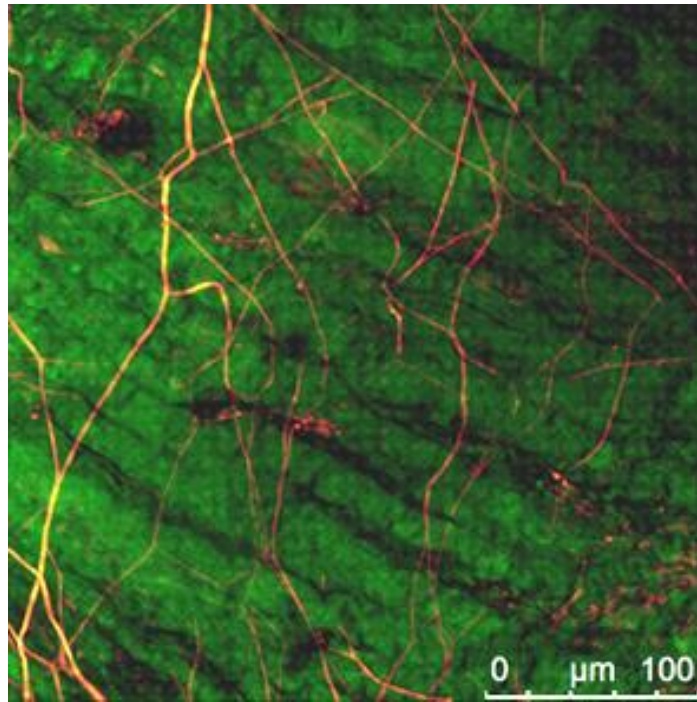
Figure 18 – Multiphoton images of human aorta. Tissue fluorescence of elastin in orange, SHG of collagen in green.

Williams et al. [75] have been able to use SHG to investigate type I collagen from rat tail tendon. They found that the resulting signal comes from the fiber shell, not the bulk of the material. Zoumi et al. [67] combined TPLSM with SHG to examine the effects of distension on rabbit aorta and porcine coronary arteries. They found that there were significant changes in wall thickness and dimension between zero load, zero stress, and distended vessels. Their results prove that multimodal microscopy can be applied to vascular biomechanics as well.

2.4 Material hereditariness

The mechanical behavior of the materials discussed in previous chapters has been shown dependent on the specific kind of tissue considered. Such observation led to two limit cases: i) in presence of a complete recovery in cyclic tensile tests the concept of material elasticity is introduced; ii) in presence of mechanical behavior such that complete energy dissipation (no recovery) is observed, the concept of viscous material is reported. Materials show an intermediate behavior and therefore the term material hereditariness is introduced. The term hereditariness indicates the intermediate behavior of a material between elastic and viscous, this behavior is typical of polymers [76], of human tissues and bones, of various mortars and resins used in construction, of some families of rocks [77] and other materials. The hereditariness material therefore it is characterized by having two asymptotic behaviors, the solid elastic one and the viscous liquid one. From previous

considerations, it is clear that time dependence of biological materials is a crucial aspect for understanding their function and performance. Hereditariness has been studied in numerous biological materials such as cardiovascular tissues, bones, articular cartilages, skeletal muscles, ligaments, and tendons [78, 79]. Aortic tissues are hereditariness and thus, display time-dependent hand load-history-dependent mechanical behavior.

To describe the history of stress and strain two functions are used: $\Phi_r(\varepsilon, t)$ and $\Phi_c(\sigma, t)$. In general, these functions are assumed to be non-linear. To investigate the nature of $\Phi_r(\varepsilon, t)$ and $\Phi_c(\sigma, t)$, experimental creep and relaxation testing are required.
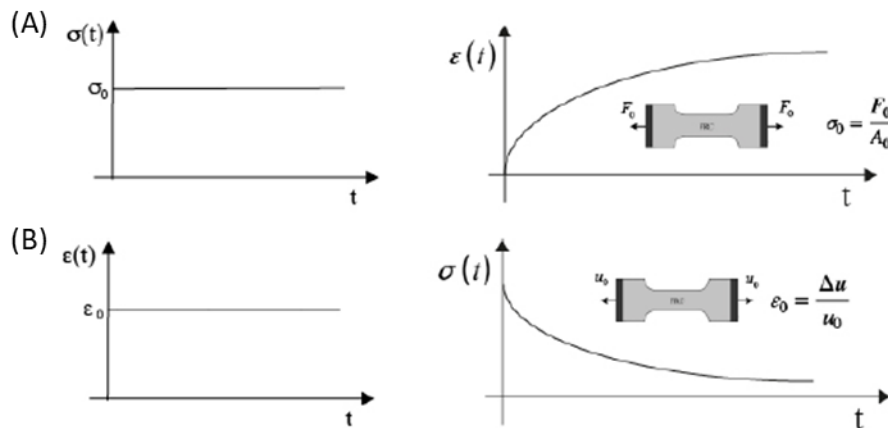
Figure 19 – (A) Creep and (B) stress relaxation test.

Let a specimen be subjected to a step stress history (Figure 19A) in which the stress is instantaneously increased to some value σ_0 at t=0 and then held. The typical strain response consists of an instantaneous increase of the strain at t=0, followed by continued straining in time at a non-constant rate, and an asymptotic approach to some limit value at time increases. The behavior is called creep. Let $\Phi_c(\sigma_0, t)=J(t, \sigma_0)$ denote the strain at time t when the value of the stress is σ_0. Please do not confuse $J(t, \sigma_0)$, called the creep compliance, with the Jacobian.

$J(t, \sigma_0)=0$ when t <0, then jumps to value $J(0,\sigma_0)$ at t=0 and monotonically increases to the limit value denoted by $J(\infty,\sigma_0)$ as t $\rightarrow \infty$. The jump in strain $J(0, \sigma_0)$ at t=0 indicates instantaneous springiness or elasticity. The fact that the material reaches a non-zero limit value of strain indicates solid behavior. If the strain were to increase without bound, it would indicate fluid behavior, which is not considered here. The relations σ_0 vs $J(0,\sigma_0)$ and σ_0 vs $J(\infty, \sigma_0)$ describe, respectively, instantaneous elastic response and the long-time or equilibrium elastic response. $J(t,\sigma_0)$ has a different dependence on time t and stress for each material and is therefore considered to be a material property called the creep function.

Let a specimen be subjected to a step strain history (Figure 19B), in which the strain is instantaneously increased to some value ε_0 at t=0 and then held. The typical stress history required

to produce this strain history consists of i) an instantaneous increase in stress at t=0 followed by ii) a gradual monotonic decrease of stress at a non-constant rate and iii) an asymptotic approach to some non-zero limit value as time increases. The behavior is called stress relaxation. Let $\Phi_r(\varepsilon_0, t)=G(t, \varepsilon_0)$ denote the stress at time t when the value of the strain is fixed at ε_0. Then, $G(t, \varepsilon_0)=0$ when t<0, $G(t, \varepsilon_0)$ jumps to the value $G(0, \varepsilon_0)$ at t=0, and $G(t, \varepsilon_0)$ monotonically decreases to the non-zero limit value denoted by $G(\infty,\varepsilon_0)$ as t$\rightarrow \infty$. The jump in stress $G(t,\varepsilon_0)$ at t=0 is another indication of instantaneous springiness or elasticity. The fact that a non-zero stress $G(\infty,\varepsilon_0)$ is required to maintain the strain at ε_0 is another indication that the material is a solid. If $G(\infty, \varepsilon_0)=0$, then no stress would be required to hold the material in a deformed state, a characteristic response of fluids. The relations $G(0, \varepsilon_0)$ vs ε_0 and $G(\infty, \varepsilon_0)$ vs ε_0 also describe, respectively, instantaneous elastic response and the long-time or equilibrium elastic response. $G(t, \varepsilon_0)$ has a different dependence on time and strain for each material and is therefore considered a material property called the stress relaxation function.

Let H(t) denote the Heaviside step function, H(t)=0, t $\in (\infty,0)$ and H(t)=1, t $\in [0,\infty)$. When there is linearity, the stress response to the step strain history $\varepsilon(t)=\varepsilon_0 H(t)$ is:

$$\sigma(t)=G(t, \varepsilon 0)=\varepsilon 0 G(t) \tag{49}$$

G(t) is called the stress relaxation modulus. It is convenient to introduce the notation $G(0) = G_0$ and G∞ and for the limit of G(t) as t$\rightarrow \infty$.

Similarly, the strain response to the step stress history $\sigma(t)=\sigma_0 H(T)$ is

$$\varepsilon(t)=J(t, \sigma 0)=\sigma 0\, J(t) \tag{50}$$

J(t) is called creep compliance. It is assumed that $J(0) > 0$ and J(t) monotonically increases to a finite limit J∞>0 as t$\rightarrow \infty$. It is convenient to introduce the notation $J(0)=J_0$ and J_∞ for the limit J(t) as t $\rightarrow \infty$.

2.4.1 Rheological Models

One of the approaches used to develop constitutive equations for linear hereditary response involves mechanical analogs. These are mechanical devices formed by combining linear elastic springs and linear viscous dampers in series or parallel. The devices can be shown to exhibit a time-dependent response that is similar to that observed in hereditary materials, namely, creep under constant load and force relaxation under constant deformation. For this reason, these devices are treated as mechanical analogs of hereditariness response. Since the springs and dampers are described by linear equations, as the equations for the kinematics of deformation and force transmission, there must be a linear relationship between the overall force and deformation. These approaches are known as rheological models and they will be discussed in the following. The spring in Figure 20A

is the elastic (or storage) element, as for it the force is proportional to the extension; it represents a perfectly elastic body obeying the Hooke law (Hooke model). In this case, we have no creep and no relaxation, therefore the creep compliance and the relaxation modulus are constant functions $J(t) \equiv 1/E$, $G(t) \equiv E$.

The dashpot in Figure 20B is the viscous (or dissipative) element, with the force being proportional to the rate of extension. It represents a perfectly viscous body obeying the Newton law (Newton model). We note that the Hooke and Newton models represent the limited cases of viscoelastic bodies. A device constituted by a spring in parallel with a dashpot is known as the Voigt model, see Figure 20C where $\tau\varepsilon$ is referred to as the retardation time. A device constituted by a spring in series with a dashpot is known as the Maxwell model, see Figure 20D, where τ_σ is referred to as the relaxation time. The Voigt model exhibits an exponential (reversible) strain creep but no stress relaxation; it is also referred to as the retardation element.
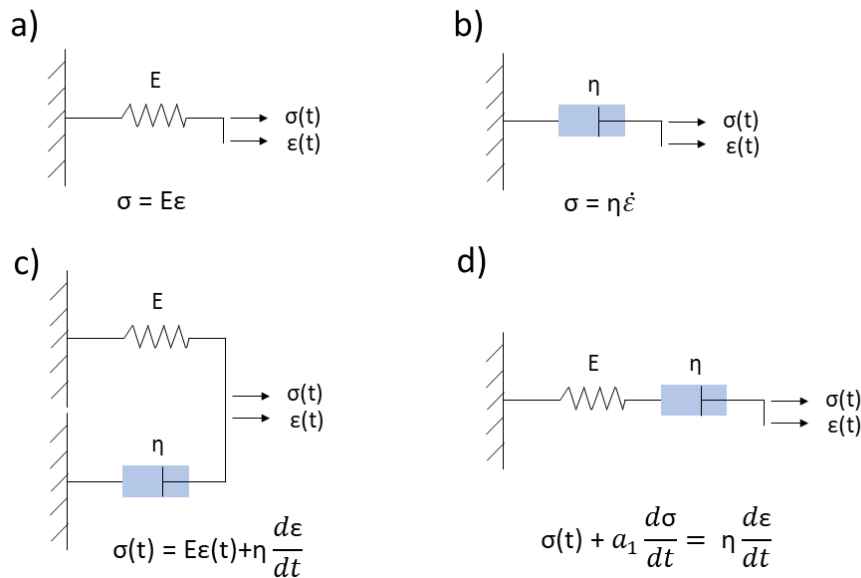
Figure 20 – Classic viscoelastic models: a) Hooke model, b) Newton model, c) Kelvin-Voigt model, d)Maxwell model.

The Maxwell model exhibits an exponential (reversible) stress relaxation and a linear (non-reversible) strain creep; it is also referred to as the relaxation element. By increasing the number of simple elements to the Kelvin-Voigt model, other more accurate models in the simulation of viscoelastic behavior are obtained. Such models are called SLS (Standard Linear Solid) or Zener.

Fractional-order linear hereditariness

Linear hereditariness is certainly the field of the most extensive applications of fractional calculus, given its ability to model hereditary phenomena with a long memory. The analysis starts from the power-law creep to justify the introduction of the operators of fractional calculus into the stress-strain relationship.
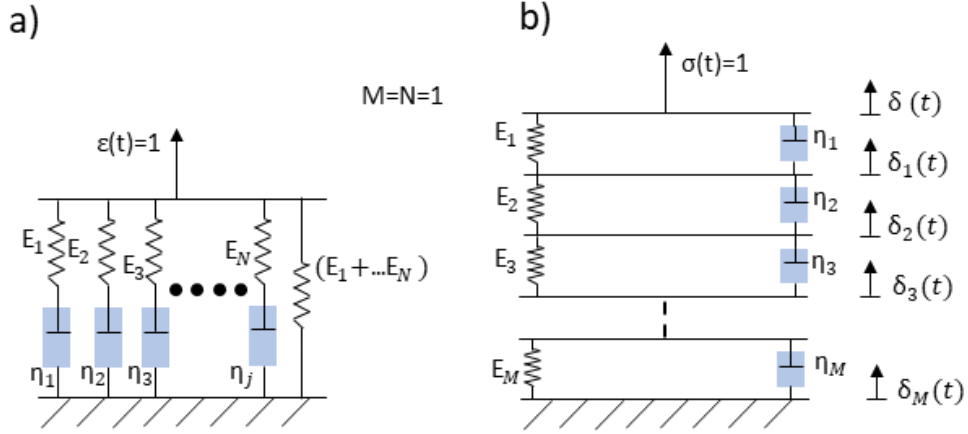
Figure 21 – a) Rheological model for exponential relaxation; b) Rheological model for exponential creep.

Let us consider the hereditariness of material with creep compliance:

$$J(t) = \frac{1}{G_0 \Gamma(1+\beta)} \left(\frac{t}{\tau_0}\right)^{\beta} \tag{51}$$

where Γ is the Euler-Gamma function, G_0 is the elastic modulus of the material, β and $[\tau_0]=T$ are material parameters that may be estimated through a best-fitting procedure of experimental data. Such creep behavior is found to be of great interest in several creep experiments; usually, it is referred to as the power-law creep.

Given the reciprocity relationship in the Laplace domain:

$$\hat{J}(s)\hat{G}(s) = \frac{1}{s^2} \tag{52}$$

we can find for such hereditariness solid its relaxation modulus, and then the corresponding relaxation spectrum. After simple manipulations we get:

$$G(t) = \frac{G_0}{\Gamma(1-\beta)} \left(\frac{t}{\tau_0}\right)^{-\beta} \tag{53}$$

For our hereditariness solid exhibiting power-law creep, the stress/strain relationship in the creep representation can be easily obtained by inserting the creep law (Eq.52) into the integral (Eq.52). Straightforward manipulations deliver the following constitutive relations:

$$\sigma(t) = \frac{G_0 \tau_0^{\beta}}{\Gamma(1-\beta)} \int_0^t (t-\tau)^{-\beta} \dot{\varepsilon}(\tau)d\tau = G_0 \tau_0^{\beta} (D_{0+}^{\beta}\varepsilon)(t) \tag{54}$$

$$\varepsilon(t) = \frac{1}{G_0 \tau_0^{\beta}\Gamma(1+\beta)} \int_0^t (t-\tau)^{\beta} \dot{\sigma}(\tau)d\tau = \frac{1}{\tau_0^{\beta} G_0} (I_{0+}^{\beta}\sigma)(t) \tag{55}$$

Where $[CD_0^{+\beta}]$ is the Fractional Caputo derivative and $[I_0^+\beta]$ is the Riemann-Liouville fractional integral. The constitutive equations Eq.54 and Eq.55 have been modeled with the introduction of a

new rheological element, the springpot, after Scott-Blair. The springpot is a mechanical element with mechanical properties that are intermediate between those of a pure elastic solid (Hooke model) and a purely viscous fluid (Newton model). The use of fractional calculus in linear hereditariness leads us to generalize the classical mechanical models, in that the basic Newton element (dashpot) is substituted by springpot. The springpot, presented in Figure 22, is defined in terms of two parameters, i.e. $C^\beta = G_0 \tau_0^\beta \geq 0$ and β with $\beta \in [0,1]$. Such element is widely used nowadays to define several types of materials including as limiting cases, elastic ($\beta = 0$) and viscous elements ($\beta = 1$).
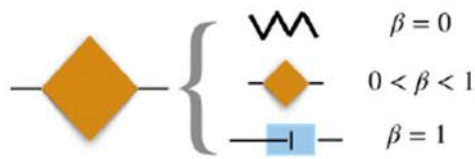
Figure 22 – Springpot element.

Chapter III

Identification of circumferential regional heterogeneity of ascending thoracic aneurysmal aorta by biaxial mechanical testing

The content of this chapter was published as a research article in Journal of Molecular and Cellular Cardiology by Di Giuseppe M., Alotta G., Agnese V., Bellavia D., Raffa G.M., Vetri V., Zingales M., Pasta S., Pilato M.

3.1 Background

Ascending thoracic aortic aneurysm (ATAA) is a life-threatening cardiovascular disease leading to weakening of the aortic wall and permanent dilation associated with high risk of adverse events [1]. ATAA affects approximately 10 out of 100,000 persons per year [80], with bicuspid aortic valve (BAV) patients having associated aortopathy on approximately 40% of the bicuspid population [20]. The risk of complications such as aortic dissection and rupture is higher in BAV patients than that of patients with the morphological-normal tricuspid aortic valve (TAV) [81]. To avoid aortic complications, the current clinical management of ATAA is based on strict monitoring of aneurysms size as well as elective repair when aortic diameter enlarges upon a critical size [82]. Aortic size is not a good predictor of ATAA failure, and this is known as the "size paradox" [83].

Aortic stiffness is associated with progressive aortic dilatation and aneurysm formation as shown by different imaging modalities [6, 7], computational analyses [4, 8, 84], and histological changes [9]. Higher aortic stiffness was associated with higher rates of surgical aortic replacement and aortic root dilation in children and young adults with connective tissue disorders [85]. In Marfan patients, aortic stiffness proved to have an important value in predicting progressive aortic dilatation [86]. A recent study of abdominal aortic aneurysms found that segmental stiffening of the aorta preceded aneurysm growth and introduced the concept that stiffening may act as an early mechanism triggering elastin breakdown and aneurysm growth [87]. However, aortic stiffness is not homogenous along the circumferential direction of the ascending aneurysmal aorta, thereby exposing local regions of the vessel at greater risk of complications than others. Alternative risk strategies, as opposed to the maximum aortic diameter criterion, are being developed by evaluating changes in the aortic stiffness of the ATAA wall [3-5]. These approaches rely on the utilize of computational tools to non-invasively

estimate wall stress/strain using homogenous material properties along the circumferential direction of the diseased aorta.

This study was undertaken to quantify the degree of regional heterogeneity of the ascending aneurysmal aorta as well as to determine differences of mechanical properties for their implementation on computational wall stress predictions. Specifically, equibiaxial mechanical testing was performed on tissue specimens extrapolated from aortic quadrants (i.e. anterior, posterior, major, and minor curvature) of ATAA rings obtained from surgically repaired patients with either BAV or TAV. The Fung-type constitutive equation was achieved for each aortic quadrant, and then the specimen tissue stiffness was derived at both physiological and supraphysiological stress levels to compare differences among groups.

3.2 Materials and Methods

3.2.1 Study population and specimen preparation

Aortic tissue samples were obtained from patients who underwent repair of the aneurysmal ascending aorta at IRCCS ISMETT as part of their clinical care and not for the purpose of the study. All patients signed informed consent before surgery, and the study was approved by the local ethical committee (IRRB/04/14). Indication for aortic surgery was based on aortic size measurement, predisposing risk factors, bicuspid aortopathy, and familiarities. A total of 36 aortic segments (n.10 BAV ATAA and n.26 TAV ATAA) were analyzed by biaxial testing and grouped according to the aortic valve morphology (i.e. BAV vs TAV) as seen by computed-tomography (CT) imaging parallel to the aortic valve plane.

After surgery, ATAA samples were cryopreserved in a calcium-free and glucose-free 0.9% physiological saline solution and stored at −80 °C before material testing and multiphoton imaging. Along the circumferential direction of ascending aorta, the harvested tissue ring was cut into squared specimens from each quadrant as a following: (a) anterior, (b) posterior, (c) major curvature, and (d) minor curvature of the aorta, as shown in Figure 23. The thickness and dimensions of each squared sample were measured using a caliber before material testing. Table 3 summarizes clinical demographics data and thickness measurements for each specimen.

Table 3 - Demographic data and measurements of thickness along the circumferential direction of the ATAA.

ID	Sex/Age/Valve	Diameter (mm)	Thickness Posterior (mm)	Thickness Major (mm)	Thickness Minor (mm)	Thickness Anterior (mm)
1	M/72/BAV	54	2.1	2.1	2.1	2.1
2	F/74/TAV	53	2.1	2.1	2.1	2.1
3	M/57/BAV	43	2.2	2.2	2.2	2.2
4	F/65/TAV	56	1.8	1.8	1.8	1.8
5	M/73/TAV	49	3.6	4.0	3.6	5.6
6	M/65/BAV	40	2.2	2.2	2.2	2.1
7	M/70/TAV	54	2.3	2.4	2.4	2.5
8	F/76/TAV	59	2.3	2.4	2.4	2.5
9	F/55/TAV	50	2.3	2.4	2.4	2.5
10	M/69/TAV	59	2.6	2.6	2.6	2.6
11	M/58/TAV	55	2.0	2.0	1.9	1.9
12	M/68/BAV	49	1.7	1.8	1.9	1.8
13	M/81/TAV	74	1.7	1.7	1.9	1.8
14	M/69/BAV	52	2.5	2.5	2.5	-
15	M/66/TAV	61	2.8	2.8	-	2.8
16	M/78/TAV	47	2.3	2.1	-	2.2
17	M/78/BAV	57	2.2	2.2	2.2	2.1
18	F/46/BAV	53	2.2	2.2	2.2	2.1
19	M/54/BAV	53	1.4	1.4	1.5	1.4
20	M/69/TAV	60	2.2	2.2	-	2.2
21	F/68/BAV	55	2.2	2.2	2.2	2.1
22	F/66/TAV	52	-	2.5	-	2.3
23	M/76/TAV	55	1.8	2.2	2.3	2.0
24	M/78/TAV	53	2.8	3.3	3.2	3.5
25	M/80/TAV	56	2.8	3.0	3.0	2.3
26	F/77/TAV	60	2.0	2.0	-	2.0
27	M/79/TAV	46	1.9	2.1	2.0	1.9
28	F/79/TAV	49	2.0	2.0	1.8	2.0
29	M/86/TAV	59	2.0	2.5	2.0	2.5
30	M/71/BAV	51	2.8	3.0	3.0	2.9
31	F/81/TAV	52	3.0	3.0	-	3.0
32	F/79/TAV	53	2.5	2.5	2.3	2.5
33	F/59/TAV	54	2.0	2.0	2.0	2.5
34	F/81/TAV	54	2.0	2.0	2.0	2.0
35	M/55/TAV	53	-	3.0	2.8	3.0
36	M/60/TAV	81	-	2.0	3.0	3.0
	69.9±9.6	54.5±7.3	2.24±0.44	2.34±0.50	2.32±0.47	2.39±0.71

3.2.2 Biaxial testing

Experimentally-related material properties from aneurysm tissue samples collected were estimated by equibiaxial mechanical testing using an ElectroForce TestBench system (TA Instrument, Boston, MA). Square specimens (15×15 mm) were anchored by sutures on specimen edge using small,

surgical fishhooks. These sutures were attached to the four electromagnetic motors of the biaxial system, aligning circumferential and longitudinal edges with the direction of stretching. Five black markers were placed on the side of the intimal tissue surface to evaluate engineering strains along testing directions using a digital video extensometer placed perpendicularly to the testing area. During biaxial loading, the specimen was submerged in a bath with 0.9% physiologic saline solution under a controlled temperature of 37 °C while a small preload (0.5 g) was set prior to the displacement-driven testing protocol. A constant speed of 1 mm/min was applied to each motor to stretch the specimen under equibiaxial conditions. Two 200 N load cells were used to record the force along with material directions. Data analysis to obtain stress and strain were calculated as defined in the next section.
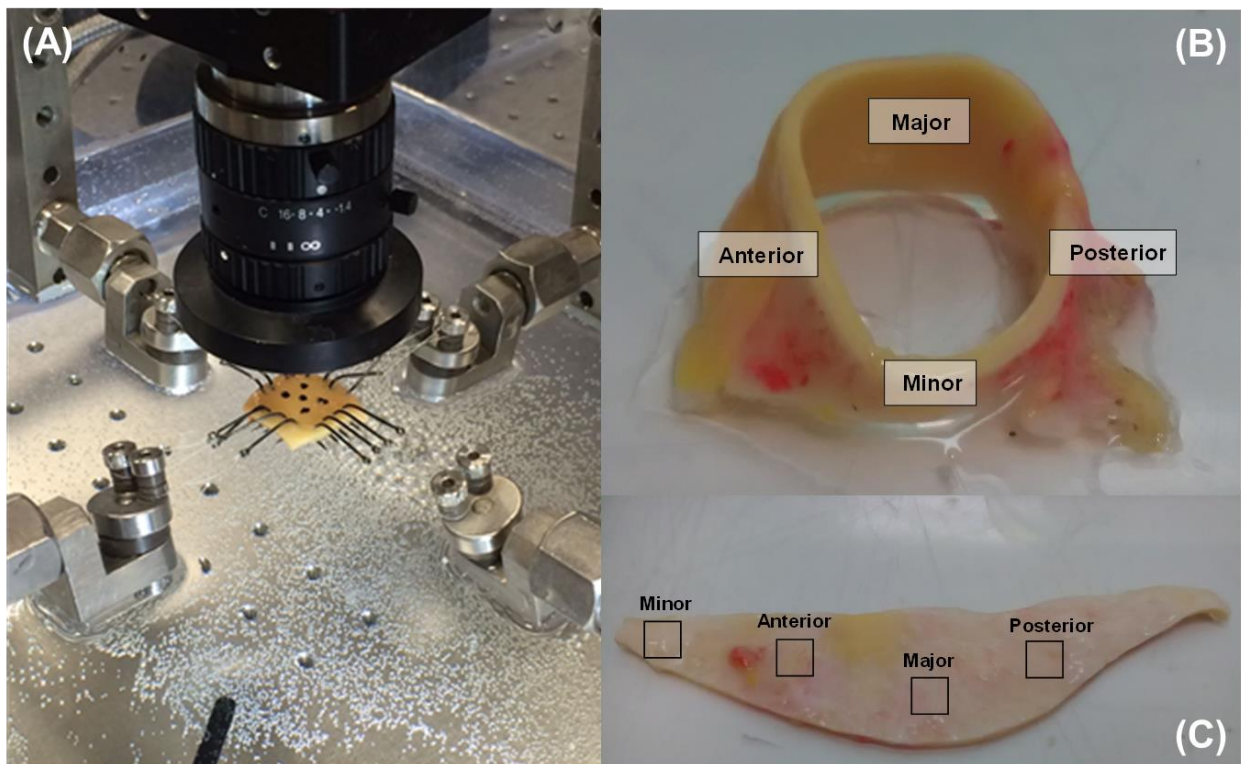
Figure 23 – (A) Equibiaxial testing device; (B,C) Picture of an ATAA tissue after collection: the anterior, posterior, major curvature, and minor curvature regions are shown in boxes.

3.2.3 Data analysis

From marker positions, the in-plane Green strain tensor was calculated as:

$$E = \frac{1}{2}(F^T F - 1) \tag{56}$$

where F is the gradient deformation tensor. For in-plane biaxial stretching, the in-plane Green strains are:

$$E_{\theta\theta} = \frac{1}{2}(\lambda_\theta^2 - 1) \tag{57}$$

$$E_{LL} = \frac{1}{2}(\lambda_L^2 - 1) \tag{58}$$

where λ_θ and λ_L are the circumferential and longitudinal stretches in the deformed equilibrium configuration, respectively.

The first Piola–Kirchhoff stress tensor P was calculated from measured loads and initial specimen dimensions so that nonzero components of P are:

$$P_{\theta\theta} = \frac{f_\theta}{H \, X_L} \tag{59}$$

$$P_{LL} = \frac{f_L}{H \, X_\theta} \tag{60}$$

where f_θ and f_L are the measured loads along each direction, X_θ and X_L are the unloaded specimen dimension along each direction, and H is the averaged specimen thickness in the unloaded reference configuration.

3.2.4 Constitutive modeling

Soft tissues are primarily composed of water and have negligible permeability, resulting in an incompressible material. Blood vessels undergo finite deformations under normal and pathological conditions. For this reason, ATAA tissues can be considered elastic, homogenous, hyperelastic, and incompressible, with the stress-strain material response mathematically described by a constitutive equation derived from scalar strain energy function W:

$$W = \frac{c}{2}(e^Q - 1) \tag{61}$$

with

$$Q = \left(b_1 E_{\theta\theta}^2 + 2b_4 E_{LL} E_{\theta\theta} + b_2 E_{LL}^2\right) \tag{62}$$

where c is a material parameter $[\frac{N}{m^2}]$ and b_1, b_4, b_3 are dimensionless parameters. The stress-strain data were fit to the following response functions, describing second Piola-Kirchoff stress tensors:

$$T_{\theta\theta} = 2ce^Q(b_1 E_{\theta\theta} + b_4 E_{LL}) \tag{63}$$

$$T_{LL} = 2ce^Q(b_4 E_{\theta\theta} + b_2 E_{LL}) \tag{64}$$

These response functions allow the interpolation of each stress component within the experimental strain range for $E_{\theta\theta}$ and E_{LL}. Fitting was performed with the nonlinear regression software package Hyperfit (v. 1.169, Brno, Czech Republic). For the Fung-exponential form, physically meaningful and plausible material parameters for the convergence of numerical solutions can be obtained by enforcing the convexity of the strain energy function and thus performing constrained minimization. For biaxial loading of soft tissue, strict convexity physically implies the projections of the contoured land only if $b_1 > 0$, $b_2 > 0$, and $b_4 > 0$.

3.2.5 Multiphoton imaging

For each aortic quadrant, square specimens (5×5 mm) for multiphoton imaging investigation were cut next to specimens used for biomechanical testing. Then, tissue specimens were fixed in 4% paraformaldehyde for 2 h approximately and stored in PBS solution at 4 °C temperature before imaging analysis. Samples were sealed in suitable chambered cover glasses. Three-dimensional (3D) image stacks were acquired at 1024×1024 pixel resolution using a Leica TCS SP5 confocal laser scanning microscope with a 40× oil objective (Leica Microsystems, Germany). The acquired image depth range was 20–60 µm with Z steps of 2 µm. The two-photon excitation (Spectra-Physics Mai-Tai Ti:Sa ultra-fast laser) was set at 880 nm. The Second Harmonic Generation (SHG) signal was detected in the range of 390–460 nm (green channel), whereas tissue autofluorescence was in the range of 485–650 nm (red channel). The scanning frequency was 400 Hz, with each image resulting from an average of 5 acquisitions. The green channel signal was mainly attributed to collagen fibers in SHG whereas the red signal channel was tissue auto fluorescence brighter signal for elastin fibers that is clearly distinguishable from the background.

3.2.6 Statistics

Tissue stiffness defined as the first derivative of the stress-strain response at a given point was obtained at two stress levels for comparison. Specifically, physiological and supraphysiological tissue stiffnesses were evaluated at 143 kPa and 242 kPa, considering a systolic blood pressure of 120 mmHg and hypertensive blood pressure of 180 mmHg, respectively. These stress levels were calculated based on the Laplace equation using the average thickness and diameter of ascending aorta

samples (see Table 3). Rank Sum test was used to compare clinical demographic data and assess differences in the material properties between BAV ATAA and TAV ATAA as well as material directions (i.e., circumferential, CIRC, and longitudinal, LONG, directions). One-way ANOVA, followed by Holm-Sidak posthoc test for all pair-wise comparisons, was used to assess differences in the stiffness values computed for each quadrant at both physiological and supraphysiological stress levels. The association of tissue stiffness with aortic diameter and patient age was explored via Pearson's correlation. For the Fung-type constitutive model, the coefficient of determination (R^2) and the normalized-root-mean-square error (NRMSE) were used as a measure for the "goodness of fit". Statistical analyses were performed using SigmaPlot (Systat Software Inc., San Jose, California), with statistical significance set to p=.05 in all cases. Data are shown as Mean ± SEM.

3.3 Results

Table 3 summarizes patient demographics and thickness measurements of aortic tissue specimens cut from each aortic quadrant. The distribution of age in BAV ATAA differs statistically from that of TAV ATAA patients (64.6 ± 9.7 years. for BAV ATAA vs 71.9 ± 8.9 years. for TAV ATAA, p=.037). There were no significant differences in the aortic diameter between BAV ATAA and TAV ATAA (50.7 ± 5.3mm for BAV ATAA vs 55.9 ± 7.5mm for TAV ATAA, p=.054) as well as the specimen thickness among each aortic quadrant and patient groups (2.1 ± 0.4mm average thickness for BAV ATAA and 2.3 ± 0.5mm average thickness for TAV ATAA, p=.349). Experimental raw data obtained from equibiaxial stretching of BAV ATAA and TAV ATAA tissue samples are reported for each region as stress-strain plots in CIRC and LONG directions as shown by Figure 24 and Figure 25, respectively.
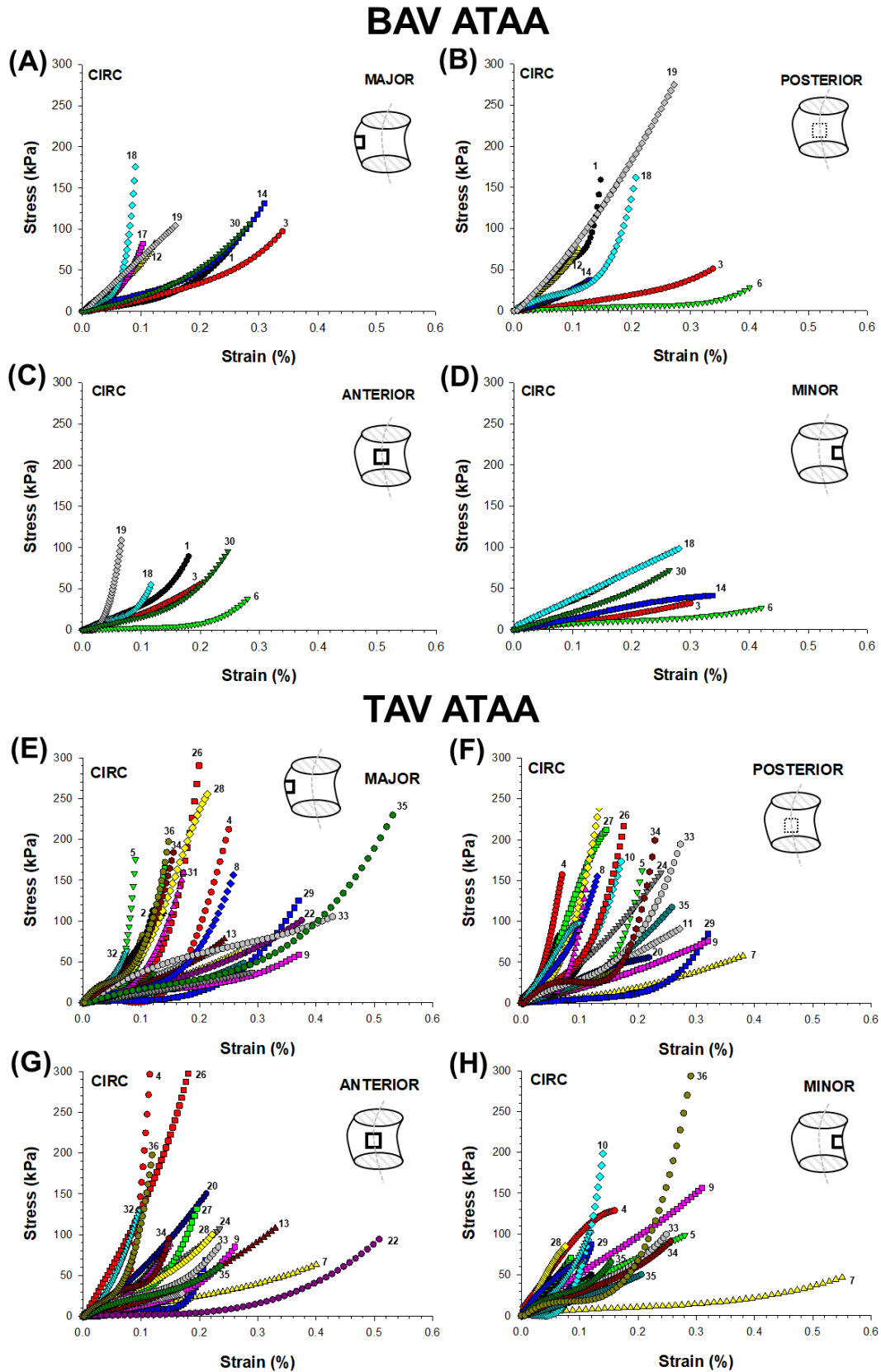
Figure 24 – Equibiaxial raw stress-strain data from each quadrant (A,B,C,D) BAV ATAA and (E,F,G,H) TAV ATAA tissues in the CIRC direction. Each ID number represents the experimental raw data obtained from different patients.

46
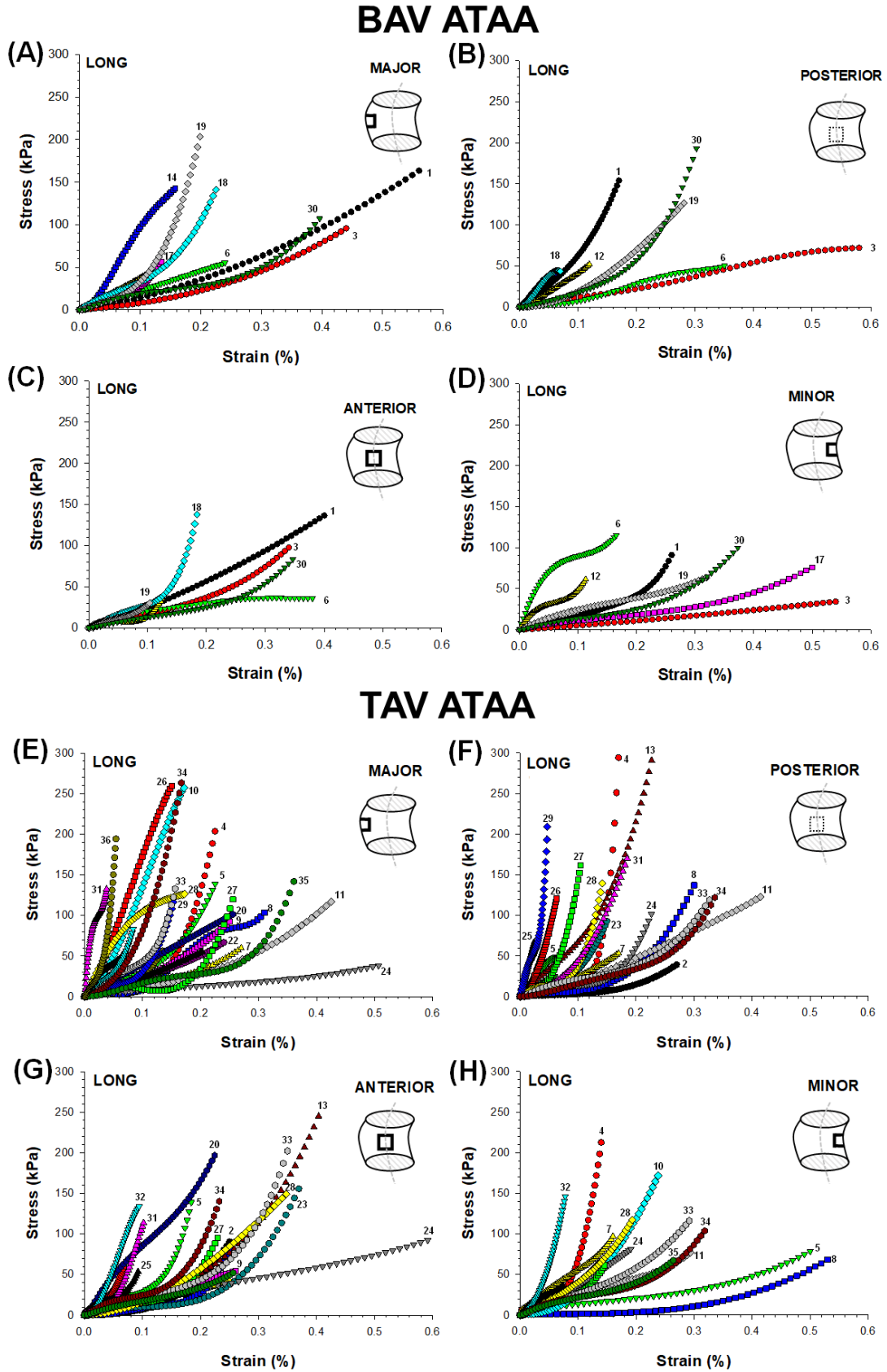
BAV ATAA

TAV ATAA

Figure 25 – Equibiaxial raw stress-strain data from each quadrant (A,B,C,D) BAV ATAA and (E,F,G,H) TAV ATAA tissues in the LONG direction. Each ID number represents the experimental raw data obtained from different patients.

Stress-strain profiles under equibiaxial loading exhibited a nonlinear and hyperelastic mechanical response, which is independent of aortic valve morphotype, aortic quadrant, and loading direction. Stress-strain data were fit to the Fung-type constitutive equation, and average material coefficients obtained from the fitting optimization are reported in Table 4. Material parameters were successfully recovered upon 60% of Green strain. Fits provided values of coefficient of determination ranging between 0.83 and 0.99, thus suggesting a satisfactory fitting of equibiaxial stress-strain profiles.

Table 4 - Constitutive material parameters of Fung's type material model resulting from the fitting of experimental stress-strain response.

	c (kPa)	b1	b2	b4	R^2	NRMSE
BAV						
Major	46.8 ± 74.2	27.2 ± 43.9	12.5 ± 24.1	-2.2 ± 14.9	0.98-0.99	0.01-0.17
Minor	17.4 ± 12.3	3.3 ± 4.8	0.7 ± 1.8	4.3 ± 10.1	0.94-0.99	0.02-0.51
Posterior	27.2 ± 19.3	20.7 ± 44.5	5.7 ± 14.9	-2.3 ± 2.7	0.86-0.99	0.01-0.36
Anterior	42.6 ± 58.5	4.2 ± 4.5	6.4 ± 16.6	-0.1 ± 2.6	0.94-0.99	0.01-0.31
TAV						
Major	34.6 ± 30.3	19.3 ± 46.9	6.4 ± 13.7	1.8 ± 4.2	0.91-0.99	0.01-0.62
Minor	79.4 ± 142.3	21.6 ± 28.1	14.4 ± 19.8	23.8 ± 83.3	0.88-0.99	0.02-0.35
Posterior	73.5 ± 115.9	19.4 ± 30.7	12.0 ± 22.2	1.6 ± 5.1	0.88-0.99	0.02-0.37
Anterior	42.0 ± 67.6	29.9 ± 45.0	12.8 ± 33.4	1.5 ± 4.8	0.83-0.99	0.03-0.74

For BAV ATAA and TAV ATAA, average tissue stiffnesses calculated as the mean values of all aortic quadrants at both 143 kPa and 242 kPa are shown in Figure 26. At both physiological and supraphysiological stress levels, there was no statistical difference on average stiffness of BAV ATAA as compared to that of TAV ATAA in either LONG (eg, 567.8 ± 181.1 kPa for BAV ATAA and 739.9 ± 371.2 kPa for TAV ATAA at 143 kPa, p=.176) and CIRC (eg, 660.4 ± 369.9 kPa for BAV ATAA and 761.5 ± 325.1 kPa for TAV ATAA at 143 kPa, p=.427) directions of material stretching.
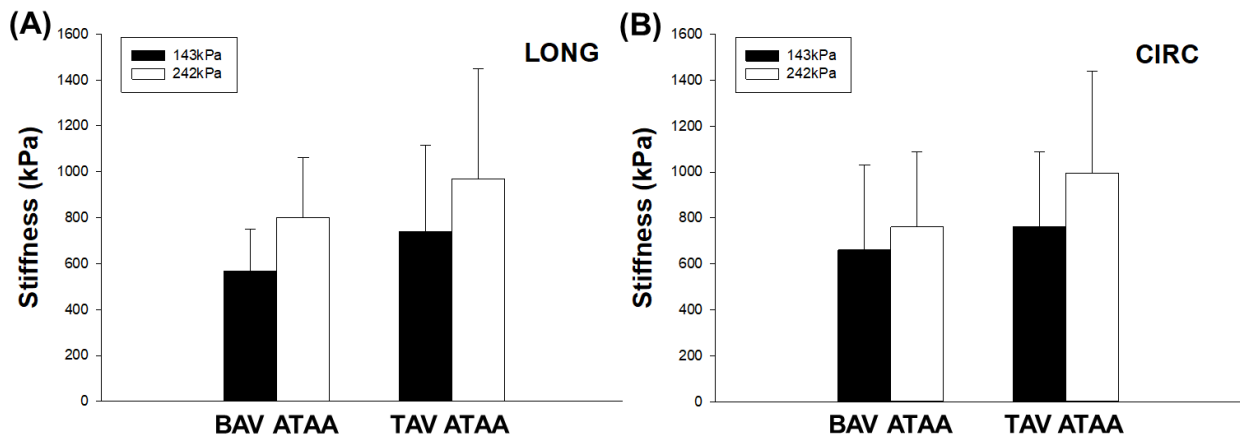
Figure 26 – Average stiffness values of BAV ATAA and TAV ATAA specimens at 143 KPa (black bar) and 242 kPa (white bar) in (A) LONG and (B) CIRC directions.

Regional heterogeneity of ATAA tissue stiffness revealed that the major curvature of the ascending aorta with BAV is statistically less stiff than that of TAV patients in the CIRC direction at both 143 kPa (276.6 ± 137.0 kPa for BAV ATAA and 733.2 ± 391.1 kPa for TAV ATAA, p=.001) and 242 kPa (355.5 ± 189.5 kPa for BAV ATAA and 965.7 ± 533.0 kPa for TAV ATAA, p=.001) as shown by Figure 27. We also found that the major curvature of BAV ATAA is less stiff than the anterior quadrant of the tissue specimen collected from the same patient at both 143 kPa (276.6 ± 137.1 kPa for BAV ATAA and 830.1 ± 557.1 kPa for BAV ATAA, p=.024) and 242 kPa (355.5 ± 189.5 kPa for BAV ATAA and 1197.1 ± 804.8 kPa for BAV ATAA, p=.017), suggesting a local weakening of ATAA wall.
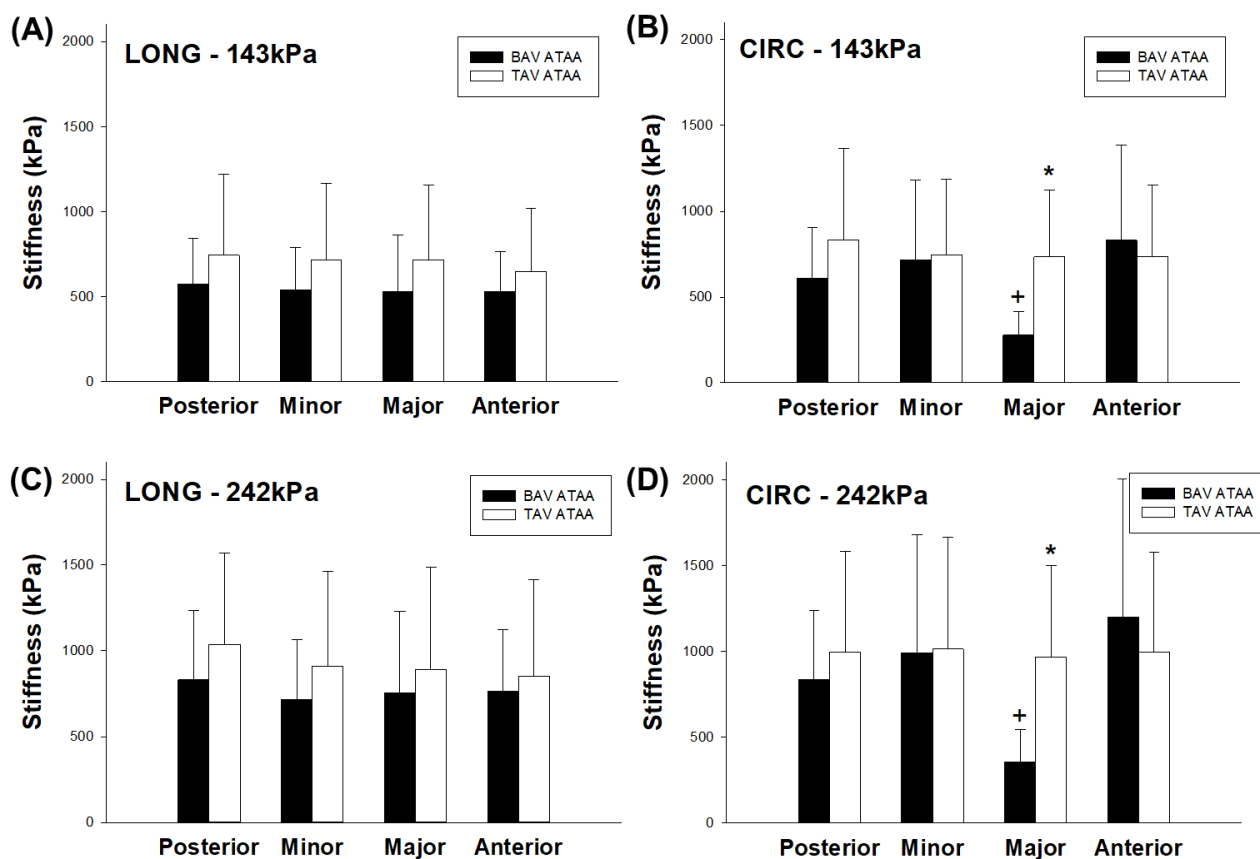
Figure 27 – Comparison of average tissue stiffness of BAV ATAAs and TAV ATAAs at (A) 143 kPa in LONG direction; (B) 143 kPa in CIRC direction; (C) 242 kPa in LONG direction; (D) 242 kPa in CIRC direction.

There was no statistical difference in the mean values of tissue stiffness for other aortic quadrants. Correlations of ATAA tissue stiffness with patient age and aortic valve diameter are shown in Figure 28. Correlations were evaluated at physiological and supraphysiological stress levels and, when observed, were statistically relevant at both levels. Aortic tissue stiffness value was positively correlated to the patient age of TAV ATAAs (R=0.492 and p=.0106 at 143 kPa), but not significantly for BAV ATAAs (R=0.102 and p=.780 at 143 kPa). A significant positive correlation was found between tissue stiffness and aortic diameter for BAV ATAAs (R=0.685 and p=.0289 at 143 kPa). A similar trend was observed between stiffness and aortic diameter for TAV ATAAs, although not statistically significant (R=0.182 and p=.373 at 143 kPa).
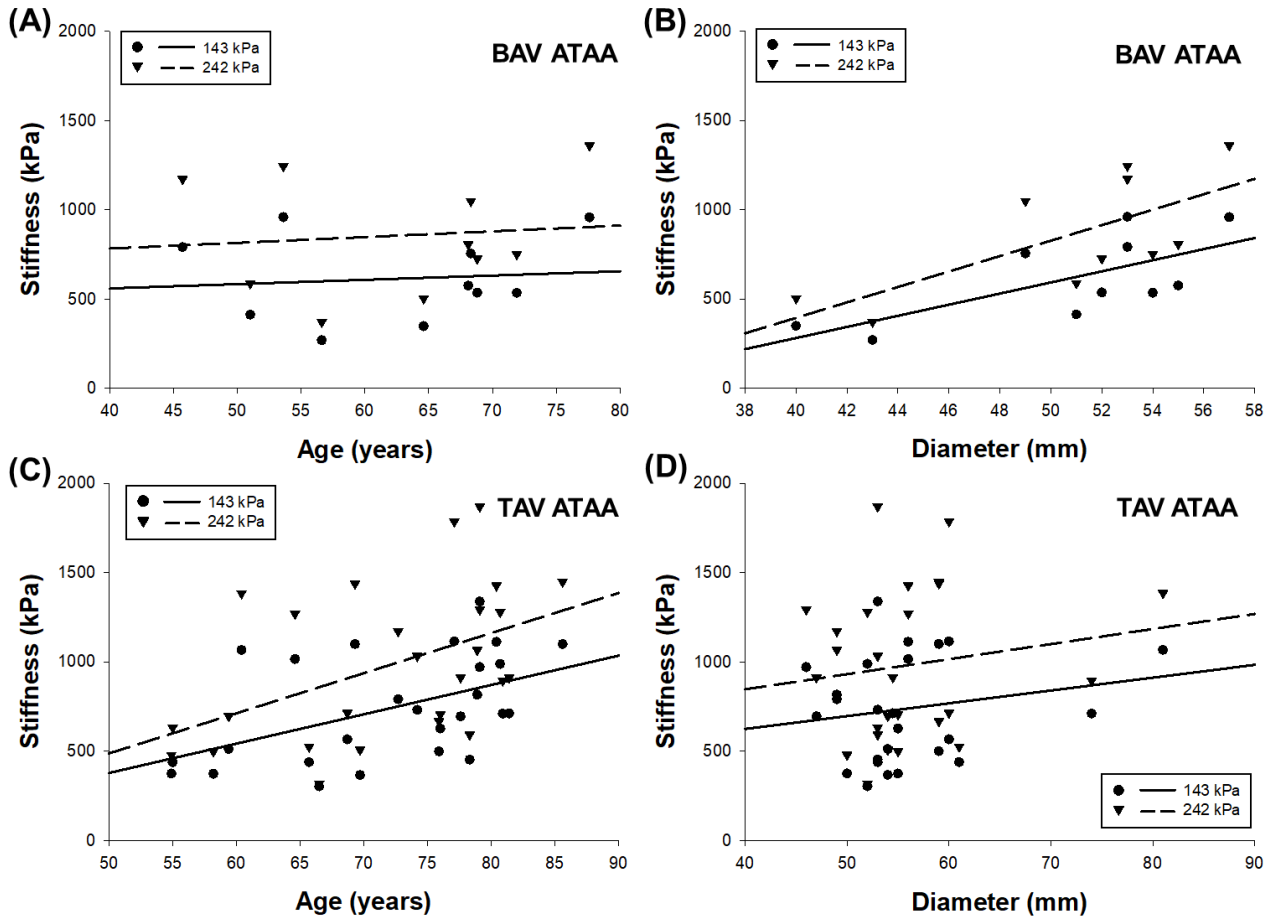
Figure 28 – (A) Correlation between stiffness and patient age for BAV ATAAs at 143 kPa (solid circles) and 242 kPa (solid triangles); (B) correlation between stiffness and aneurysm diameter for BAV ATAAs at 143 kPa and 242 kPa; (C) correlation between stiffness and patient age for TAV ATAAs at 143 kPa and 242 kPa; (D) correlation between stiffness and aneurysm diameter for TAV ATAAs at 143 kPa and 242 KPa.

Figure 29 shows the overlap of about 50 μm depth multiphoton images for each quadrant in both BAV ATAA and TAV ATAA tissue samples. A representative 3D reconstruction and Z-axis stack images movies are reported in Videos S1 and S2, respectively. The architecture of the aneurysmal aorta in either BAV or TAV is detected at the microscale and revealed that both elastin (red) and collagen (green) fibers are disorganized as compared to our previous investigation [88]. Elastin fibers appeared of the same thickness, being present both as thin straighter filaments and tick curly disorganized fibers. Differences in fiber length between BAV and TAV ATAA tissue samples cannot be assessed. For major, anterior and posterior quadrants, tissue samples of BAV ATAA highlighted elastin fibrils characterized by higher density, larger disorganization, and straight bans as compared to that TAV-related samples showing collagen fiber fascicles organized along a preferential direction and thickness of 20 μm.
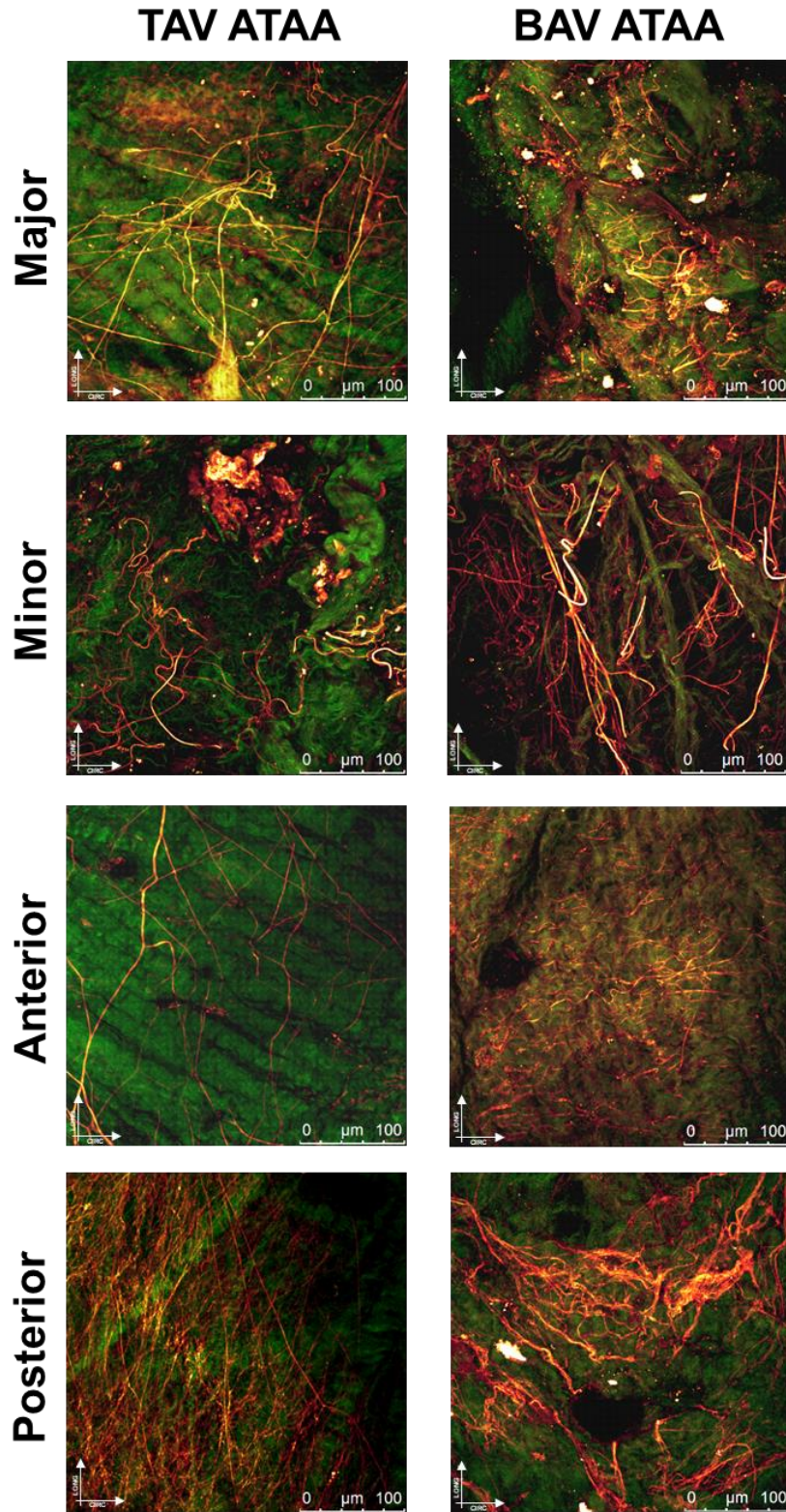
Figure 29 – Representative multiphoton microscopy measurement of BAV ATAA and TAV ATAA from anterior, posterior, major curvature and minor curvature (thickness of 50 μm); overlap of z-stack is reported; images acquired under laser excitation of λ_{ecx}=880 nm and SGH signal of collagen fiber in the range of 390-460 nm (green channel) and tissue autofluorescence in the range 485-650 nm (red channel) with elastin fibers clearly distinguishable from higher intensity and morphology.

3.4 Discussion

TAV ATAA tissue samples using planar equibiaxial material testing. Tissue behavior was quantified by tissue stiffness for all quadrants of the aneurysmal aorta, and direct comparison was done to assess regional heterogeneity of biomechanical properties of diseased aorta along the circumferential direction. The most striking finding is that the major curvature of aneurysmal aorta from patients with BAV is weaker than that observed on the anterior region and to that of TAV patients in the same quadrant. This is likely a consequence of mechanical weakening characteristics of bicuspid aortopathy caused by diverse pathogenetic inferences.

Although the aortic size criterion can be adjusted to achieve higher patient specificity using the body surface area, the surgical dilemma on the optimal timing for elective repair of an ATAA still exists because fatal complications can occur at aortic diameters lower than that dictated by current clinical guidelines [7]. There is therefore a need to delineate additional metrics, not based on aortic size, to better identify the risk of ATAA failure. Indeed, the maximum aortic diameter as a standard criterion for ATAAs is a surrogate geometric indicator of the imbalance between biomechanical stress and strength, which is what ultimately determines the rupture of dilated ascending aortas. Although a biomechanical approach is far away from clinical application, findings on the strength of ATAAs as here presented do not only elucidate the mechanobiology of this deadly pathology but can also lead to better patient stratification criteria for surgery.

There are two possible explanations for our findings: (1) the presence of the BAV-related morphology has led to hemodynamic disturbances locally increasing wall shear stress in the major curvature of the ascending aorta so that the prolonged exposure to aortic shear stress led to weakening of the aortic wall; (2) an inherent fiber defect due to genetic causes of bicuspid aortopathy has disorganized fiber architecture of extracellular matrix (as partially confirmed by multiphoton imaging) to determine aortic wall weakening and dilatation. While the first evidence is supported by the fact that bulged aortic dilatations are commonly seen in BAV patients at the time of surgery or CT imaging [89, 90], the second comment rises by studies documenting increased proteolytic activity in surgically resected BAV tissues showing the presence of thin, fragmented elastin fibers, reduced fibrillin-1 content, and decreased types I and III collagen in the major curvature of aneurysmal ascending aorta [91, 92]. Matrix metalloproteases (MMP) are also differentially expressed across different aortic sites in BAV patients, with high concentrations of MMP-2 and associated tissue inhibitor (TIMP-3) in the concavity of ascending aorta [93]. These differences were also documented by tissue changes on microRNA expression when comparing convex and concave portions of dilated aortas in BAV patients [94]. In contrast, several hemodynamic studies using 4D Flow MRI [95, 96] or computational

analyses [97-100] have elucidated that distinct aortic cusp fusion patterns of BAV phenotypes result in specific orientations of eccentric flow jets which in turn may lead to regionally located distributions of aortic shear stress, leading to adverse vascular remodeling and weakening of the aortic wall. This clinical evidence and histological changes are used to alternatively support the dichotomy between hemodynamic-mediated aneurysm progression versus the genetic theory of aortic dilatation. To our knowledge, this is the first study reporting the heterogeneity of aortic tissue stiffness of ATAAs with either BAV or TAV. Although several speculations are proposed, further studies are needed to univocally assess the main cause of tissue stiffness changes. Computational simulations based on virtual anatomic reconstructions of the ATAA geometry could potentially reveal whether the major curvature of the aneurysmal aorta of our BAV patients was exposed to high shear stress; however, only four patients underwent CT imaging in our hospital while others arrived from external centers. Familiarity for ATAA was reported by six patients but a genetic investigation was not undertaken in this study.

The heterogeneity of the ascending aorta is at two levels, that due to the layering along with the tissue thickness (ie, intima, media, and adventitia) and that due to each layer along the circumferential regions of the vessel (ie, anterior, posterior, major and minor curvature). Holzapfel et al. [52] reported different material properties and fiber angle for each aortic layer while Deveja et al. [101] revealed that layer-specific extensibility was significantly greater in BAV ATAAs than in TAV ATAAs, unaccounted by elastin/collagen content changes. On artificially dissected aortic tissue specimens, we found that the inner layers ruptured earlier than the outer layer [88], and then observed correlation with collagen fiber architecture assessed by multiphoton imaging [102]. Although multiphoton shown regional changes in the fiber architecture of each quadrant [103], several studies using uniaxial tensile testing did not highlight any regional changes in the elastic modulus and stress values at rupture of the ATAA wall but observed stiffness differences according to the material testing direction [101, 104, 105]. Comparison with our result is not straightforward, as we performed equibiaxial testing that is more appropriate for the membrane-like ascending aorta for uniaxial testing. In general, if the major curvature of the aneurysmal aorta is weaker than other quadrants, this is likely at high risk of complications. Regional variations of constitutive properties make also sense as they can be related to local tissue adaptation through growth and remodeling.

The fidelity of wall stress predictions is affected by changes in constitutive material parameters and fiber architecture along the circumferential direction of the aorta. In our opinion, regional heterogeneity has to be considered in patient-specific computational analyses of ATAA mechanics because, according to the equilibrium equation, the analysis of the wall stress in a curved ascending aorta indicates that the circumferential stress is much larger on the lower curvature of the aortic wall

than that of the greater curvature where rupture/dissection are clinically seen. If not considered, this geometrical nature of the aneurysmal ascending aorta can therefore lead to erroneous predictions of computational wall stress even if we account for layer heterogeneity by using a fiber-reinforced material model like that proposed by Gasser [106]. The difference in the material parameters here reported can be used in a rotationally symmetric dispersion model like that proposed by Holzapfel et al. [107] to account for regional heterogeneity and associated fiber changes.

Another relevant finding is the corroboration of tissue stiffness increase with patient age. Indeed, a loss of arterial elasticity is common in ascending aortic aneurysms as documented by two-dimensional speckle-tracking echocardiography [7], medical images analysis of dynamic CT images [8, 84], or bulge-inflation experimental testing [3]. These studies documented a not appreciable variation on ATAA tissue stiffness between BAV and TAV patients, suggesting that clinical management of BAV patients should be similar to that of the general tricuspid population. Strain-based rupture estimation relying on the imbalance between aortic strain and strength at rupture and have demonstrated that only a stiffer dilated aorta with increased blood pressure could significantly increase the risk of rupture [3, 5]. Less stiff aortic regions are, however, not necessary at the greatest risk of failure because of variability in the aortic wall strength (ie, the ability of the material to withstand a loading condition). The aortic strength is therefore an important determinant of ATAA failure and can be only estimated by ex-vivo mechanical testing.

This study has some limitations. Biaxial mechanical properties were not investigated for the non-aneurysmal aorta because of difficulties in collecting aortic tissues from organ donors or heart transplant recipients. The study of Azadani et al. [108] documents Fung-type material coefficient and tissue stiffness changes on healthy aortas, although with no details on regional heterogeneity. The biaxial mechanical protocol was extended to an equibiaxial loading condition whereas the full anisotropic behavior of the aorta can be captured varying the stress ratio in material stretching directions. Lastly, tissue stress levels were estimated based on the Laplace equation, which relies on cylindrical geometry rather than true ATAA geometry to determine wall stress. More accurate stress levels can be obtained by computational studies incorporating patient-specific ATAA geometries. Larger sample size for the BAV study group would be ideal to confirm observations, although statistical power was found relevant.

Chapter IV

Patient-Specific Computational Evaluation of Stiffness Distribution in Ascending Thoracic Aortic Aneurysm

The content of this chapter was published as a research article in Journal of Biomechanics by Di Giuseppe M., Farzaneh S., Zingales M., Pasta S., Avril S.

4.1 Background

Ascending thoracic aortic aneurysm (ATAA) is a life-threatening cardiovascular disease, leading to weakening of the aortic wall and permanent dilation. ATAA affects approximately 10 out of 100,000 persons per year in the general population [80], and this disease is associated with a high risk of mortality and morbidity [1]. Bicuspid aortic valve (BAV) is a predisposing risk factor to ATAA formation and development with patients having associated aortopathy on approximately 40% of the whole bicuspid population [20] and a higher rate of aortic dissection compared to patients with the tricuspid aortic valve (TAV) [81].

To avoid aortic complications (i.e. rupture or dissection), the current clinical management of ATAA is based on strict monitoring of the aneurysm size, and elective repair is recommended when aortic diameter reaches a critical size [82]. However, aortic size is not a sufficient predictor of the risk of ATAA failure [83]. Aortic stiffness is associated with progressive aortic dilatation and aneurysm formation as shown by imaging modalities [7, 109], computational analyses [4, 5, 8], and biomechanical studies [9, 10]. High aortic stiffness was associated with high rates of surgical aortic replacement and aortic root dilation in children and adults with connective tissue disorders [85]. In Marfan patients, aortic stiffness proved to be important in predicting progressive aortic dilatation [86, 110]. A recent study of abdominal aortic aneurysms found that segmental stiffening of the aorta preceded aneurysm growth and introduced the concept that stiffening may act as an early mechanism triggering elastin breakdown and aneurysm growth [87]. Imaging based on 4D Flow MRI [96], in silico computational modeling [99, 111], or a combination of them [112] have confirmed an altered hemodynamic environment in BAV ATAAs with well-functioning or stenotic aortic valve leaflets [113]. The underlying hypothesis is that flow disturbances induce local wall shear stress (WSS) forces on the dilated aorta, portending to adverse vascular remodeling by mechanotransduction. This can further lead to changes in the biomechanical properties of ATAA wall as reflected by an increased stiffness for the dilated aorta.

Risk assessment based on the aortic stiffness of the ATAA wall is being developed [3, 5, 114]. In this way, the quantification of local elastic properties of the ATAA wall from in vivo data is crucial to establish a reliable method for estimating the severity of an ATAA [115, 116]. Most importantly, new strategies of risk assessment should be accurate and compatible with the clinical time framework. For that purpose, the in vivo non-invasive identification of aortic stiffness would be essential for clinicians to improve the clinical decision making process. Recently, Farzaneh et al. [4] have presented a novel methodology, namely the LESI (local extensional stiffness identification) methodology, to non-invasively quantify local stiffness properties based on ECG-gated CT scans and brachial arm pressure. The interrelationship between the obtained local stiffness with other established markers of aortic function remains unclear and this currently limits the methodology's potential impact. The current study aimed to determine the most sensitive markers of local ATAA stiffness estimation with the hypothesis that direct measures of local ATAA stiffness could better detect the high-risk patients. First, the patterns of extensional stiffness obtained by the LESI methodology in a cohort of 30 patients with ATAAs and different aortic valve phenotypes were analyzed. Then, the association of stiffness with demographic data and computationally derived wall shear stress (WSS) was investigated.

4.2 Methods

4.2.1 Study Population

After internal review board approval and informed consent, 30 patients (12 BAV and 18 TAV) referred for aortic size evaluation by electrocardiographic-gated computed tomography (ECG-gated CT) were enrolled. Table 5 shows demographic data of the patient population as well as aortic diameter. For all patients, ECG-gated CT scans were performed after intravenous injection of contrast agent to improve image quality. Imaging was carried out on a GE VCT 64-channel scanner (GE Medical Systems, Milwaukee, Wisconsin), with a gantry rotation velocity of 0.5 m/s and spiral pitch of 0.984. Retrospective reconstruction of images was performed to obtain images at cardiac phases corresponding to both end-diastole and end-systole at the resolution of 512 x 512 and slice thickness of 0.625 mm. Before imaging, diastolic and systolic blood pressures were measured by brachial sphygmomanometer for each patient.

Table 5 – Demographic and clinical data.

ID	Sex	Valve	Age [years]	Systolic Pressure [mmHg]	Diastolic Pressure [mmHg]	Aortic Diameter [mm]
1	M	TAV	56	140	74	45.9
2	M	TAV	55	136	76	41.7
3	M	BAV	62	135	77	40.13
4	M	BAV	43	125	88	36.32
5	M	BAV	48	135	85	42.15
6	M	TAV	71	145	70	50.5
7	M	BAV	58	150	70	48.04
8	M	TAV	73	100	77	47.3
9	M	TAV	61	180	86	43.5
10	M	TAV	67	136	75	49.05
11	M	TAV	67	140	80	45.01
12	M	TAV	68	122	70	46.27
13	F	TAV	83	150	75	42.23
14	M	TAV	65	116	73	46.1
15	M	TAV	61	136	70	44.8
16	M	BAV	48	130	80	37.2
17	M	BAV	49	136	75	28.56
18	M	TAV	68	129	77	40.27
19	M	TAV	53	126	72	46.7
20	F	TAV	64	144	68	44.67
21	M	TAV	73	144	84	48.47
22	M	BAV	41	136	75	30.13
23	M	BAV	42	131	68	46.59
24	M	TAV	64	120	80	37.43
25	M	BAV	48	148	90	47.05
26	M	TAV	64	130	80	37.71
27	M	BAV	45	124	78	49.21
28	F	BAV	61	144	77	48.36
29	F	TAV	52	125	70	42.1
30	M	BAV	58	136	76	40.86
			58.9±10.4	135.0±13.8	76.5±5.8	43.1±5.4

4.2.2 Image Analysis

For each patient, segmentation of ECG-gated CT images was performed at both diastolic and systolic phases using Mimics v20 (Materialise, Leuven, BE). Specifically, semi-automatic threshold-based segmentation of the aortic lumen was performed to obtain a point cloud of ATAA geometries. The same smoothing factor was applied to all phases. The three-dimensional (3D) surface of the aorta was generated for each phase and exported as STL file. Then, 3D aortic surfaces reconstructed at both cardiac phases were cut by identical cross-sectional planes in Rhinoceros (Robert McNeel & Associates, Seattle, USA) to define a domain of the aorta larger than the final segment of interest. A

set of nodes was defined across each reconstructed aortic geometry, with the requirement that a node represented the position of the same material point at each phase of the cardiac cycle. For this, it was essential to reconstruct a structural mesh for all phases with an identical number of elements and nodes. The Vascular Modeling Toolkit (VMTK, Orobix, Bergamo, Italy; www.vmtk.org) (Antiga and Steinman, 2004) was employed to generate the structural mesh from STL files. The extracted data from VMTK were post-processed in MATLAB to extract an accurate mesh using the longitudinal and circumferential metrics obtained from VMTK. A structural mesh composed of 3871 quadrilateral shell elements, 49 along the circumferential direction and 79 along the longitudinal direction, was defined on the template geometry. Each node of the structural mesh was related to assumedly the same material points for systole and diastole phases.

The LESI methodology for calculating the extensional stiffness was described by Farzaneh et al. [4]. In brief, local principal strain components (ε_1 and ε_2) were deduced by computing the spatial gradients of displacements between diastolic and systolic configurations. Although the aortic tissue is globally anisotropic and nonlinear, its mechanical behavior was linearized in the range of strains induced by pressure variations between diastole and systole, and anisotropic effects were neglected in this range. The local principal stress components (τ^0_1 and τ^0_2) were derived by finite-element analysis (FEA) performed on the ATAA diastolic geometry using average blood pressure evaluated over the cardiac cycle (Joldes et al., 2016). To obtain radii of curvature (r^0_1 and r^0_2) and their variations (Δr_2 and Δr_1) fast and efficiently, a method based on the principle of virtual work was developed, as previously introduced in Bersi et al. [117].

Finally, it was possible, for each element, to relate the extensional stiffness to the pulsed pressure ΔP such as:

$$Q = \frac{\Delta P + \frac{\tau^0_1 \Delta r_1}{(r^0_1)^2} + \frac{\tau^0_2 \Delta r_2}{(r^0_2)^2}}{\frac{\varepsilon_1 + \nu \varepsilon_2}{r^0_1} + \frac{\nu \varepsilon_1 + \varepsilon_2}{r^0_2}} \tag{65}$$

In the current study, we used the concept of "extensional stiffness" (intensive property) which equals the material stiffness times the thickness and whose dimension is MPa.mm.

The aortic thickness could not be measured accurately due to the limited spatial resolution of CT.

Once LESI results were obtained for each patient, the average extensional stiffness was evaluated in each of the four quadrants, including the major, minor, anterior, and posterior regions; quadrants are shown in Figure 30.
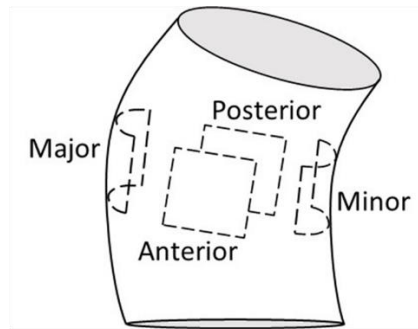
Figure 30 - Representation of ATAA: anterior, posterior, major, and minor regions are shown in boxes.

4.2.3 Computational Flow Analysis

Computational flow modeling was applied to study ATAA hemodynamics at systolic peak when the aortic valve is supposedly fully open [97]For each patient, the fluid domain of ATAA geometry at end-systole was meshed with unstructured tetrahedral elements with a size of 0.1 mm. The blood was assumed as a non-Newtonian incompressible fluid (density of 1060 kg/m^3 and viscosity of 0.00371 Pa*s) adopting the Carreau model [118, 119]. The solution was obtained with FLUENT v18 (ANSYS Inc., Canonsburg, PA) using the SIMPLE algorithm for the pressure-velocity coupling and second-order accurate discretization scheme. To include patient-specific hemodynamics conditions, the transaortic jet velocity evaluated by Doppler echocardiography was set as the inflow velocity condition at the aortic valve plane. For each outlet, we first computed the global vascular resistance and arterial compliance of each patient from echocardiographic measurements and clinical demographic data. Then, these parameters were used to compute the outflow boundary conditions of a three-element Windkessel model (comprising proximal resistance, compliance, and a distal resistance) coupled to each outflow branch. Boundary conditions were adjusted to match brachial artery pulse pressure.

After numerical solution, WSS values were obtained for the entire thoracic aorta, with further in-depth subanalysis in the ascending thoracic aorta by computing maxima at sinotubular junction (namely, analysis plane = AA1), proximal (AA2) and mid (AA3) ascending thoracic aorta for each quadrant (i.e., major, minor, anterior and posterior quadrants).

4.2.4 Statistical Analysis

The Rank Sum test was used to assess differences in the extensional stiffness between BAV ATAAs and TAV ATAAs. One-way Anova, followed by Holm-Sidak post-hoc test for all pair-wise comparisons, was used to assess differences of extensional stiffness among aortic quadrants. The

association of the extensional stiffness with patient age, aortic pulse pressure, aortic diameter, WSS, aortic strain, and stress was explored by Pearson's correlation. Statistical analyses were performed using SigmaPlot (Systat Software Inc., San Jose, California), with statistical significance set at p=0.05 in all cases. Data are shown as Mean ± SEM.

In addition, Principal Component Analysis (PCA) was performed for dimensionality reduction of all data computed for each patient. The first two principal components were analyzed to assess the separation of BAV ATAA versus TAV ATAA. The tolerance ellipse based on Hotelling's T2 at a significance level of 0.05 was calculated and shown in the score plots. Principal Component Analysis was performed using SPSS software (IBM SPSS Statistics v.17, New York, NY).

4.3 Results

Table 5 summarizes patient demographic data, systolic and diastolic pressures, and aortic diameter. The distribution of age in BAV ATAAs differs significantly from that of TAV ATAAs patients (50.2 ± 7.5 years for BAV ATAAs vs 64.7 ± 7.8 years for TAV ATAAs, p<0.01), and this difference was confirmed by the analysis of the age on a different cohort of 159 patients [120].
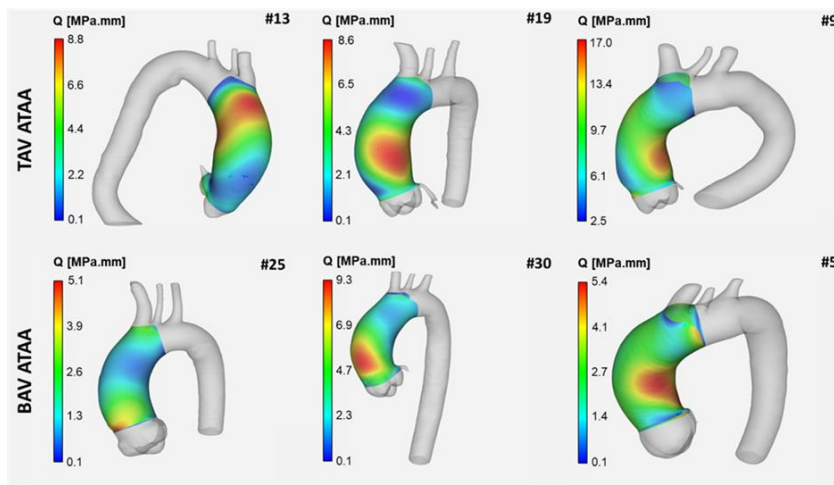
Figure 31 - Representative extensional stiffness maps of 6 patients reconstructed using LESI methodology for TAV ATAA and BAV ATAA patients.
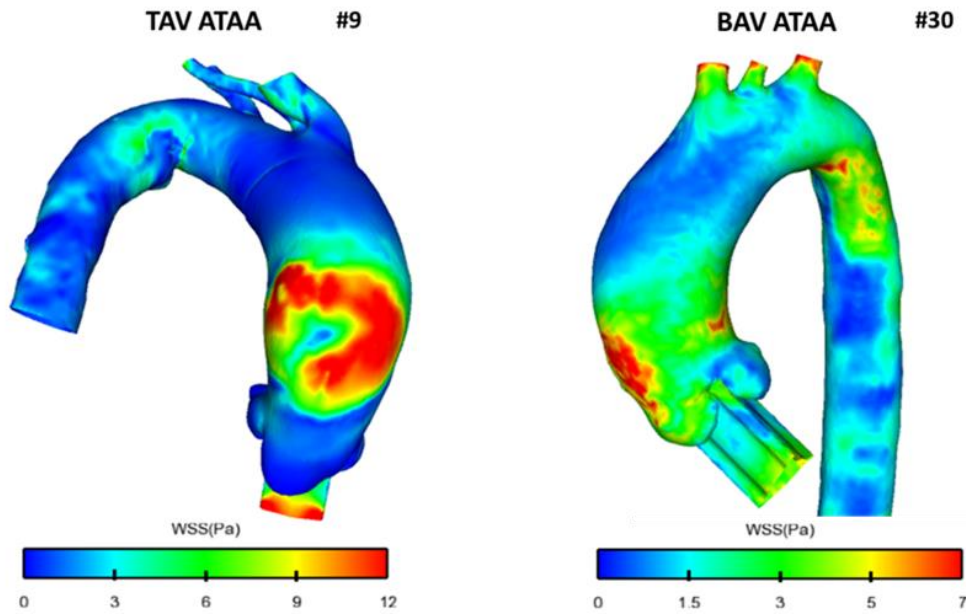
Figure 32 - Representative wall shear stress maps of 2 patients obtained by CFD analysis for TAV ATAA and BAV ATAA patients.

Figures 31 and 32 show representative extensional stiffness and WSS maps obtained by the LESI methodology and CFD analyses for BAV ATAAs and TAV ATAAs, respectively. There was no significant difference in the extensional stiffness (Q) between BAV ATAAs and TAV ATAAs (Q=3.6±2.5 MPa.mm for BAV ATAAs vs Q=5.3±3.1 MPa.mm for TAV ATAAs, p=0.094). Similarly, the mean values of the extensional stiffness did not significantly change among aortic quadrants, as presented in Figure 33, although many patients had high values of the extensional stiffness in the minor and anterior quadrants of the ascending aorta.
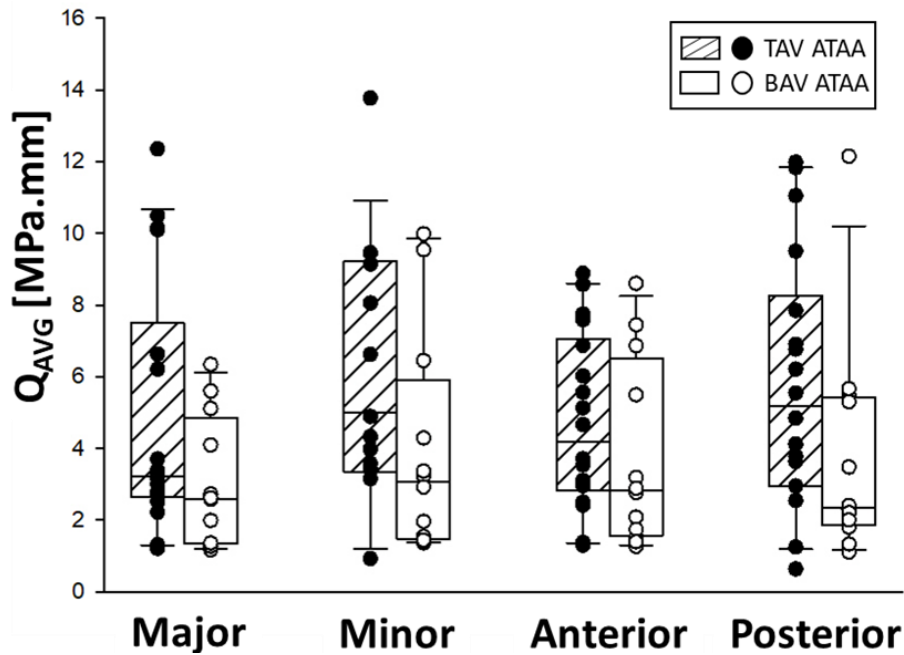
Figure 33 - Comparisons of average extensional stiffness of BAV ATAAs and TAV ATAAs evaluated at different quadrants.

The relationship of extensional stiffness as averaged among quadrants with the ascending aortic diameter and the aortic pulse pressure are shown in Figures 34A and 34B. A strong positive correlation was found between the extensional stiffness and the aortic pulse pressure (R=0.644 and p<0.001), but was not significant between the extensional stiffness and the aortic diameter (R=0.341 and p=0.065). Interestingly, a significant positive correlation was found between extensional stiffness and patients' age for BAV ATAAs (R=0.619 and p=0.032), but not for TAV ATAAs (R=-0.117 and p=0.645) as shown by Figures 34C and 34D. Figures 34E and 34F show the relationship of both strain and stress obtained in the circumferential direction with the average extensional stiffness. The extensional stiffness was inversely correlated with the circumferential strain (R=-0.522 and p=0.00324) and positively with the circumferential stress (R=0.474 and p=0.008). Correlation analysis of extensional stiffness with age, shown in Figure 34C, also revealed that BAV ATAAs can be divided into two subgroups: 1) patients younger than 50 years old who had a relatively low extensional stiffness, 2) patients older than 55 years old who had a relatively high extensional stiffness. All analyses in Figure 34 were also broken down by aneurysm type, results are reported in Figure 35.
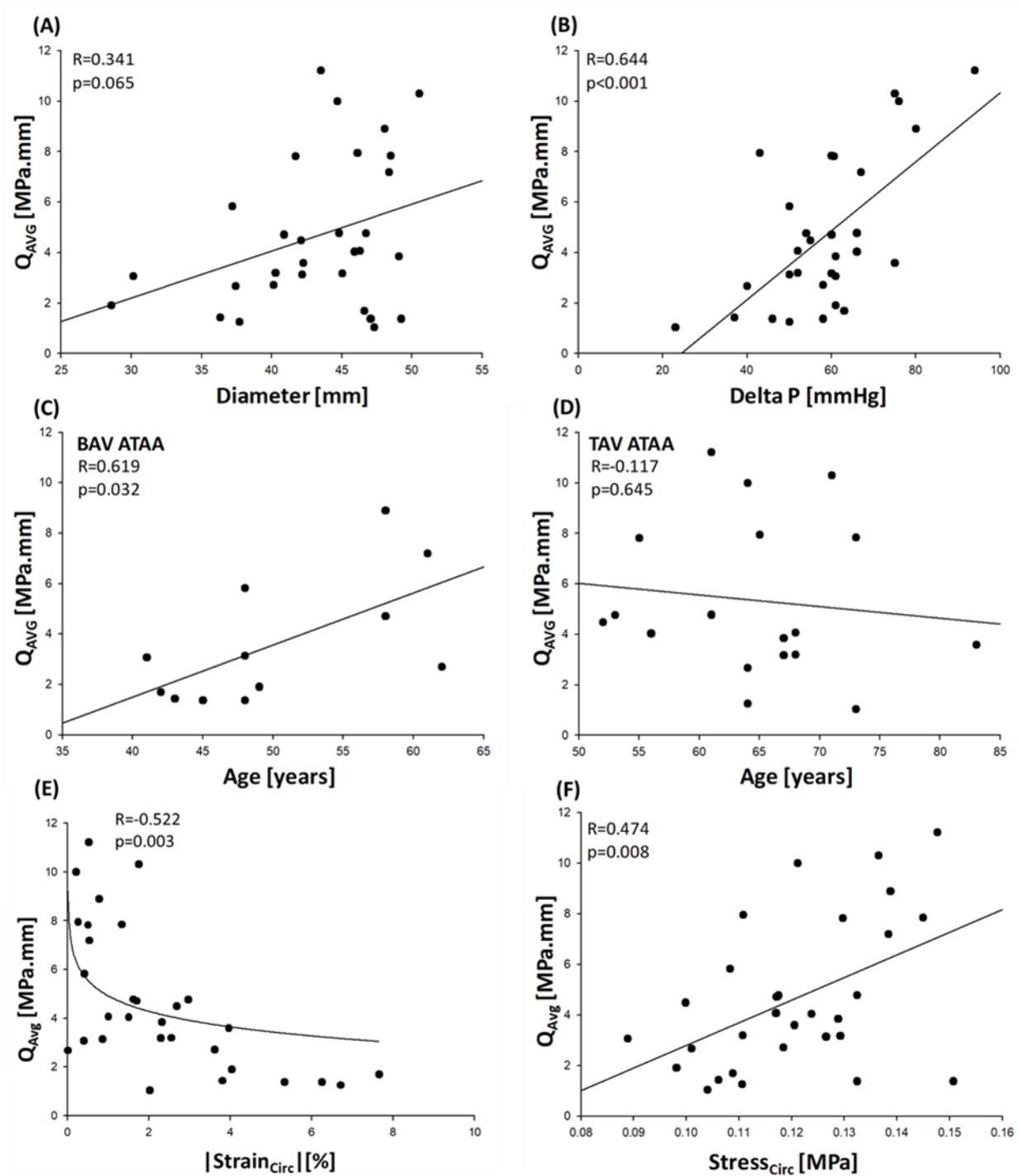
Figure 34 - (A) Correlation between average extensional stiffness and ascending aortic diameter; (B) correlation between average extensional stiffness and aortic pulse pressure; (C) correlation between average extensional stiffness and patients' age of BAV ATAAs; (D) correlation between average extensional stiffness patients' age of TAV ATAAs; (E) average extensional stiffness vs circumferential strain data with regression curve; (F) correlation between average extensional stiffness and circumferential stress.
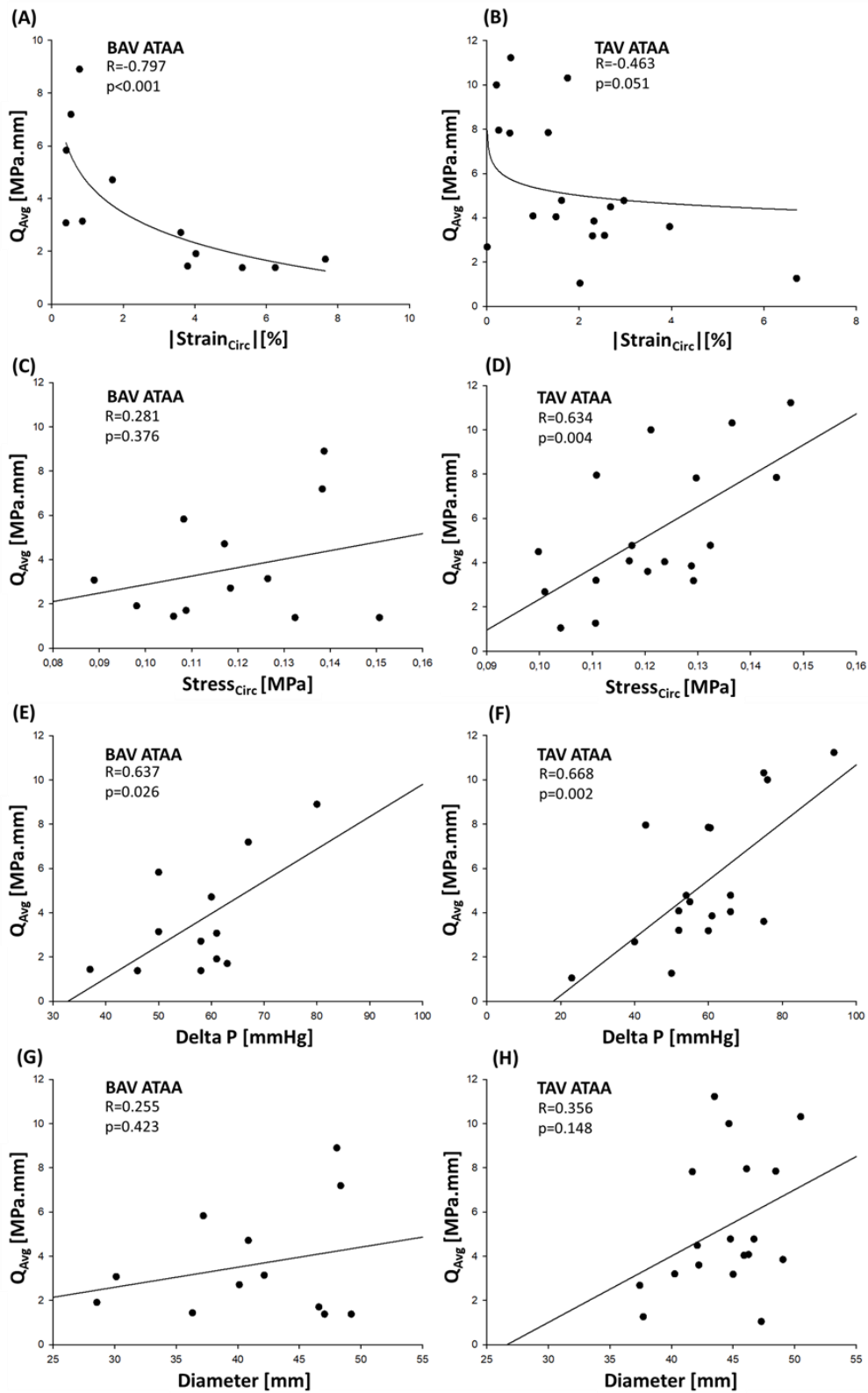
Figure 35 – Correlation between average extensional stiffness vs circumferential strain data with regression curve for BAV (A) and TAV (B) patients; correlation between average extensional stiffness vs circumferential stress for BAV (C) and TAV (D) patients; correlation between average extensional stiffness vs aortic pulse pressure for BAV (E) and TAV (F) patients; correlation between average extensional stiffness vs aortic diameter for BAV (G) and TAV (H) patients.

Peak systolic WSSs were correlated to the average extensional stiffness for each ascending aortic level and aortic quadrant. The correlation analysis between extensional stiffness and WSS values evaluated at proximal ascending thoracic aorta (AA2) appears promising (R=0.343 and p=0.080 for AA2), but no significant correlation was found between stiffness and WSS evaluated locally for Major, Minor, and Anterior quadrants. For the Posterior quadrant, a correlation was identified although the obtained p-value was very close to the threshold (p=0.05) and a low coefficient was obtained. Results are presented in Figure 36. All analyses were also broken down by aneurysm type, results are reported in Figure 37.
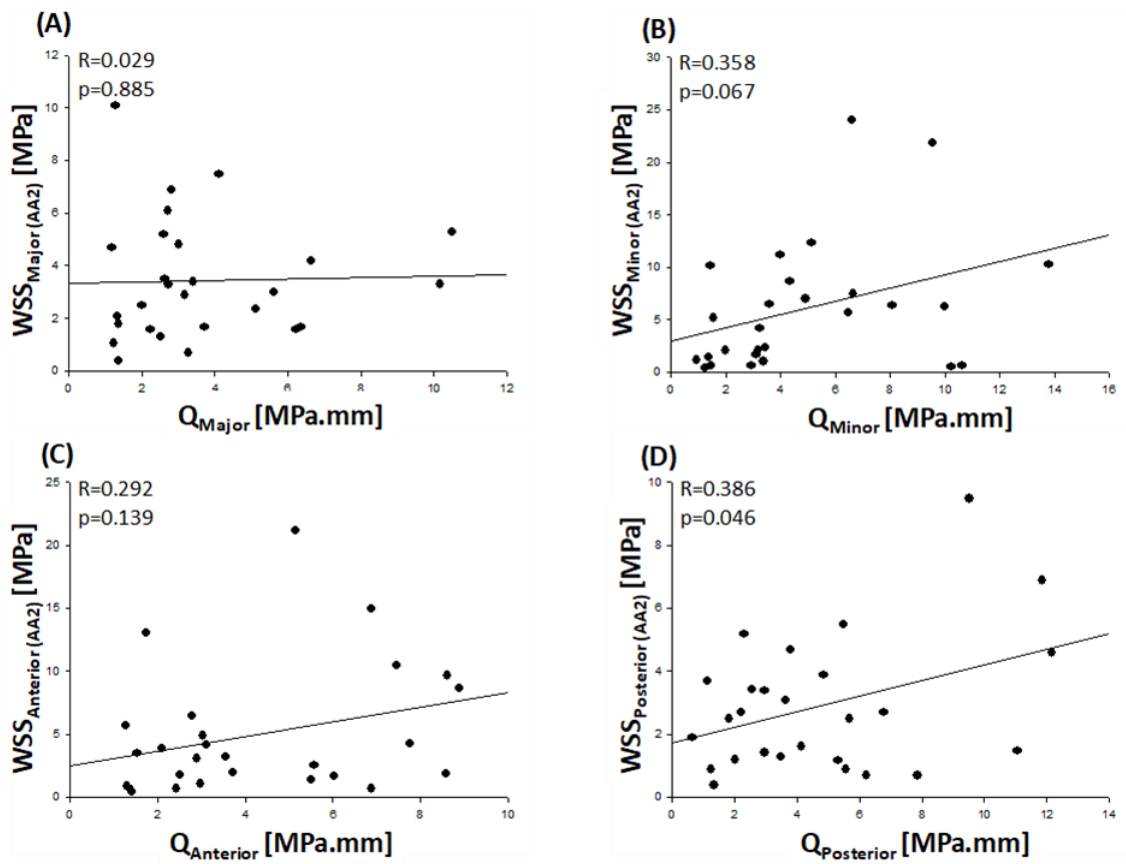
Figure 36 - Correlation between extensional stiffness and peak systolic WSSs evaluated at proximal ascending aorta from (A) major, (B) minor, (C) anterior, and (D) posterior regions.
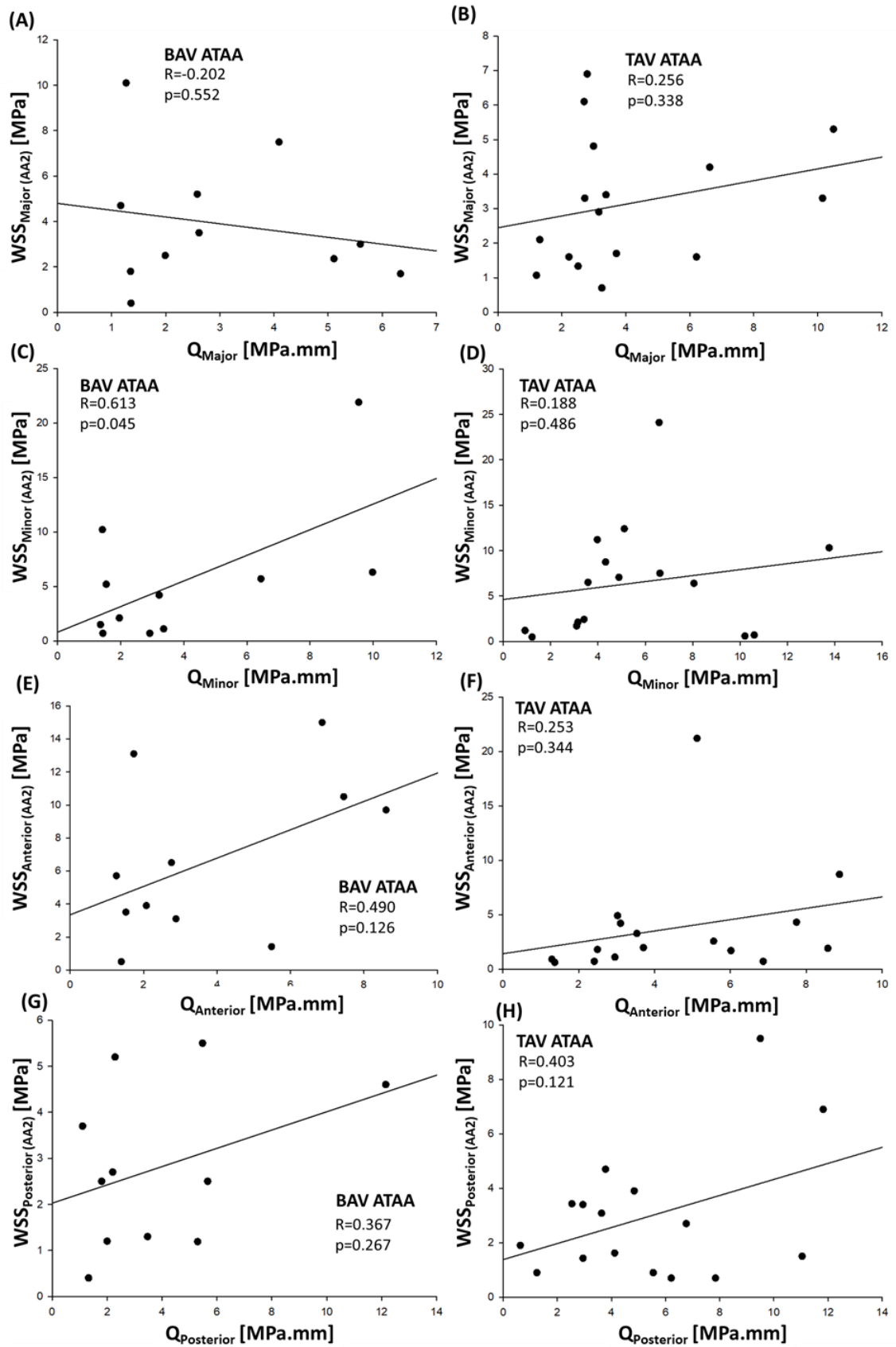
Figure 37 - Correlation between extensional stiffness and peak systolic WSSs evaluated at proximal ascending aorta from major, minor, anterior, and posterior regions for BAV (A,C,E,G) and TAV patients (B,D,F,H).

A PCA based on patient's age, aortic diameter, aortic pulse pressure, extensional stiffness, and WSS showed no separation of BAV ATAAs from TAV ATAAs, as shown in Figure 38. However, the loading plot revealed that the most important variables responsible for differences between BAV ATAAs and TAV ATAAs are the pulsed pressure and the patient's age.
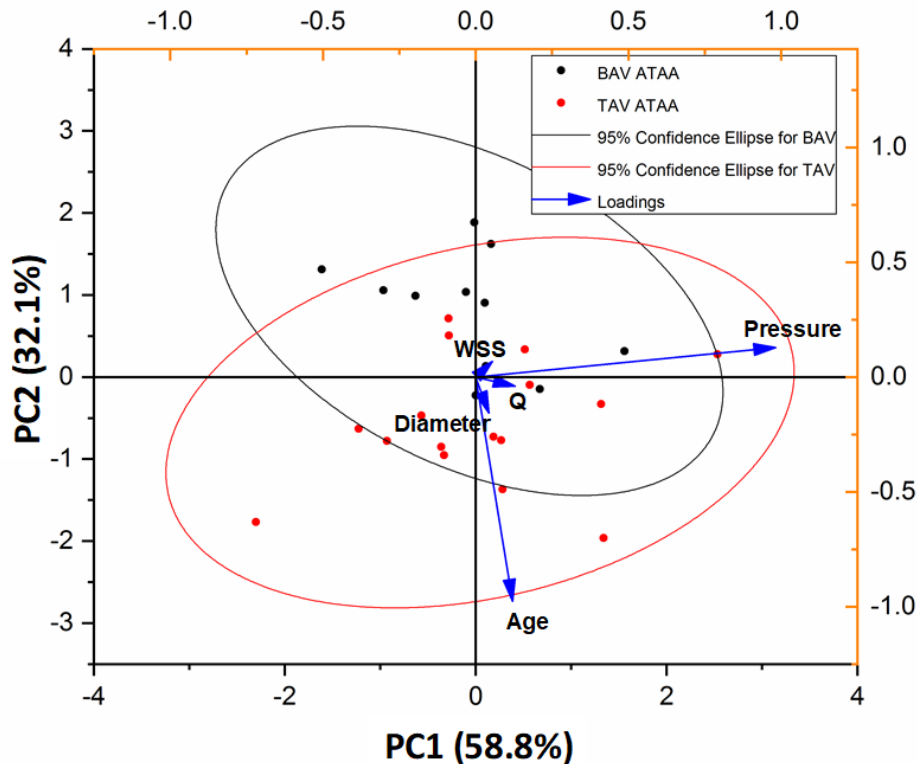
Figure 38 - Two-dimensional score plots of PC1 versus PC2 with loading showing the main variables responsible for clustering BAV ATAAs (black dots) from TAV ATAAs (red dots); the plot shows patient's age, aortic diameter, aortic pulse pressure, extensional stiffness, and wall shear stress. Solid lines represent 95% tolerance ellipse of TAV ATAAs (red color) and BAV ATAAs (black color).

4.4 Discussion

This study aimed to investigate the patterns of extensional stiffness from in vivo dynamic imaging of ATAAs and to evaluate potential correlations with clinical data and blood shear forces. The extensional stiffness did not show any significant difference between BAV ATAAs and TAV ATAAs. This supports recent evidence and observations for which there should be no distinction in the surgical management of BAV patients versus TAV patients [120]. Recently, we performed equibiaxial mechanical testing on ascending aortic tissues with either BAV or TAV [121] and found no difference in the mean values of the aortic tissue stiffness between BAV ATAAs and TAV ATAAs as reported here. However, other groups who performed mechanical testing on ascending aortic tissues found differences in the mean values of the aortic tissue stiffness between BAV patients and

TAV patients [122-126]. We did not measure the extensional stiffness in non aneurysmatic subjects as healthy subjects cannot undergo CT scans. However the stiffness of healthy aortas was measured by a variety of other techniques in the literature and values in a range between 150 kPa and 1000 kPa were reported, with ATAA exhibiting generally a higher stiffness than healthy aortas [108, 127].

The correlation of patients' age with the extensional stiffness obtained by the LESI methodology was strongly affected by the valve phenotype. For TAV patients, the extensional stiffness did not vary with the patient age but increased with the age of BAV patients. This is likely a consequence of the significant difference in the age of BAV versus TAV patients. Indeed, TAV ATAAs were older than 50 years while most patients with BAV were <50 years. We also found that BAV ATAAs can be divided into two subgroups: 1) patients younger than 50 years old who had a relatively low extensional stiffness, 2) patients older than 55 years old who had a relatively high extensional stiffness. Martin et al. [84] showed that the biomechanical properties of dilated ascending aorta change between 50 and 60 years, and this could explain either the difference in the extensional stiffness of two subgroups of BAV ATAAs or the lack of correlation between the extensional stiffness and patient age for TAV ATAAs.

As expected, no significant correlation was found between extensional stiffness and shear stress for the Major, Minor and Anterior quadrant, thereby suggesting there is no direct link between hemodynamics and biomechanical properties of ATAA wall. For the posterior quadrant, instead, a significant correlation was observed.

The extensional stiffness was significantly correlated with both the pulsed pressure and the circumferential strain and stress. Although these variables are directly involved in the derivation of the aortic stiffness in the LESI methodology, these significant correlations can also be interpreted with physiological principles.

Relations between the aortic stiffness and the pulsed pressure have been known for decades. Indeed, as the aorta becomes stiffer, the central pulsed pressure is higher due to the increase in the pulse wave velocity and the early return of reflected waves to the heart from following junctions [128]. In a young and healthy aorta, the reflected wave tends to hit the aortic root during diastole, serving to increase diastolic pressure and hence improving perfusion of coronary arteries. In aged and stiffened aortas, the reflected hits the aortic root earlier, increasing the systolic pressure and decreasing the diastolic one. The amplitude of reflected waves increases as the arterial stiffness increases, further augmenting central systolic pressure [128-133]. The effects of this supplemental load onto the aorta, which are direct expressions of the stiffness increase, should be reckoned for estimating the risk of rupture or dissection of ATAAs.

As expected, the extensional stiffness was also significantly correlated to the circumferential strain since circumferential strains are a direct expression of the aortic stiffness. Stiffening often triggers degradation and/or loss of a fraction of elastin fibers, leading to a reduction of the wall extensibility [134]. Another consequence is also a decrease of the axial stretch of the aorta, producing an increase of the aortic arch curvature named unfolding [135]. The degradation of protein networks in the extracellular matrix of ATAAs can be explained by the unbalance between protein synthesis by vascular cells and protein destruction by matrix metalloproteases (MMPs) [136]. In the cohort from which this study group was extracted, we found that the expression level of MMP-9 is altered in BAV ATAAs vs TAV ATAAs [137]. The significant correlation between extensional stiffness and stress is very common for fibrous soft tissues, owing to their exponential stress-strain curve [138]. This reflects the reorientation and straightening of collagen bundles upon loading [139].

When analyzing BAV and TAV ATAAs together, the PCA analysis suggested that BAV ATAAs are likely forming a cluster in the lower quadrants of the multivariate score plot in the direction of the loading associated with patient age. This is not surprising because BAV patients are known to commonly develop ATAA at a younger age than TAV [120, 136].

4.5 Limitations

The LESI approach relies on local equilibrium equations as it is based on the principle of virtual work [117]. As for the generalized Laplace's law, the LESI approach considers the local equilibrium between pressures and tensions in a membrane, indicating that the aortic wall experience no shear through the thickness. This may not be a realistic assumption in regions near the aortic branches but these were excluded from the analysis. The peripheral pulse pressure rather than central aortic pressure was used. However, the mismatch of aortic compliance between the brachial artery and the aorta should be likely reduced or even reversed with the advanced age of our patients. The effect of brachial blood pressure on the extensional stiffness evaluations will be likely minimal in this study. Validation of in silico modeling has to be established. A large sample size including BAV ATAAs matched with the age of TAV ATAAs would be ideal to confirm observations. Unfortunately, we could not compare results with those relatives of non aneurysmatic subjects because healthy control volunteers are not allowed to undertake multiphase gated CT scans due to x-ray radiations risks. We are trying to extend our methodology to other imaging modalities (ultrasounds, MRI).

Chapter V

In Vitro Measurement of Strain Localization Preceding Dissection of the Aortic Wall Subjected to Radial Tension

The content of this chapter was published as a research article in Experimental Mechanics by Di Giuseppe M., Zingales M., Pasta S., Avril S.

5.1 Background

Aortic dissection (AD) is an adverse condition of the aorta, which is typically described by a primary intimal tear on the aortic wall [11]. Dissections are commonly described as first propagating in the radial direction towards the medial layer, then it proceeds within the media, or between the media and the adventitia, causing the layers of the aortic wall to separate [140]. The separation allows the blood flow to enter the aortic wall, where a secondary channel, a so-called false lumen, is created. This leads to dilation and weakening of the wall of the false lumen with an increasing probability of fatal rupture, bleeding, or malperfusion [141, 142]. In the absence of intervention, acute aortic dissections have a mortality risk upon 90% with the majority of deaths occurring within 48h [143]. The incidence of spontaneous aortic dissections is reported to be 5–30 cases per million people per year and strongly depends on the presence of risk factors.

Although arterial dissection is a common pathology and a challenging clinical problem, the underlying biomechanics remain underexplored. The structural organization is prone to separation in a plane parallel to the lumen [144, 145], as elastin fibers, collagen bundles, and smooth muscle cells are organized in concentric lamellar units in the media layer [146].

Hypertension is the most common predisposing factor to AD [11, 147]. AD is frequent in patients harboring a thoracic aortic aneurysm (TAA). TAA is a life-threatening cardiovascular disease leading to weakening of the aortic wall and permanent dilation [1]. TAA is characterized at the tissue level by extracellular matrix degradation and biomechanical weakening of the aortic wall, ultimately leading to dilation and failure by rupture or dissection. The mortality of thoracic aneurysms is estimated to be 50% over 5 years [148]; nevertheless, AD can occur in the absence of an aortic dilatation [149].

The predisposition of TAAs to ADs can be related to the degradation of the aortic wall in TAAs. A better understanding of the biomechanical effects preceding dissection initiation is essential for

predicting such an adverse event on a patient-specific basis. Moreover, the predictability of patient-specific biomechanics-based computational models is hampered by uncertainty about boundary conditions and material properties in such complex situations [8, 99, 108, 149, 150]. Experimental studies that focused on ADs permitted to measure the strength of dissecting aortic tissues [88, 151-154] subjected to radial tension. Although the radial stress in an elastic cylinder subjected to an inflating pressure is negative, the radial stress can become positive in the aortic wall and possibly induce AD when glycosaminoglycans (GaGs) accumulate in the wall [155, 156]. However, to the best of our knowledge, the strain distribution across the aortic wall preceding a dissection has never been measured.

Optical coherence tomography (OCT) is an imaging modality of micrometric scale permitting the visualization of tissue microstructure at different sub-surface levels (high-resolution and cross-sectional images acquisition with a near-infrared light) [157-162].

OCT has been used for medical application studies (in vivo) and for bioengineering research (in vitro) to characterize soft and hard human tissues. This technique can be applied to quantify the mechanical properties of biological tissues [163, 164]. In experimental biomechanics, OCT can be potentially combined with digital image correlation (DIC) to perform material characterization by measurements of displacements and strains [163, 165]. Originating from experimental mechanics, DIC has now been applied in several scientific fields including biomechanics [163, 166-169]. DIC has been largely adopted to study the mechanical behavior of biological tissues because it offers non-contact full-field measurements, which are beneficial when studying anisotropic and inhomogeneous materials such as cardiovascular tissues [170, 171]. DIC usually requires an artificial speckle pattern to be applied to the object surface and tracked during deformation [166]. More importantly, the speckle quality strongly affects the success and accuracy of DIC analysis [117]. Ensuring appropriate speckle quality can be very challenging in soft tissues because of the moist and reflective surface. Different studies have been conducted so far using DIC to characterize the mechanical and structural properties of aortic tissue [172]. Regarding the aorta, few studies have applied the OCT technique [158, 173]. This scarcity of OCT studies on the aortic tissue can be explained by the main limitations of OCT, which are its penetration depth and image contrast. The penetration depth across the aorta is usually less than 500 μm for state-of-the-art commercially available OCT systems operating in the 1.3 μm wavelength range [147], whereas human or porcine aortas have a thickness of about 2 mm. These limitations of OCT are related to the scattering properties of biological tissues. To overcome these limitations, it is possible to apply a tissue clearing technique to increase the OCT imaging contrast and penetration capability [173, 174], although the clearing process can alter biomechanical properties of the aorta [155].

The goal of the present project is to introduce a new methodology combining DIC and OCT to measure strain fields in aortic tissues subjected to tensile loading along the radial direction. We first describe the experimental protocol and apply it to healthy porcine tissues, then the methodology is extended to ATAA human tissues as a first proof of principle for the evaluation of dissection predisposition.

5.2 Materials and Methods

5.2.1 Porcine Tissue Origin

In this study, aortic samples were collected from different segments of the aorta, as illustrated in Figure 39. A descending thoracic aorta was collected from a healthy pig. The Veterinary School of Lyon (Institut Claude Bourgelat) supplied the aortas in accordance with the recommendations of the ethics committee of VetAgro Sup (C2EA No 18) and animal testing regulation – Directive 2010/63/EU. The study and protocol were reviewed and approved by the ethics committee of VetAgro Sup (project approved under No 1546). Porcine aortas were cryopreserved after collection and stored at −24 °C before experimental testing.
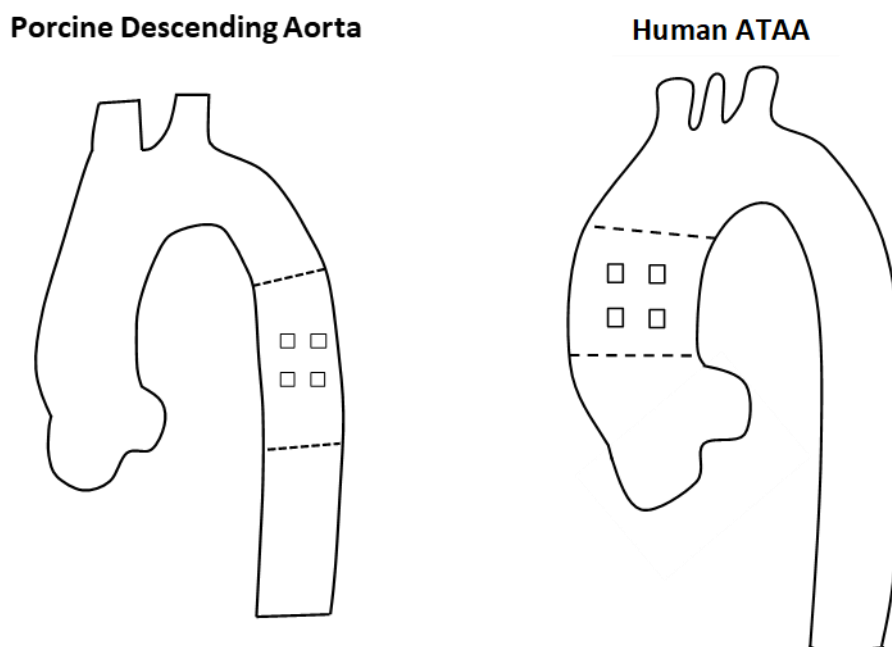
Figure 39 - Representation of the area of the aorta where samples are collected.

5.2.2 Human ATAA Tissue Origin

An ascending thoracic aortic aneurysm was collected from a patient undergoing elective surgery. The collection of the ATAA tissue was carried out in accordance with the guidelines of the Institutional Review Board of the University Hospital Center of Saint-Etienne, and the patient signed informed consent before surgery. The human tissue was cryopreserved after collection in a physiological saline solution and stored at −24 °C before material testing.

5.2.3 Sample Preparation

Both the human pathological and healthy animal tissues underwent the same process to prepare samples for mechanical testing. The aortic samples were cut along the axial direction to obtain flat rectangular tissue sheets, and the loose connective tissues were carefully removed from the adventitial side. From the healthy tissue, a total of 5 square samples (5x5mm2) were cut, whereas 2 square samples of the same size (5x5mm2) were cut from the human pathological tissue.

5.2.4 Uniaxial Testing

Mechanical characterization of the aortic tissue was performed on a previously developed OCT experimental setup [175], which was adapted for short biological samples. The setup is presented in Figure 40. Specifically, the grips were substituted with L-shaped 3D printed arms anchored onto the device. We assumed that the force measured with a load cell in the arm was entirely transmitted through all parts of the system (arms, glue, sample) and that it induced uniform stress in the arterial sample regardless of the effects of stiffness of all other components of the system.

Samples were glued to a 3D printed arm using cyanoacrylate glue, with sandpaper placed between the arm and the sample. The arm was then mounted on the device with the transverse section of the sample perpendicular to the OCT camera; glue was placed on the other arm and a compression force of 0.5 N was gently applied for 10 min to allow adhesive curing. After the gluing process, the sample was rehydrated by filling the testing chamber with 0.9% physiological saline solution at room temperature. Due to the gentle compression, the tests always started with a negative offset in the force values, which was eventually removed for the analysis. Figures 41 and 42 show a schematic of the tested samples with the 3 vectors of the cartesian reference frame and a picture of the sample before and after rupture.

During each test, we decided to manually apply in each direction twelve displacement steps of 0.01 mm± uncertainty as this corresponds to an average strain of 0.005 (0.5%). Indeed, samples were collected from the same area and had an average thickness of 2 mm.

Steps were applied acting on the micrometric linear stages Newport M-460P-X shown in Figure 40, while continuously acquiring the corresponding load values with a load cell of 22 N capacity (rate output ±1.57 mV/V) with an accuracy of about 0.1 N, conditioned with a Futek IPM650 panel mount display (input range up to ±500 mV/V). After the last step, the sample was stretched up to rupture dynamically applying a strain rate of 0.1 s−1 to verify that the failure did not occur in the bond where the sample was glued to the arm (Figure 42); this quite large rate was due to technical constraint but it did not affect the main results of the study. Between each displacement step, there was a time window of about 30s requested to acquire the images with the OCT system.
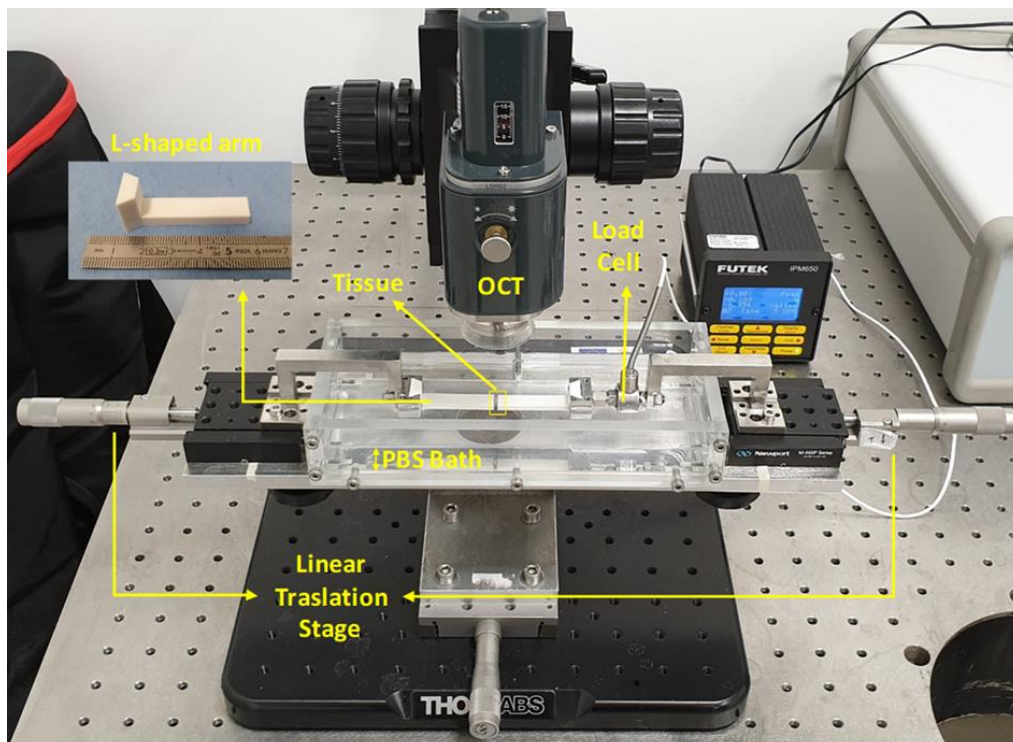
Figure 40 - Experimental setup used for radial tensile test.
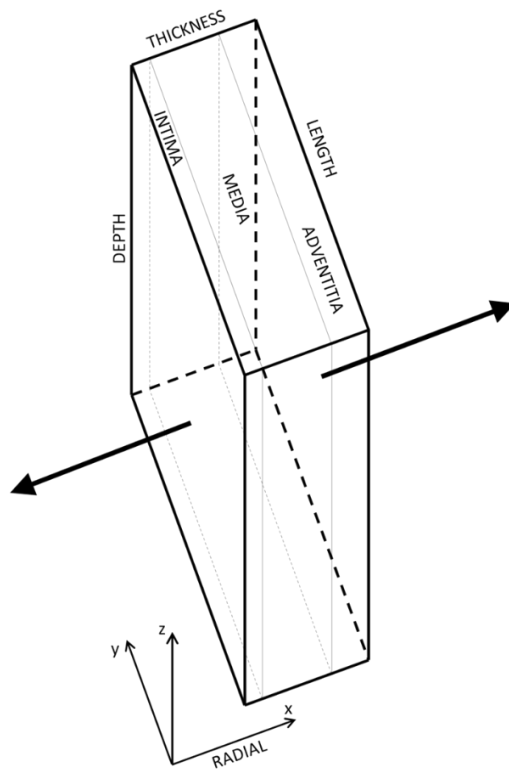
Figure 41 - Reference frame of the radial tensile test.
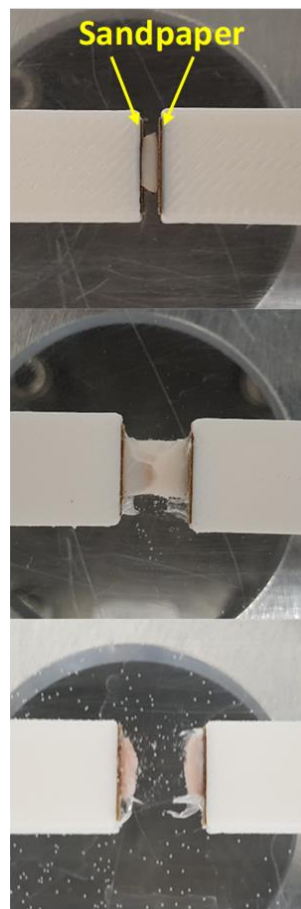
Figure 42 - Representative photographs of the initial, failure, and final stage of a successful radial tensile test.

5.2.5 Data Analysis

From force values obtained by the load cell for porcine samples, the stress was calculated. The stress-strain data were fitted by polynomial functions using SigmaPlot (Systat Software Inc., San Jose, California). These functions were used to interpolate the stress values within the experimental displacement range. Stress-strain curves were plotted considering the engineering stress values σ_{xx}, which were calculated by dividing the measured force value by the initial cross-sectional area of the sample (5×5 mm2), and the average Green-Lagrange strain across the sample.

Tissue stiffness defined as the first derivative of the stress-strain response at a given point was evaluated for porcine samples. Since all samples had the same thickness, we evaluated the stiffness at a displacement value of 0.04 mm, corresponding to an average strain of 0.01 (1%) (considering the strain values obtained by DIC), starting from the first positive stress point of the curve.

5.2.6 OCT–Acquisition System

For 3D volume image acquisition, the aortic wall reflectivity was measured with an OCT system (Thorlabs OCTTEL220C1) [163]. System settings were as follows: a center wavelength of 1300 nm, lateral resolution 7 μm, focal length 18 mm, maximum sensitivity range 111 dB (at 5.5 kHz), imaging depth 2.6 mm (in water), axial resolution 4.2 μm in water, and 5.5 μm in air. We found that PBS does not have different refractive properties compared to water, which has a reported refractive index of 1.33. Optimal OCT parameters were taken from a previous study by Santamaria et al. [175]: 5 μm pixel size, 2x2mm field of view (FOV). A volume of 2×2×1 mm3 was acquired, but the signal was obtained only up to a depth of 0.5 mm due to the scattering effects. During experiments, the OCT illumination tube was immersed in the PBS bath. The OCT x-y plane acquisition data were saved in TIFF stack format. The TIFF virtual stack was processed using ImageJ® software. Maximum intensity projection (MIP) [176] was applied on the stack to obtain a single representative 2D image for each step of the test. The contrast was enhanced by equalizing the histogram and the final images were exported as TIFF files for the displacement and strain measurements, final result is shown in Figure 43.
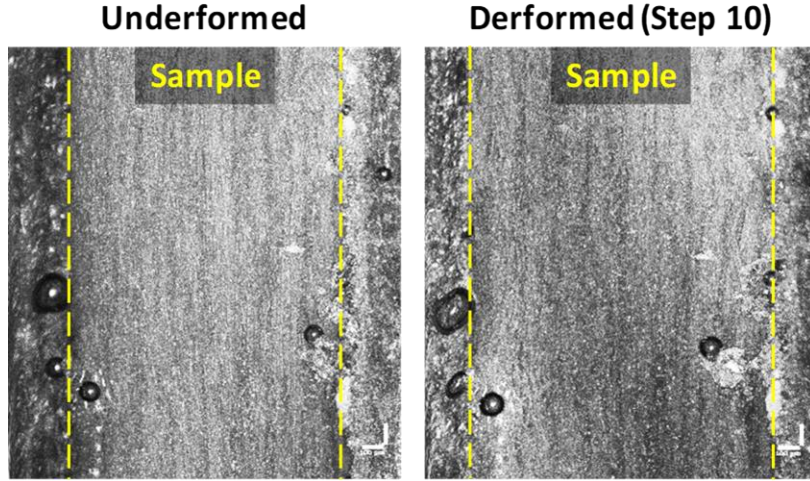
Figure 43 - Images used for DIC analysis of an undeformed and deformed porcine sample.

5.2.7 Digital Image Correlation

DIC is based on the analysis of the evolution in the greyscale distribution of the images obtained at different stages of the mechanical test. In this work, the subset-based DIC algorithm implemented in Ncorr [177] was used to obtain the in-plane displacement and strain fields over a region of interest (ROI) of about 1.5×1.5 mm^2 at 200 pixels/magnification. The selected rectangular ROI was defined to include the whole thickness of the sample. The settings used for DIC analyses [178] are given in Table 6.

Table 6 - Settings used in the DIC analysis

DIC Settings	Value
Subset size [pixels]	30
Step size [pixels]	1
Strain window size [data points]	5
Interpolation	Biquintic B-spline
Shape function	First-order

The Exx component of the Green-Lagrangian strain tensor was finally evaluated in Ncorr according to:

$$E_{xx} = \frac{1}{2}\left[2\frac{\partial u}{\partial x} + \left(\frac{\partial u}{\partial x}\right)^2 + \left(\frac{\partial v}{\partial x}\right)^2\right]$$

(66)

5.3 Results

Figure 44 shows experimental raw and fitted data obtained by mechanical testing of all the healthy porcine samples. In the curves of Figures 44(a) and (c), we report the points at which images were acquired for evaluating displacement (along the x direction) and strain (Exx component) fields as shown in Figures 45 and 46. For porcine samples, stress-strain curves were almost linear (up to the dotted lines in Figures 44 (b)-(d)-(f)-(h)-(j)) for the first steps. This was followed by a plateau region. Raw data show a stress peak at every step followed by a drop and a small valley.
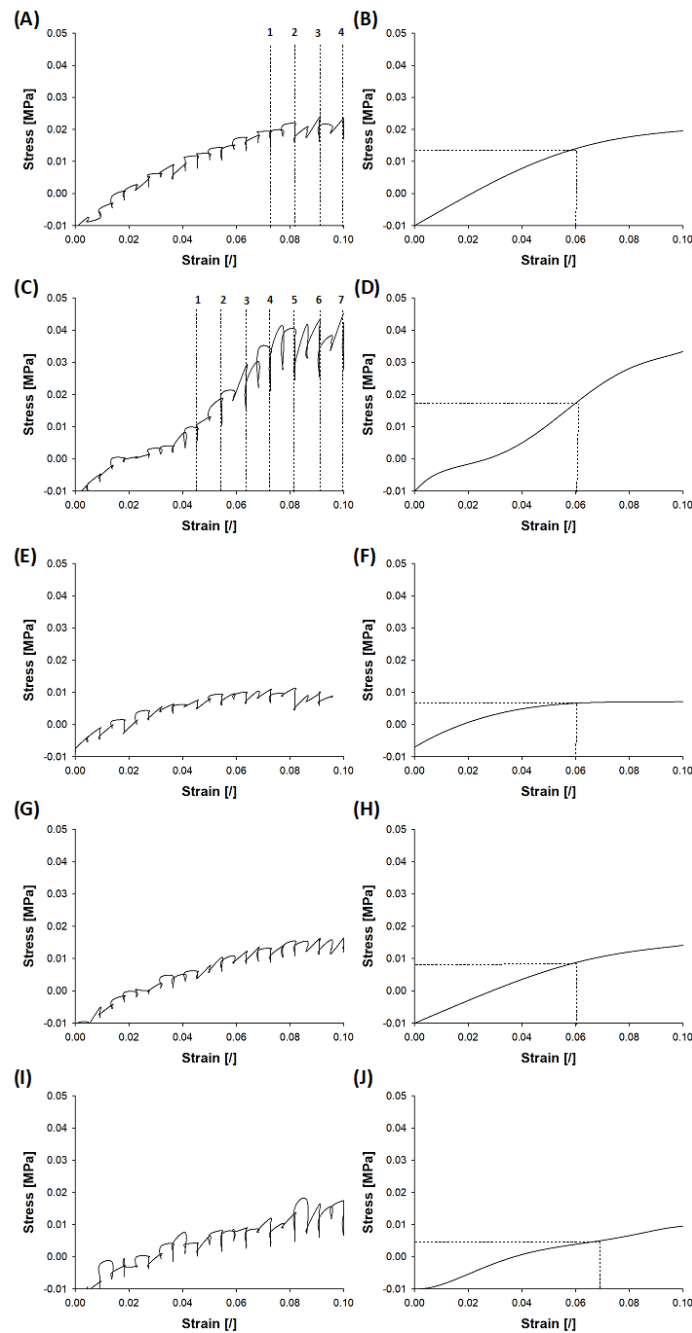
Figure 44 - Raw and fitted stress-strain data from porcine samples showing: points of raw curves corresponding to the images used for DIC and the linear part of fitted curves used for stiffness evaluation.

This behavior shows a moderate relaxation phenomenon that may be induced by chemoelastic effects in the arterial tissue as observed by [175]. Figures 45 and 46 show displacement and strain fields obtained by DIC on two porcine samples. These samples showed a strain localization with two different distributions of strain field. The sample shown in Figure 45 presented a single localization of strain on a wide deformed area covering almost the whole thickness of the sample, whereas the one shown in Figure 45 presented a narrow deformed area not covering the whole tissue thickness and with two parallel peaks in the center of the analyzed sample.
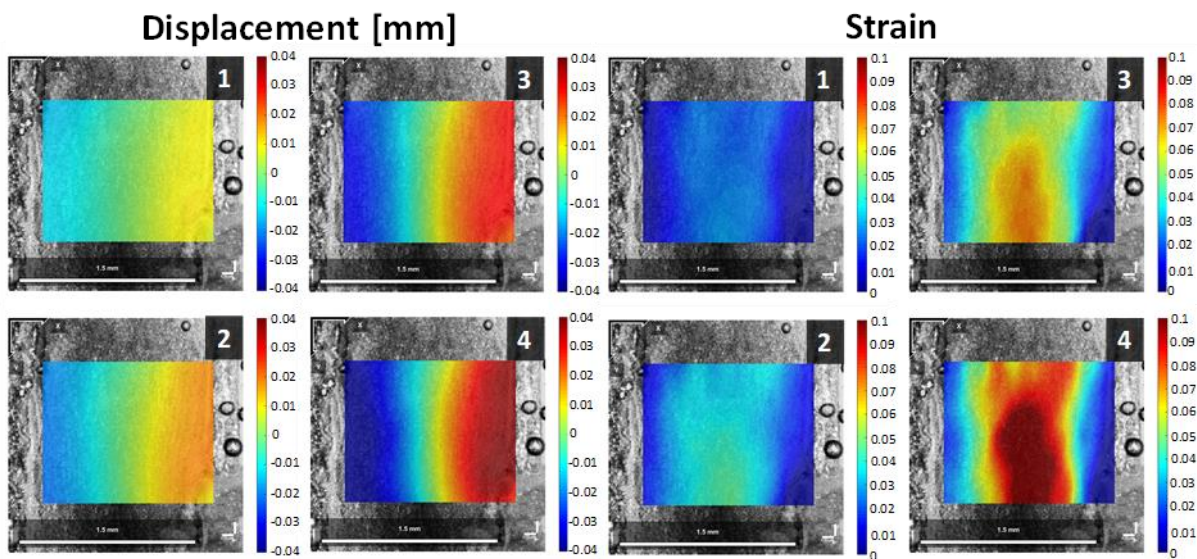
Figure 45 - Displacement (along the x direction) and strain fields (E_{xx} component) obtained by DIC on porcine sample n°1; in this particular case, the damage of the sample already reached a high value earlier after the 4th step and the strains and distortions were too high in further steps, inducing failure of the DIC.
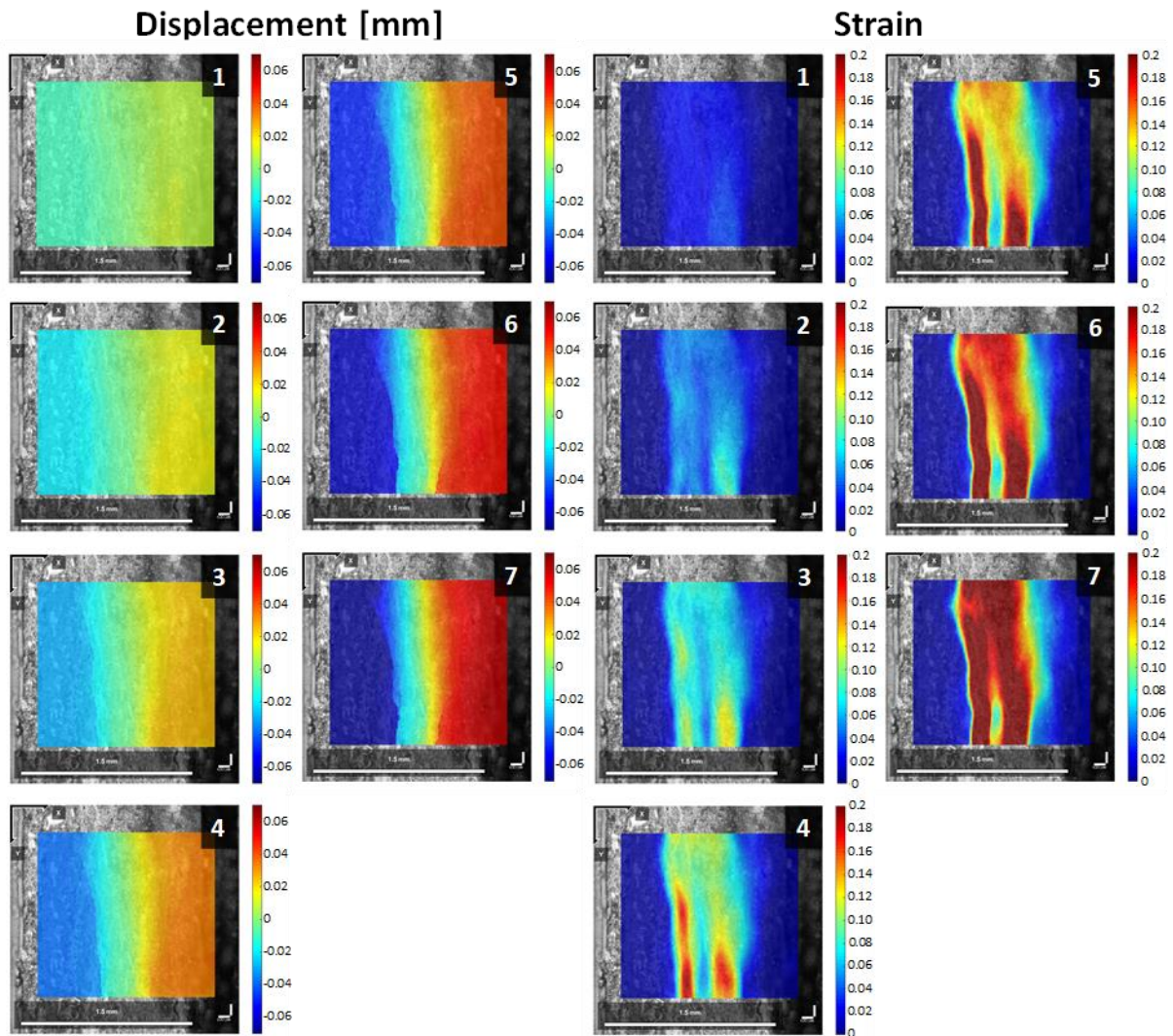
Figure 46 - Displacement (along the x direction) and strain fields (E_{xx} component) obtained by DIC on porcine sample n°2

It is interesting to notice that some samples ruptured in two steps (two parallel cracks, one occurring earlier than the other), showing stress-strain curves like the one in Figures 45(c)-(d). Indeed, it can be observed in Figure 46 that there are 2 bands of localized strain for this sample, each one leading to a crack. Figures 47 and 48 show displacement and strain fields obtained on two human aneurysmal samples. These two samples exhibited similar patterns of displacement and strain fields: the displacement fields show a discontinuity located into the intimal side of the sample shown in Figure 47 and in the middle of the sample shown in Figure 48. At these locations, the strain fields show peaks extending over a very narrow single area, showing a pronounced localization.
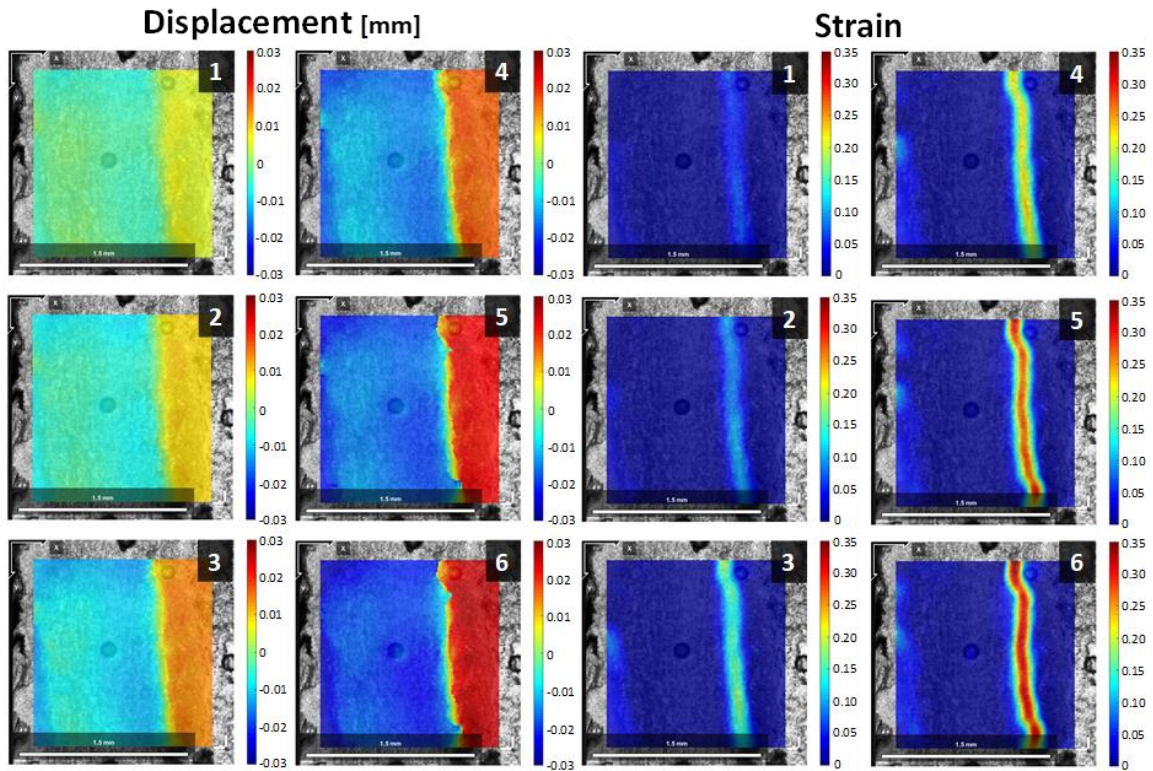
Figure 47 - Displacement (along the x direction) and strain fields (E_xx component) obtained by DIC on human sample n°1.
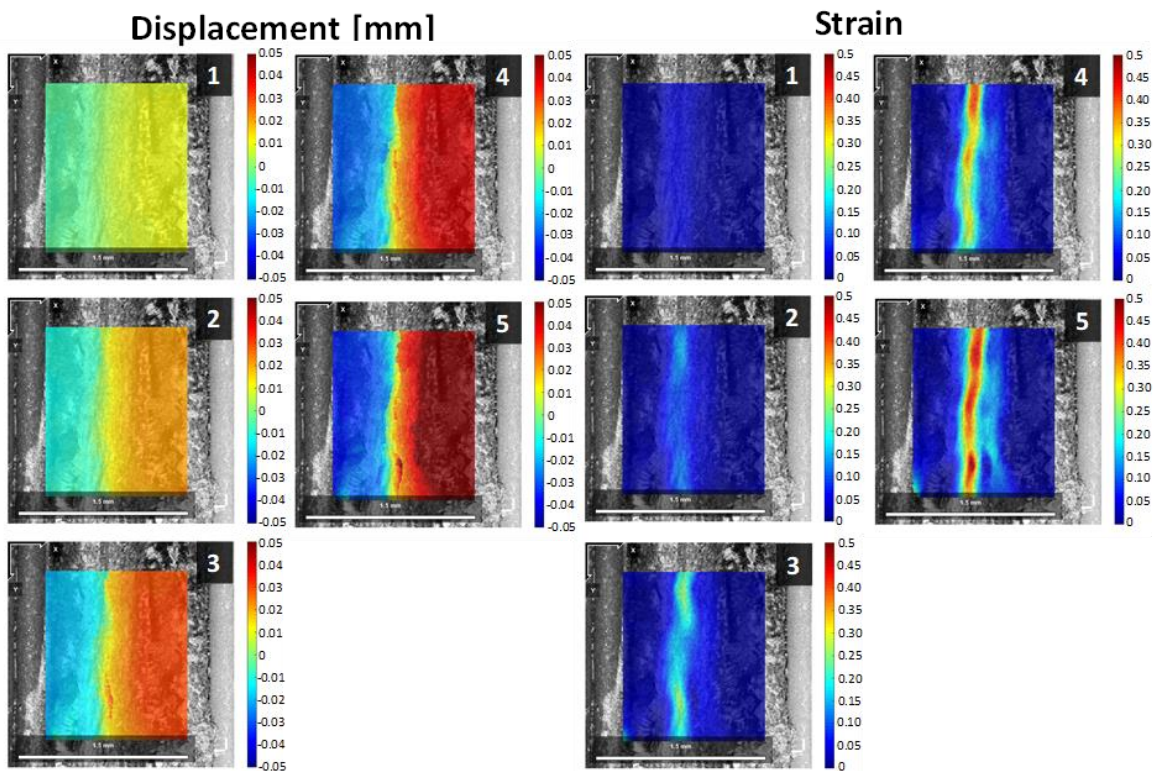
Figure 48 - Displacement (along the x direction) and strain fields (E_xx component) obtained by DIC on human sample n°2.

Average strains measured by DIC during the elastic range and the related stiffness values are reported in Table 7.

Sample	Displacement applied [mm]	Average strain measured by DIC [/]	Stiffness [kPa]
#1	0.04	0.009	475
#2	0.04	0.011	288
#3	0.04	0.006	864
#4	0.04	0.011	812
#5	0.04	0.013	358
	0.04±0	0.01±0.003	559±264

Table 7 - Radial stiffness values evaluated for porcine samples

5.4 Discussion

Aortic samples subjected to radial tension exhibited only a limited elastic response (strains<0.05), followed by sharp strain localization during the softening response, and eventually crack initiation. Unlike the elastic response in the circumferential direction which is known to be highly nonlinear due to increased collagen recruitment [139], the elastic response in the radial direction is nearly linear given the very narrow elastic range. Nevertheless, the measured radial stiffness values (average: 559 ± 264 kPa) are similar to the circumferential incremental modulus reported for the same porcine aortic tissue, which was estimated to be averagely 700 kPa [155] and for the human aorta in the diastolic-to-systolic range which was estimated to be approximately 500 kPa [179]. Several studies investigated dissection properties of the aortic wall using different mechanical tests such as peeling test [88, 153], in-plane shear test [151, 154], and radial tensile test [152, 153]. Mechanical tests were also accompanied by histological [152, 153] or microscopic imaging investigations [88, 154].

Although these studies have well established the strength values of the aortic wall when subjected to dissection loading, the mechanisms of rupture initiation and propagation were not addressed. Here we measured displacement and strain fields during the early stage of failure to better understand the mechanism underlying AD. The use of DIC, which requires a speckle pattern on the area of interest, was possible after overcoming several technical issues related to the dimension of the analyzed surface. The solution was provided by combining OCT with DIC to obtain displacements and strains. OCT does not require to generate a speckle pattern in the tissue sample surface, as the optical signature of the sample creates the pattern. This is due to the ability of OCT to differentiate the composition and structure of soft tissues as the reflectivity of the tissue creates a speckle to be

correlated by a correlation algorithm [180]. However, noise effects can easily corrupt the correlation for large deformations, but this was avoided by cautiously applying sequentially small loading steps during loading.

From OCT data, it is technically feasible to evaluate the strain field of the whole volume imaged using digital volume correlation (DVC). We preferred DIC given the limited penetration depth of OCT (less than 500 μm) leading to imaging of only 25% of the tissue depth. This is not enough to fully describe the mechanical behavior of aortic tissue when subjected to radial tension. Moreover, the contrast and brightness of OCT images decrease with imaging depth, which may also result in a decreasing correlation efficiency as a function of depth. This can be avoided by tissue clearing to increase the OCT imaging contrast and depth capability, but clearing can alter the biomechanical response of the aortic wall. In this way, we decided to apply maximum intensity projection on the stack of images before correlating them with the DIC algorithm.

According to DIC analysis, both healthy and pathological tissues exhibited a very early strain localization. The development of rupture in healthy aortic porcine samples was characterized by a concentration of strain localized on one or two sections of the tissue. In contrast, TAA tissue samples exhibited a sharper concentration of strain localized in a very narrow area of the aortic tissue. This difference could be explained by the biomechanical weakening of the aortic wall associated with aortic dilation, but we are performing tests on more TAA samples to verify if there is always an aneurysmal effect on the radial tension response. Indeed, collagen fibers are the main load-bearing structures in the arterial wall at large deformation while elastin bears most of the stress at small deformation. For aneurysmal tissues, the contribution of the elastin network is very small, because elastin is usually fractured in such diseased tissues [181]. This different resistance to aortic dissection of aneurysmal aorta compared to non-aneurysmal one was previously reported by Pasta et al. [88] using peeling tests.

The stress-strain curves obtained in this study for healthy porcine samples revealed an almost linear elastic behavior characterized by small strain levels. Indeed, the elastic range in the radial direction is narrow with a peak strain of 0.05, approximately. For the human aorta, tissue samples can be easily stretched upon 0.4 strain in circumferential and longitudinal directions under uniaxial tensile testing conditions. This narrow elastic range in the radial direction was previously observed by Sommer et al. [153] using a similar experimental test modality. The linear elastic part is followed by a plateau (indicating the initiation and propagation of the dissection), suggesting that the dissection may not begin and propagate at a steady rate but more in a discontinuous fashion, arresting and eventually reinitiating at regular intervals as observed in previous studies [88, 153, 182]. Vaishnav et al. [183]

showed that radial properties of canine aortic walls under compression loading conditions are different from those obtained in circumferential and longitudinal directions. In healthy human aortas, MacLean et al. [152] demonstrated that radial stresses are apparently compressive, but radial tensile forces may manifest to determine the onset of dissection under certain pathological conditions.

Repeating the same methodology on tissues with different pathologies could help to decipher the conditions leading to decrease dissection resistance in the aortic wall. Moreover, since early strain localization always precedes dissection, it is suggested that delaying this strain localization could increase the resistance to dissection. The localization phenomena could be investigated more thoroughly by finite element analyses in the future and a failure criterion could be calibrated against the radial tensile results presented in the current study.

5.5 Limitations

The analysis was performed on samples coming from one healthy porcine aorta and one pathological human aorta so that a larger number of experiments are necessary to confirm findings. Analysis of human samples was preliminary, the purpose of this study was to introduce the method, provide a proof of concept on porcine aortas and show the possibility of extracting results for human aortas.

Storage of tissues at $-24\ °C$ and the use of glue may alter the biomechanical properties of aortic tissue before testing and their effect on stress-strain curves should be quantified. Gluing duration of 10 min was chosen because it was the minimum time needed to effectively cure the glue without having dry effects on the sample. We did not observe any drying effects, but further investigation may be needed for clarification on this point. About 10 other samples failed in the glue during the test (cohesive rupture), and we discarded them for this study.

The limited penetration depth of OCT on aortic tissues prevented the acquisition of complete 3D images and consequently the analysis of the trough-the-thickness strain field. Given the relatively low spatial resolution of OCT images and the dimension of subset used in DIC analysis, it is possible that the separation between tissue portions would lead to an erroneous peak value of strain. Future work will adopt other DIC algorithms to deal with discontinuity in the displacement field [184]. Given the large deformation gradients, a second-order shape function could more appropriately describe the displacement field and allow obtaining more accurate results.

After each displacement step, the sample was no longer deformed for about 30 s to acquire the OCT images. Although there is some relaxation during this phase (force decrease), we assume there is no deformation in the sample itself (no creep) and then that the acquisition time will not affect the results. This assumption could be partially verified. Indeed, if the sample deformed during this phase, we

would observe spurious effects in the OCT images and strain maps related to the scanning process. Indeed, OCT scans the sample, raw after raw, starting from the top left and finishing at the bottom right. We never observed gradients related to this scanning process in the strain maps. However, we admit that the acquisition time should be reduced.

It was not possible to precondition the tissue because even a small strain could cause damage to the tissue. Previous studies achieving similar tests [153] did not report preconditioning either. Finally, we are aware that dissections are multifactorial and that radial tension is not the only factor that can explain dissection, but it is important to understand how arteries respond to radial tension to better understand how dissections can initiate.

Chapter VI

Non-linear Hereditariness of Aortic Tissues

In this chapter, an approach to non-linear hereditariness in terms of fractional-order calculus is used for the biomechanical characterization of aortic tissues. This study will continue, future investigations will focus on a statistical analysis of non-linear hereditariness parameters' differences among load values used for creep testing.

6.1 Background

Biological tissues under loads do not reproduce a perfect elastic behavior, neither a perfect viscous behavior, instead they reproduce a viscoelastic behavior [185-188]. This is not surprising since biological tissues are composed of liquids. In order to characterize the development and the failure of an aneurysm, it is important to study the viscoelastic behavior of these tissues. Two mechanical tests are used to analyze the viscoelastic behavior: creep test and stress-relaxation test. Creep test is a unidirectional test: the specimen is loaded linearly to a prescribed load value; once this value is reached up, it is kept constant for a time window, during which the specimen continues to stretch and, eventually, breaks off. In this study, the viscoelastic behavior, defined for more generality, material hereditariness, has been studied with respect to its effect on the failure of the aortic tissues. This subject is of great importance in understanding the phenomenon besides the initiation of the aneurysm in the thoracic ascending aortic tissue. The final aim of this study is to identify non-linear hereditariness material parameters in terms of fractional-order calculus of healthy aortic tissues.

6.1 Materials and Methods

6.2.1 Study population and specimen preparation

A total of 15 porcine aortic segments from animals without cardiovascular pathologies were collected by a local slaughterhouse within few hours by the death of the animal. Tissues were stored in a calcium-free and glucose-free 0.9% physiological saline solution at 4 °C and tested within 48 hours. Aortic tissues were prepared for mechanical testing by removing connective tissues. Samples were collected from the tissues in circumferential (CIRC) and longitudinal (LONG) directions using a dogbone sample cutting die, presented in Figure 49, to obtain perfectly identical samples (length=8mm, width=2mm). The thickness of each sample was measured using a caliber before material testing. The external sections of the sample were glued to sandpaper squares using cyanoacrylate to prevent slipping between clamps and the sample.
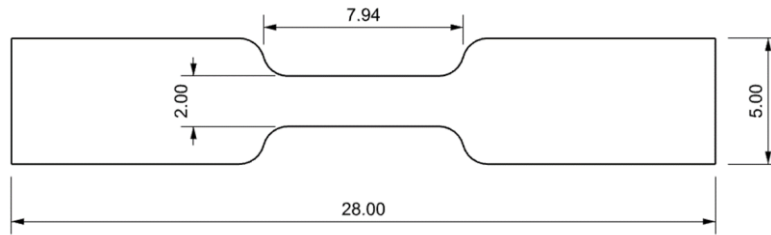
Figure 49 - Shape and size of dogbone sample cutting die (quotes in mm).

6.2.2 Tensile testing

Mechanical testing was performed using an ElectroForce TestBench system (TA Instrument, Boston, MA). In each test, the sample was submerged in a bath with 0.9% physiologic saline solution under controlled temperature of 37 °C while a small preload (0.3 N) was set prior to the testing protocol. Before each test, the sample underwent sinusoidal preconditioning of ten cycles at 8% of stretch for increasing test repeatability and reduce data variability. Creep testing requires precise load values for the samples to be tested. In order to analyze the relation between viscoelastic behavior and aortic tissues failure, the load values for creep testing were identified as percentages of the failure stress. It was requested to evaluate the average failure stress for these tissues in circumferential and longitudinal directions. Six tensile tests were performed in the two main directions (circumferential and longitudinal), the samples were stretched linearly with a displacement rate of 0.03 mm/s. The tensile test was considered over when the sample failed. Load values were collected by a 200N load cell. Data collected from tensile testing, presented in Fig. 50, were consistent with values provided in literature for healthy porcine tissues [189].
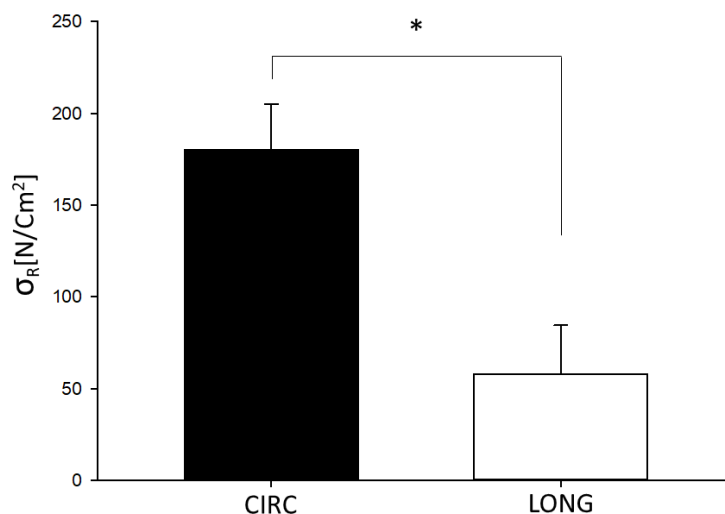
Figure 50 - Average failure stress values obtained by tensile testing in circumferential and longitudinal directions (p<0.05).

6.2.3 Creep testing

Once failure stress values were collected, creep testing was performed. In order to investigate the relation between viscoelastic behavior and aortic failure as the load reaches the ultimate value, the following stress values were identified: 50%-60%-70%-75%-80%-85%-90%-95% of failure stress. The sample underwent the same preconditioning used for tensile testing, then it was loaded up to the target value in about five seconds and the load was maintained for a time window of 30 minutes. Figure 51 presents the creep test protocol.
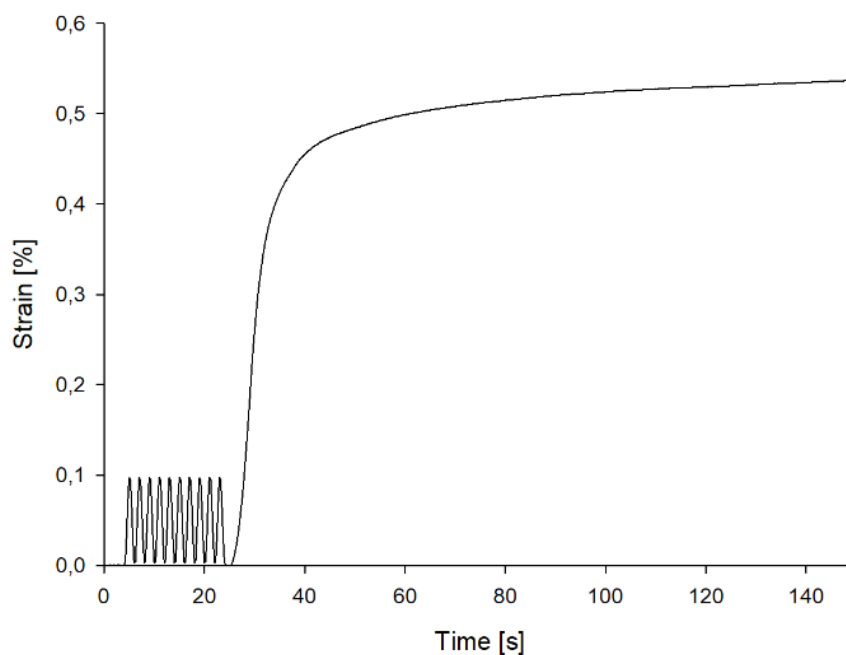
Figure 51 – Creep test protocol.

Each test could end in three different ways:

1. Early failure before reaching the target value;
2. Failure within the time window;
3. No failure at all.

Acquiring useful data from these tests is not easy, since inhomogeneity of aortic tissues and statistical variability of the test requires a high number of samples to be tested to deliver statistically significant results. Fifty-five samples were tested in total, a higher number of samples were tested at high stress levels (>80%) since the high instability of the sample due to the high level of stress maintained for a long time increased data variability. For more details about how many samples were tested for a specific direction or load value see Table 8.

Table 8 – Number of samples tested for each direction and failure stress level.

	50%	60%	70%	75%	80%	85%	90%	95%
CIRC	3	2	2	2	5	5	5	5
LONG	1	1	2	2	5	5	5	5
TOT	4	3	4	4	10	10	10	10

6.2.4 Data Analysis

The stress values were calculated by dividing the force values (measured by the load cell) by the initial cross-sectional area of the sample tested. The strain was evaluated as the difference between the initial and final length of the sample divided by the initial length, with no slippage between clamps and the sample considered. β values were obtained by power-law fitting of experimental campaigns for creep test using MATHEMATICA (Wolfram Research). The function used for fitting is:

$$J(t) = \frac{t^\beta}{C_\beta \Gamma[1+\beta]} \quad 0 < \beta < 1 \tag{67}$$

With β and C_β material parameters. Statistical analysis of average failure stress values delivered by tensile testing was performed using SimgmaPlot (Systat Software Inc.).

6.3 Results

Average failure stress values obtained by tensile testing along circumferential and longitudinal directions are reported in Figure 50. T-test showed, as expected, a statistical difference in strength ($P<0.001$) between samples aligned with circumferential and longitudinal directions. Characteristic creep curves obtained by mechanical testing are presented in Figure 52. These results highlighted the variability of strain values delivered for samples collected by different tissues tested along the same direction and at the same stress level; moreover, these results showed differences between samples tested in different directions within the same failure stress percentage group (for instance samples tested in CIRC and LONG directions at 80% of σ_R, as presented in Figure 52).
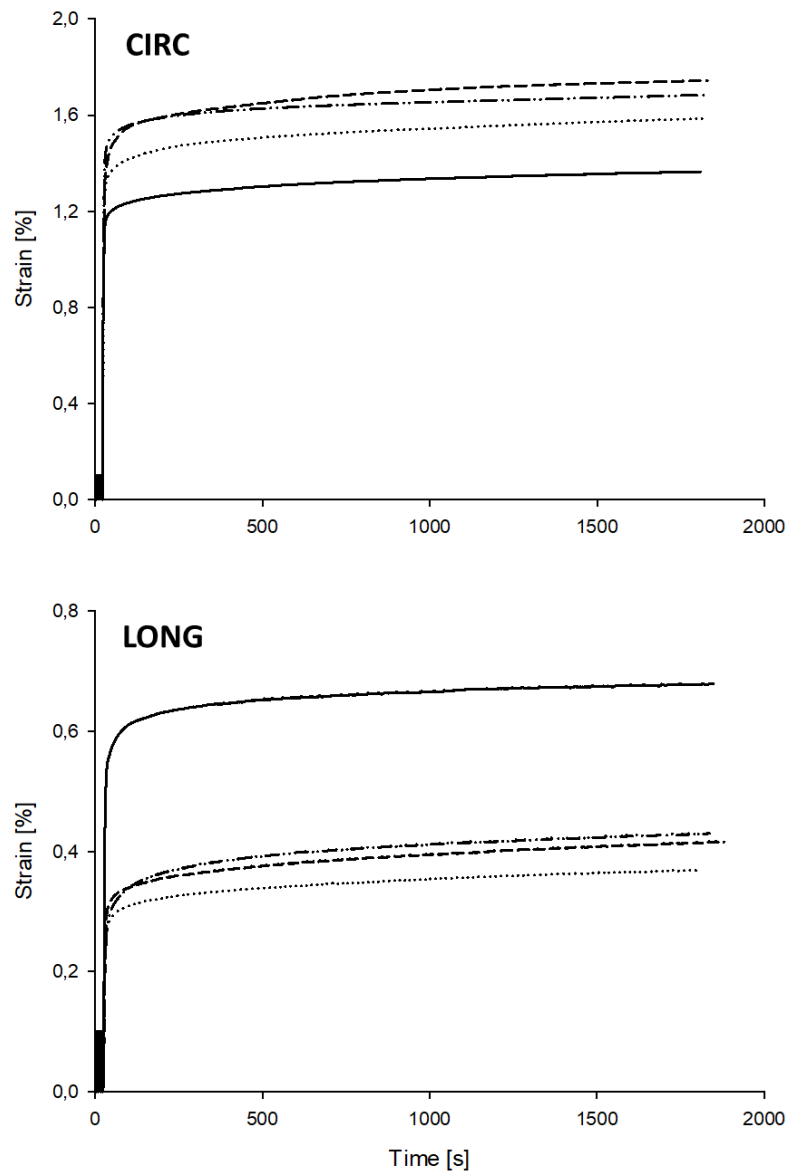
Figure 52 – Creep curves obtained for samples tested at 80% σ_R in circumferential and longitudinal directions.

Average β values obtained by best fitting of strain-time curves delivered by data creep testing for each stress level along circumferential and longitudinal directions are reported as histograms in Figure 53 and as a table in Table 9.

Table 9 – Average β values obtained by creep testing for each stress level in CIRC and LONG directions.

	50%	60%	70%	75%	80%	85%	90%	95%
CIRC								
AVG	0.02855	0.03135	0.04119	0.05326	0.03827	0.03776	0.03782	0.03680
DEV.ST.	0.00151	0.00040	0.00744	0.00486	0.00763	0.00495	0.00635	0.00311
LONG								
AVG	0.04236	0.03561	0.04457	0.05166	0.06410	0.06422	0.05074	0.05291
DEV.ST.	0.00000	0.00000	0.00142	0.00485	0.01608	0.02895	0.00517	0.00449
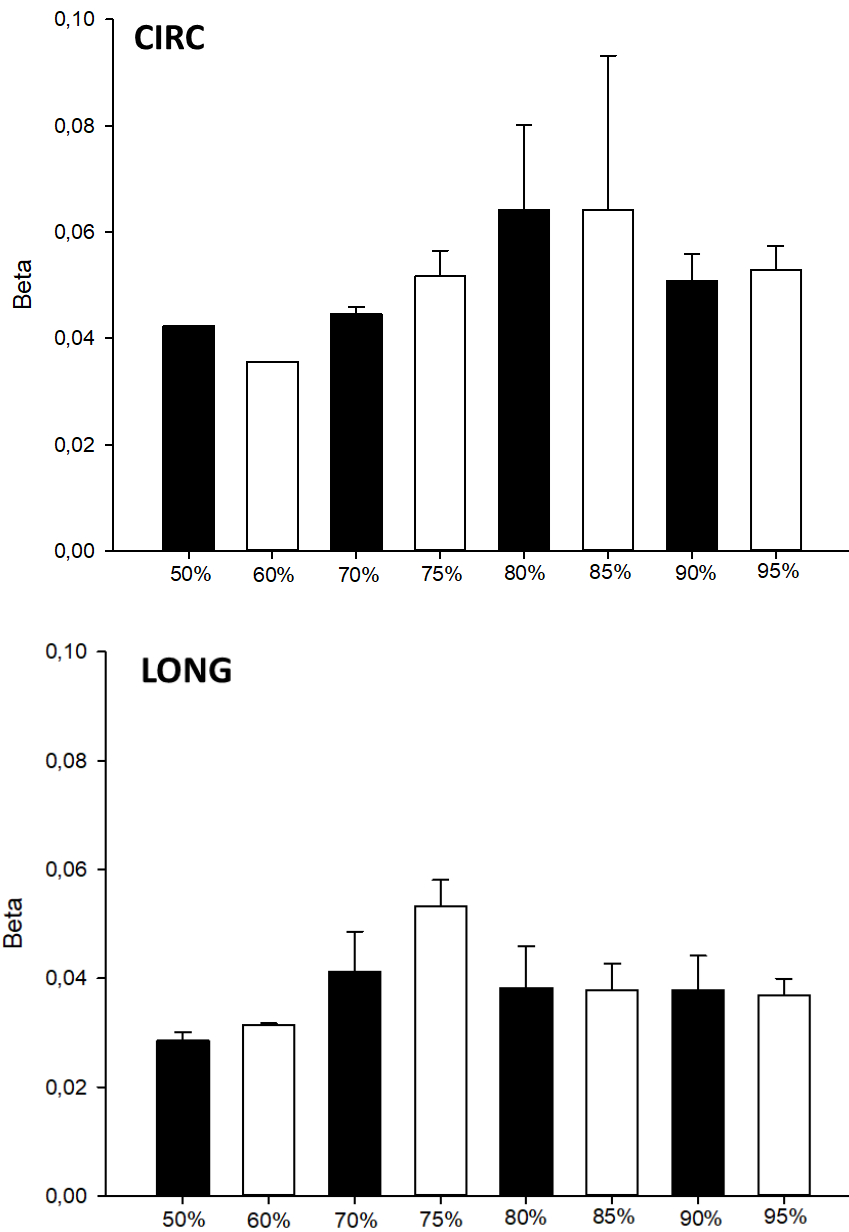
Figure 53 - Average β values obtained by creep testing for each stress level in CIRC and LONG directions.

6.4 Future Works

This project will be continued performing statistical analysis to measure differences of creep parameter β among different load levels and between directions of loading. Moreover, future analysis will include C_β, the other material parameter involved in the creep function considered. If needed, more experimental tests will be performed.

Conclusion

This PhD project focuses on the analysis of the micromechanical processes responsible for aortic failure and dissection through experimental (biaxial, radial tensile test) and computational (LESI methodology) mechanical characterization on pathological tissues coupled with advanced imaging techniques (multiphoton microscopy, optical coherence tomography).

Tissue stiffness determined from stress-strain curves under equibiaxial loading was heterogeneous among aortic quadrants in ATAAs, with the aortic major curvature quadrant in BAV patients weaker (1) than the anterior quadrant in BAVs and (2) than the major curvature quadrant in TAV patients. These observations were supported by qualitative multiphoton analysis carried out on the same tissues used for mechanical testing.

The material parameters for the Fung-type constitutive model obtained by equibiaxial mechanical testing are crucial for reliable stress predictions and for the development of risk stratification strategies not based on aortic size.

The patterns of extensional stiffness from in vivo imaging of ATAAs were evaluated on a cohort of 30 patients using the LESI methodology. No appreciable differences between BAV and TAV patients were found. Regional differences appeared marginal due to inter-individual variability. The correlation of patients' age with the extensional stiffness strongly depended on the valve phenotype. A strong relationship of the extensional stiffness with the pulsed pressure was found, supported by biomechanical explanations.

Finally, a new methodology to evaluate strain fields during dissection tests by combining OCT imaging with DIC was developed. This methodology was applied to radial tensile tests carried out on healthy and pathological aortic tissues. All aortic tissues showed an early localization of strain, with the healthy animal aortic tissue showing strain localized on one or two sections and the pathological human aortic tissue having a single sharper strain localization. This different mechanical behavior may be an expression of a weakened aortic wall in TAA

The limitations of this project are here summarized. Mechanical properties were not investigated for non-aneurysmal human aorta because of difficulties in collecting healthy aortic tissues from organ donors or heart transplant recipients. Larger BAV patients groups would have been appreciated to confirm observations delivered by experimental and numerical analyses. Tissue stress levels were estimated considering the local equilibrium between pressures and tensions in a membrane, indicating that the aortic wall experience no shear through the thickness. This may not be a realistic assumption

in regions near the aortic branches but these were excluded from the analyses. Cryopreservation of tissues may alter the biomechanical properties of aortic tissue before testing and its effect should be quantified. The biaxial mechanical protocol was extended to an equibiaxial loading condition whereas the full anisotropic behavior of the aorta can be captured varying the stress ratio in material stretching directions. The peripheral pulse pressure rather than central aortic pressure was used as clinical data for statistical analyses. Patient-specific numerical methods were applied on only one imaging modality: computed tomography.

Future directions of this project will be focused on: 1) extracting quantitative data by multiphoton analysis to assess structural heterogeneity of ATAA; 2) validating in-silico modeling and extending the numerical methodology to other imaging modalities (ultrasounds, MRI); 3) applying experimental protocols developed for strain field evaluation onto a larger number of samples from patients with different cardiovascular pathological conditions; 4) investigating the strain localization of dissecting tissues by finite element analyses; 5) performing statistical analysis on data delivered by creep testing; 6) extending the viscoelastic analysis to stress-relaxation testing.

Bibliography

1.   Elefteriades, J.A. and E.A. Farkas, *Thoracic aortic aneurysm: clinically pertinent controversies and uncertainties.* Journal of the American College of Cardiology, 2010. **55**(9): p. 841-857.
2.   Pape, L., et al., *Aortic Diameter> 5.5 cm is not a good predictor of type A aortic dissection.* Circulation, 2007. **116**: p. 1120-1127.
3.   Duprey, A., et al., *Biaxial rupture properties of ascending thoracic aortic aneurysms.* Acta biomaterialia, 2016. **42**: p. 273-285.
4.   Farzaneh, S., O. Trabelsi, and S. Avril, *Inverse identification of local stiffness across ascending thoracic aortic aneurysms.* Biomechanics and modeling in mechanobiology, 2019. **18**(1): p. 137-153.
5.   Martin, C., et al., *Predictive biomechanical analysis of ascending aortic aneurysm rupture potential.* Acta biomaterialia, 2013. **9**(12): p. 9392-9400.
6.   Longobardo, L., et al., *Impairment of elastic properties of the aorta in bicuspid aortic valve: relationship between biomolecular and aortic strain patterns.* European Heart Journal-Cardiovascular Imaging, 2018. **19**(8): p. 879-887.
7.   Teixeira, R., et al., *Circumferential ascending aortic strain and aortic stenosis.* European Heart Journal–Cardiovascular Imaging, 2013. **14**(7): p. 631-641.
8.   Pasta, S., et al., *In vivo strain analysis of dilated ascending thoracic aorta by ECG-gated CT angiographic imaging.* Annals of biomedical engineering, 2017. **45**(12): p. 2911-2920.
9.   Selvin, E., et al., *A comprehensive histopathological evaluation of vascular medial fibrosis: insights into the pathophysiology of arterial stiffening.* Atherosclerosis, 2010. **208**(1): p. 69-74.
10.   Smoljkić, M., et al., *Biomechanical characterization of ascending aortic aneurysms.* Biomechanics and modeling in mechanobiology, 2017. **16**(2): p. 705-720.
11.   Khan, I.A. and C.K. Nair, *Clinical, diagnostic, and management perspectives of aortic dissection.* Chest, 2002. **122**(1): p. 311-328.
12.   Mikich, M., *Dissection of the aorta: a new approach.* Heart, 2003. **89**(1): p. 6-8.
13.   Buehler, M.J., *Nanomechanics of collagen fibrils under varying cross-link densities: atomistic and continuum studies.* Journal of the mechanical behavior of biomedical materials, 2008. **1**(1): p. 59-67.
14.   Wu, D., et al., *Molecular mechanisms of thoracic aortic dissection.* Journal of Surgical Research, 2013. **184**(2): p. 907-924.
15.   Gupta, G., *Animal lectins: form, function and clinical applications*. 2012: Springer Science & Business Media.
16.   Tadros, T.M., M.D. Klein, and O.M. Shapira, *Ascending aortic dilatation associated with bicuspid aortic valve: pathophysiology, molecular biology, and clinical implications.* Circulation, 2009. **119**(6): p. 880-890.
17.   Holzapfel, G.A., T.C. Gasser, and R.W. Ogden, *A new constitutive framework for arterial wall mechanics and a comparative study of material models.* Journal of elasticity and the physical science of solids, 2000. **61**(1): p. 1-48.
18.   Elefteriades, J.A., et al., *Guilt by association: paradigm for detecting a silent killer (thoracic aortic aneurysm).* Open Heart, 2015. **2**(1).
19.   Schaefer, B.M., et al., *The bicuspid aortic valve: an integrated phenotypic classification of leaflet morphology and aortic root shape.* Heart, 2008. **94**(12): p. 1634-1638.
20.   Verma, S. and S.C. Siu, *Aortic dilatation in patients with bicuspid aortic valve.* New England Journal of Medicine, 2014. **370**(20): p. 1920-1929.
21.   Benjamin, E.J., et al., *Heart disease and stroke statistics—2019 update: a report from the American Heart Association.* Circulation, 2019. **139**(10): p. e56-e528.
22.   Holzapfel, G.A., *Structural and numerical models for the (visco) elastic response of arterial walls with residual stresses*, in *Biomechanics of soft tissue in cardiovascular systems*. 2003, Springer. p. 109-184.
23.   Nimni, M.E., *Collagen: Volume I: Biochemistry*. 2018: CRC press.

24.   Bernard, Y., et al., *False lumen patency as a predictor of late outcome in aortic dissection.* The American journal of cardiology, 2001. **87**(12): p. 1378-1382.
25.   Holzapfel, A.G., *Nonlinear solid mechanics* 2000.
26.   Humphrey, J.D., *Continuum biomechanics of soft biological tissues.* Proceedings of the Royal Society of London. Series A: Mathematical, Physical and Engineering Sciences, 2003. **459**(2029): p. 3-46.
27.   Holzapfel, G.A., *Biomechanics of soft tissue.* The handbook of materials behavior models, 2001. **3**: p. 1049-1063.
28.   Iozzo, R.V. and L. Schaefer, *Proteoglycan form and function: a comprehensive nomenclature of proteoglycans.* Matrix biology, 2015. **42**: p. 11-55.
29.   Wight, T.N., M.G. Kinsella, and E.E. Qwarnström, *The role of proteoglycans in cell adhesion, migration and proliferation.* Current opinion in cell biology, 1992. **4**(5): p. 793-801.
30.   Conti, C.A., et al., *Biomechanical implications of the congenital bicuspid aortic valve: a finite element study of aortic root function from in vivo data.* The Journal of thoracic and cardiovascular surgery, 2010. **140**(4): p. 890-896. e2.
31.   Walsh, R., *Hurst's the heart manual of cardiology*. 2012: McGraw-Hill Education.
32.   Schulze-Bauer, C.A., P. Regitnig, and G.A. Holzapfel, *Mechanics of the human femoral adventitia including the high-pressure response.* American Journal of Physiology-Heart and Circulatory Physiology, 2002. **282**(6): p. H2427-H2440.
33.   Gao, F., et al., *Fluid-structure interaction within a layered aortic arch model.* Journal of biological physics, 2006. **32**(5): p. 435-454.
34.   Litmanovich, D., et al., *CT and MRI in diseases of the aorta.* American Journal of Roentgenology, 2009. **193**(4): p. 928-940.
35.   Joyce, J.W., et al., *Aneurysms of the thoracic aorta: a clinical study with special reference to prognosis.* Circulation, 1964. **29**(2): p. 176-181.
36.   Coady, M.A., et al., *What is the appropriate size criterion for resection of thoracic aortic aneurysms?* The Journal of thoracic and cardiovascular surgery, 1997. **113**(3): p. 476-491.
37.   Elefteriades, J.A., *Thoracic aortic aneurysm: reading the enemy's playbook.* Current problems in cardiology, 2008. **33**(5): p. 203-277.
38.   Della Corte, A., et al., *The ascending aorta with bicuspid aortic valve: a phenotypic classification with potential prognostic significance.* European Journal of Cardio-Thoracic Surgery, 2014. **46**(2): p. 240-247.
39.   Roy, C.S., *The elastic properties of the arterial wall.* The Journal of physiology, 1881. **3**(2): p. 125-159.
40.   Bergel, D., *The visco-elastic properties of the arterial wall. 1960*. 1960, Ph. D.: 250.
41.   Saini, A., C. Berry, and S. Greenwald, *Effect of age and sex on residual stress in the aorta.* Journal of vascular research, 1995. **32**(6): p. 398-405.
42.   Lakes, R. and R. Vanderby, *Interrelation of creep and relaxation: a modeling approach for ligaments.* 1999.
43.   Chuong, C.-J. and Y.-C. Fung, *Residual stress in arteries*, in *Frontiers in biomechanics*. 1986, Springer. p. 117-129.
44.   Matsumoto, T., T. Goto, and M. Sato, *Microscopic residual stress caused by the mechanical heterogeneity in the lamellar unit of the porcine thoracic aortic wall.* JSME International Journal Series A Solid Mechanics and Material Engineering, 2004. **47**(3): p. 341-348.
45.   Fung, Y. and J. Sanders, *A first course in continuum mechanics.* Journal of Applied Mechanics, 1978. **45**(4): p. 969.
46.   Minns, R., P. Soden, and D. Jackson, *The role of the fibrous components and ground substance in the mechanical properties of biological tissues: a preliminary investigation.* Journal of biomechanics, 1973. **6**(2): p. 153-165.
47.   Fung, Y.-c., *Biomechanics: mechanical properties of living tissues*. 2013: Springer Science & Business Media.
48.   Cowin, S.C. and S.B. Doty, *Tissue mechanics*. 2007: Springer Science & Business Media.
49.   Ogden, R.W., *Non-linear elastic deformations*. 1997: Courier Corporation.
50.   Belytschko, T., et al., *Nonlinear finite elements for continua and structures*. 2013: John wiley & sons.

51.	Greenwald, S., et al., *Experimental investigation of the distribution of residual strains in the artery wall.* 1997.

52.	Holzapfel, G.A., et al., *Layer-specific 3D residual deformations of human aortas with non-atherosclerotic intimal thickening.* Annals of biomedical engineering, 2007. **35**(4): p. 530-545.

53.	Liu, S. and Y. Fung, *Zero-stress states of arteries.* Journal of biomechanical engineering, 1988. **110**(1): p. 82-84.

54.	Chen, H., et al., *Biaxial deformation of collagen and elastin fibers in coronary adventitia.* Journal of applied physiology, 2013. **115**(11): p. 1683-1693.

55.	Takamizawa, K. and K. Hayashi, *Strain energy density function and uniform strain hypothesis for arterial mechanics.* Journal of biomechanics, 1987. **20**(1): p. 7-17.

56.	Helmchen, F. and W. Denk, *Deep tissue two-photon microscopy.* Nature methods, 2005. **2**(12): p. 932-940.

57.	Denk, W., J.H. Strickler, and W.W. Webb, *Two-photon laser scanning fluorescence microscopy.* Science, 1990. **248**(4951): p. 73-76.

58.	Diaspro, A. and M. Robello, *Two-photon excitation of fluorescence for three-dimensional optical imaging of biological structures.* Journal of Photochemistry and Photobiology B: Biology, 2000. **55**(1): p. 1-8.

59.	Masters, B.R. and P.T. So, *Multi-photon excitation microscopy and confocal microscopy imaging of in vivo human skin: a comparison.* Microscopy and Microanalysis, 1999. **5**(4): p. 282-289.

60.	Masters, B.R. and P.T. So, *Confocal microscopy and multi-photon excitation microscopy of human skin in vivo.* Optics express, 2001. **8**(1): p. 2-10.

61.	So, P.T., H. Kim, and I.E. Kochevar, *Two-photon deep tissue ex vivo imaging of mouse dermal and subcutaneous structures.* Optics express, 1998. **3**(9): p. 339-350.

62.	Squirrell, J.M., et al., *Long-term two-photon fluorescence imaging of mammalian embryos without compromising viability.* Nature biotechnology, 1999. **17**(8): p. 763-767.

63.	Gauderon, R., P. Lukins, and C. Sheppard, *Three-dimensional second-harmonic generation imaging with femtosecond laser pulses.* Optics letters, 1998. **23**(15): p. 1209-1211.

64.	Guo, Y., et al., *Second-harmonic tomography of tissues.* Optics Letters, 1997. **22**(17): p. 1323-1325.

65.	Campagnola, P.J., et al., *Second harmonic imaging microscopy of living cells.* Journal of biomedical optics, 2001. **6**(3): p. 277-286.

66.	Moreaux, L., O. Sandre, and J. Mertz, *Membrane imaging by second-harmonic generation microscopy.* JOSA B, 2000. **17**(10): p. 1685-1694.

67.	Zoumi, A., A. Yeh, and B.J. Tromberg, *Imaging cells and extracellular matrix in vivo by using second-harmonic generation and two-photon excited fluorescence.* Proceedings of the National Academy of Sciences, 2002. **99**(17): p. 11014-11019.

68.	Richards-Kortum, R. and E. Sevick-Muraca, *Quantitative optical spectroscopy for tissue diagnosis.* Annual review of physical chemistry, 1996. **47**(1): p. 555-606.

69.	Goeppert-Mayer, M., *Über Elementarakte mit zwei Quantensprüngen.* Annalen der Physik, 1931. **401**: p. 273-294.

70.	Zipfel, W.R., R.M. Williams, and W.W. Webb, *Nonlinear magic: multiphoton microscopy in the biosciences.* Nature biotechnology, 2003. **21**(11): p. 1369-1377.

71.	Deyl, Z., K. Macek, and M. Adam, *Studies on the chemical nature of elastin fluorescence.* Biochimica et Biophysica Acta (BBA)-Protein Structure, 1980. **625**(2): p. 248-254.

72.	Parasassi, T., et al., *Two-photon microscopy of aorta fibers shows proteolysis induced by LDL hydroperoxides.* Free Radical Biology and Medicine, 2000. **28**(11): p. 1589-1597.

73.	Megens, R., et al., *Two-photon microscopy of vital murine elastic and muscular arteries.* Journal of vascular research, 2007. **44**(2): p. 87-98.

74.	Bélisle, J., *Design and assembly of a multimodal nonlinear laser scanning microscope*. 2006, McGill University Montreal, Quebec, Canada.

75.	Williams, R.M., W.R. Zipfel, and W.W. Webb, *Interpreting second-harmonic generation images of collagen I fibrils.* Biophysical journal, 2005. **88**(2): p. 1377-1386.

76.	Failla, G., *Stationary response of beams and frames with fractional dampers through exact frequency response functions.* Journal of Engineering Mechanics, 2017. **143**(5): p. D4016004.

77.   Gurtin, M.E. and E. Sternberg, *Archive for Rational Mechanics and Analysis.* Springer, 1962.

78.   Amabili, M., et al., *Layer-specific hyperelastic and viscoelastic characterization of human descending thoracic aortas.* Journal of the mechanical behavior of biomedical materials, 2019. **99**: p. 27-46.

79.   Amabili, M., et al., *Viscoelastic characterization of woven Dacron for aortic grafts by using direction-dependent quasi-linear viscoelasticity.* Journal of the mechanical behavior of biomedical materials, 2018. **82**: p. 282-290.

80.   Coady, M.A., et al., *Natural history, pathogenesis and etiology of thoracic aortic aneurysms and dissections.* Cardiology Clinics, 1999. **17**(4): p. 615-635.

81.   Januzzi, J.L., et al., *Characterizing the young patient with aortic dissection: results from the international registry of aortic dissection (IRAD).* Journal of the American College of Cardiology, 2004. **43**(4): p. 665-669.

82.   Borger, M.A., et al., *The american association for thoracic surgery consensus guidelines on bicuspid aortic valve–related aortopathy: full online-only version.* The Journal of Thoracic and Cardiovascular Surgery, 2018. **156**(2): p. e41-e74.

83.   Pape, L.A., et al., *Aortic diameter >or = 5.5 cm is not a good predictor of type A aortic dissection: observations from the International Registry of Acute Aortic Dissection (IRAD).* Circulation, 2007. **116**(10): p. 1120-7.

84.   Martin, C., et al., *Age-dependent ascending aorta mechanics assessed through multiphase CT.* Annals of biomedical engineering, 2013. **41**(12): p. 2565-2574.

85.   Prakash, A., et al., *Segmental aortic stiffness in children and young adults with connective tissue disorders: relationships with age, aortic size, rate of dilation, and surgical root replacement.* Circulation, 2015. **132**(7): p. 595-602.

86.   Sulejmani, F., et al., *Biomechanical properties of the thoracic aorta in Marfan patients.* Annals of cardiothoracic surgery, 2017. **6**(6): p. 610.

87.   Raaz, U., et al., *Segmental aortic stiffening contributes to experimental abdominal aortic aneurysm development.* Circulation, 2015. **131**(20): p. 1783-1795.

88.   Pasta, S., et al., *Effect of aneurysm on the mechanical dissection properties of the human ascending thoracic aorta.* The Journal of thoracic and cardiovascular surgery, 2012. **143**(2): p. 460-467.

89.   Hope, M.D., et al., *4D flow CMR in assessment of valve-related ascending aortic disease.* JACC: Cardiovascular Imaging, 2011. **4**(7): p. 781-787.

90.   Hope, M.D., et al., *Bicuspid aortic valve: four-dimensional MR evaluation of ascending aortic systolic flow patterns.* Radiology, 2010. **255**(1): p. 53-61.

91.   Cotrufo, M., et al., *Different patterns of extracellular matrix protein expression in the convexity and the concavity of the dilated aorta with bicuspid aortic valve: preliminary results.* The Journal of thoracic and cardiovascular surgery, 2005. **130**(2): p. 504. e1-504. e9.

92.   Della Corte, A., et al., *Spatial patterns of matrix protein expression in dilated ascending aorta with aortic regurgitation: congenital bicuspid valve versus Marfan's syndrome.* J Heart Valve Dis, 2006. **15**(1): p. 20-7.

93.   Mohamed, S.A., et al., *Locally different endothelial nitric oxide synthase protein levels in ascending aortic aneurysms of bicuspid and tricuspid aortic valve.* Cardiology research and practice, 2012. **2012**.

94.   Albinsson, S., et al., *Patients with bicuspid and tricuspid aortic valve exhibit distinct regional microrna signatures in mildly dilated ascending aorta.* Heart and vessels, 2017. **32**(6): p. 750-767.

95.   Barker, A.J., C. Lanning, and R. Shandas, *Quantification of hemodynamic wall shear stress in patients with bicuspid aortic valve using phase-contrast MRI.* Annals of biomedical engineering, 2010. **38**(3): p. 788-800.

96.   Mahadevia, R., et al., *Bicuspid aortic cusp fusion morphology alters aortic three-dimensional outflow patterns, wall shear stress, and expression of aortopathy.* Circulation, 2014. **129**(6): p. 673-682.

97.   D'Ancona, G., et al., *Haemodynamic predictors of a penetrating atherosclerotic ulcer rupture using fluid–structure interaction analysis.* Interactive cardiovascular and thoracic surgery, 2013. **17**(3): p. 576-578.

98.   Lee, J.J., et al., *Role of computational modeling in thoracic aortic pathology: a review.* Journal of Cardiac Surgery: Including Mechanical and Biological Support for the Heart and Lungs, 2014. **29**(5): p. 653-662.

99.   Pasta, S., et al., *In silico shear and intramural stresses are linked to aortic valve morphology in dilated ascending aorta.* European Journal of Vascular and Endovascular Surgery, 2017. **54**(2): p. 254-263.

100.   Rinaudo, A. and S. Pasta, *Regional variation of wall shear stress in ascending thoracic aortic aneurysms.* Proceedings of the Institution of Mechanical Engineers, Part H: Journal of Engineering in Medicine, 2014. **228**(6): p. 627-638.

101.   Deveja, R.P., et al., *Effect of aneurysm and bicuspid aortic valve on layer-specific ascending aorta mechanics.* The Annals of thoracic surgery, 2018. **106**(6): p. 1692-1701.

102.   Tsamis, A., et al., *Fiber micro-architecture in the longitudinal-radial and circumferential-radial planes of ascending thoracic aortic aneurysm media.* Journal of biomechanics, 2013. **46**(16): p. 2787-2794.

103.   Tsamis, A., et al., *Extracellular matrix fiber microarchitecture is region-specific in bicuspid aortic valve-associated ascending aortopathy.* The Journal of thoracic and cardiovascular surgery, 2016. **151**(6): p. 1718-1728. e5.

104.   Iliopoulos, D.C., et al., *Regional and directional variations in the mechanical properties of ascending thoracic aortic aneurysms.* Medical engineering & physics, 2009. **31**(1): p. 1-9.

105.   Sokolis, D.P., E.P. Kritharis, and D.C. Iliopoulos, *Effect of layer heterogeneity on the biomechanical properties of ascending thoracic aortic aneurysms.* Medical & biological engineering & computing, 2012. **50**(12): p. 1227-1237.

106.   Gasser, T.C., R.W. Ogden, and G.A. Holzapfel, *Hyperelastic modelling of arterial layers with distributed collagen fibre orientations.* Journal of the royal society interface, 2006. **3**(6): p. 15-35.

107.   Holzapfel, G.A., et al., *Modelling non-symmetric collagen fibre dispersion in arterial walls.* Journal of the royal society interface, 2015. **12**(106): p. 20150188.

108.   Azadani, A.N., et al., *Biomechanical properties of human ascending thoracic aortic aneurysms.* The Annals of thoracic surgery, 2013. **96**(1): p. 50-58.

109.   Longobardo, L., et al., *Impairment of elastic properties of the aorta in bicuspid aortic valve: relationship between biomolecular and aortic strain patterns.* European Heart Journal - Cardiovascular Imaging, 2017. **19**(8): p. 879-887.

110.   Guala, A., et al., *Influence of aortic dilation on the regional aortic stiffness of bicuspid aortic valve assessed by 4-dimensional flow cardiac magnetic resonance: comparison with Marfan syndrome and degenerative aortic aneurysm.* JACC: Cardiovascular Imaging, 2019. **12**(6): p. 1020-1029.

111.   Mendez, V., M. Di Giuseppe, and S. Pasta, *Comparison of hemodynamic and structural indices of ascending thoracic aortic aneurysm as predicted by 2-way FSI, CFD rigid wall simulation and patient-specific displacement-based FEA.* Computers in biology and medicine, 2018. **100**: p. 221-229.

112.   Youssefi, P., et al., *Patient-specific computational fluid dynamics—assessment of aortic hemodynamics in a spectrum of aortic valve pathologies.* The Journal of thoracic and cardiovascular surgery, 2017. **153**(1): p. 8-20. e3.

113.   van Ooij, P., et al., *Aortic valve stenosis alters expression of regional aortic wall shear stress: New insights from a 4-dimensional flow magnetic resonance imaging study of 571 subjects.* Journal of the American Heart Association, 2017. **6**(9): p. e005959.

114.   Farzaneh, S., et al., *Identifying local arterial stiffness to assess the risk of rupture of ascending thoracic aortic aneurysms.* Annals of biomedical engineering, 2019. **47**(4): p. 1038-1050.

115.   Mousavi, S.J. and S. Avril, *Patient-specific stress analyses in the ascending thoracic aorta using a finite-element implementation of the constrained mixture theory.* Biomechanics and modeling in mechanobiology, 2017. **16**(5): p. 1765-1777.

116.   Rooprai, J., et al., *Thoracic aortic aneurysm growth in bicuspid aortic valve patients: role of aortic stiffness and pulsatile hemodynamics.* Journal of the American Heart Association, 2019. **8**(8): p. e010885.

117. Bersi, M.R., et al., *Novel methodology for characterizing regional variations in the material properties of murine aortas.* Journal of biomechanical engineering, 2016. **138**(7): p. 071005.

118. Khanafer, K.M., et al., *Modeling pulsatile flow in aortic aneurysms: effect of non-Newtonian properties of blood.* Biorheology, 2006. **43**(5): p. 661-679.

119. Leuprecht, A. and K. Perktold, *Computer simulation of non-Newtonian effects on blood flow in large arteries.* Computer Methods in Biomechanics and Biomedical Engineering, 2001. **4**(2): p. 149-163.

120. Agnese, V., et al., *Patterns of ascending aortic dilatation and predictors of surgical replacement of the aorta: A comparison of bicuspid and tricuspid aortic valve patients over eight years of follow-up.* Journal of Molecular and Cellular Cardiology, 2019. **135**: p. 31-39.

121. Di Giuseppe, M., et al., *Identification of circumferential regional heterogeneity of ascending thoracic aneurysmal aorta by biaxial mechanical testing.* Journal of Molecular and Cellular Cardiology, 2019. **130**: p. 205-215.

122. Choudhury, N., et al., *Local mechanical and structural properties of healthy and diseased human ascending aorta tissue.* Cardiovasc Pathol, 2009. **18**(2): p. 83-91.

123. Duprey, A., et al., *In vitro characterisation of physiological and maximum elastic modulus of ascending thoracic aortic aneurysms using uniaxial tensile testing.* Eur J Vasc Endovasc Surg, 2010. **39**(6): p. 700-7.

124. Okamoto, R.J., et al., *Mechanical properties of dilated human ascending aorta.* Ann Biomed Eng, 2002. **30**(5): p. 624-35.

125. Pham, T., et al., *Biomechanical characterization of ascending aortic aneurysm with concomitant bicuspid aortic valve and bovine aortic arch.* Acta Biomater, 2013. **9**(8): p. 7927-36.

126. Pichamuthu, J.E., et al., *Differential tensile strength and collagen composition in ascending aortic aneurysms by aortic valve phenotype.* Ann Thorac Surg, 2013. **96**(6): p. 2147-54.

127. Walraevens, J., et al., *Correlation between compression, tensile and tearing tests on healthy and calcified aortic tissues.* Medical engineering & physics, 2008. **30**(9): p. 1098-1104.

128. Fung, Y.-C., *Biomechanics: circulation.* Springer, 1998. **9**(2): p. 155.

129. Chirinos, J.A. and P. Segers, *Noninvasive evaluation of left ventricular afterload: part 1: pressure and flow measurements and basic principles of wave conduction and reflection.* Hypertension, 2010. **56**(4): p. 555-562.

130. Chirinos, J.A. and P. Segers, *Noninvasive evaluation of left ventricular afterload: part 2: arterial pressure-flow and pressure-volume relations in humans.* Hypertension, 2010. **56**(4): p. 563-570.

131. Laurent, S., P. Boutouyrie, and P. Lacolley, *Structural and genetic bases of arterial stiffness.* Hypertension, 2005. **45**(6): p. 1050-1055.

132. Mackenzie, I., I. Wilkinson, and J. Cockcroft, *Assessment of arterial stiffness in clinical practice.* Qjm, 2002. **95**(2): p. 67-74.

133. O'Rourke, M.F. and W.W. Nichols, *Aortic diameter, aortic stiffness, and wave reflection increase with age and isolated systolic hypertension.* Hypertension, 2005. **45**(4): p. 652-658.

134. Sokolis, D.P., et al., *Biomechanical response of ascending thoracic aortic aneurysms: association with structural remodelling.* Computer methods in biomechanics and biomedical engineering, 2012. **15**(3): p. 231-248.

135. Redheuil, A., et al., *Age-related changes in aortic arch geometry: relationship with proximal aortic function and left ventricular mass and remodeling.* Journal of the American College of Cardiology, 2011. **58**(12): p. 1262-1270.

136. LeMaire, S.A., et al., *Matrix metalloproteinases in ascending aortic aneurysms: Bicuspid versus trileaflet aortic valves1.* Journal of Surgical Research, 2005. **123**(1): p. 40-48.

137. Gallo, A., et al., *On the prospect of serum exosomal miRNA profiling and protein biomarkers for the diagnosis of ascending aortic dilatation in patients with bicuspid and tricuspid aortic valve.* International journal of cardiology, 2018. **273**: p. 230-236.

138. García-Herrera, C.M., et al., *Mechanical behaviour and rupture of normal and pathological human ascending aortic wall.* Medical & biological engineering & computing, 2012. **50**(6): p. 559-566.

139. Sokolis, D.P., et al., *A structural basis for the aortic stress–strain relation in uniaxial tension.* Journal of biomechanics, 2006. **39**(9): p. 1651-1662.

140. Mikich, B., *Dissection of the aorta: a new approach.* Heart (British Cardiac Society), 2003. **89**(1): p. 6-8.

141. Criado, F.J., *Aortic dissection: A 250-year perspective.* Texas Heart Institute Journal, 2011. **38**(6): p. 694-700.

142. Oberwalder, P.J., *Aneurysms and dissection of the thoracic aorta: definition and pathology.* Journal fur Kardiologie, 2001. **8**(1-2): p. 2-4.

143. Kouchoukos, N.T. and D. Dougenis, *Surgery of the thoracic aorta.* New England Journal of Medicine, 1997. **336**(26): p. 1876-1889.

144. Tam, A.S., M.C. Sapp, and M.R. Roach, *The effect of tear depth on the propagation of aortic dissections in isolated porcine thoracic aorta.* Journal of biomechanics, 1998. **31**(7): p. 673-676.

145. van Baardwijk, C. and M.R. Roach, *Factors in the propagation of aortic dissections in canine thoracic aortas.* Journal of biomechanics, 1987. **20**(1): p. 67-73.

146. Wolinsky, H. and S. Glagov, *A lamellar unit of aortic medial structure and function in mammals.* Circulation research, 1967. **20**(1): p. 99-111.

147. Auer, J., R. Berent, and B. Eber, *Aortic dissection: incidence, natural history and impact of surgery.* Journal of Clinical and Basic Cardiology, 2000. **3**(3): p. 151-154.

148. Trimarchi, S., et al., *Acute type B aortic dissection in the absence of aortic dilatation.* Journal of vascular surgery, 2012. **56**(2): p. 311-316.

149. Geest, J.P.V., et al., *Towards a noninvasive method for determination of patient-specific wall strength distribution in abdominal aortic aneurysms.* Annals of biomedical engineering, 2006. **34**(7): p. 1098-1106.

150. Rinaudo, A., et al., *Predicting outcome of aortic dissection with patent false lumen by computational flow analysis.* Cardiovascular Engineering and Technology, 2014. **5**(2): p. 176-188.

151. Haslach Jr, H.W., et al., *Comparison of aneurysmal and non-pathologic human ascending aortic tissue in shear.* Clinical Biomechanics, 2018. **58**: p. 49-56.

152. MacLean, N.F., N.L. Dudek, and M.R. Roach, *The role of radial elastic properties in the development of aortic dissections.* Journal of vascular surgery, 1999. **29**(4): p. 703-710.

153. Sommer, G., et al., *Dissection properties of the human aortic media: an experimental study.* Journal of biomechanical engineering, 2008. **130**(2): p. 021007.

154. Sommer, G., et al., *Mechanical strength of aneurysmatic and dissected human thoracic aortas at different shear loading modes.* Journal of biomechanics, 2016. **49**(12): p. 2374-2382.

155. Santamaría, V.A.A., et al., *Characterization of chemoelastic effects in arteries using digital volume correlation and optical coherence tomography.* Acta Biomaterialia, 2020. **102**: p. 127-137.

156. Wang, R.K. *Tissue clearing as a tool to enhance imaging capability for optical coherence tomography*. in *Coherence Domain Optical Methods in Biomedical Science and Clinical Applications VI*. 2002. International Society for Optics and Photonics.

157. Ahmadzadeh, H., M. Rausch, and J. Humphrey, *Modeling lamellar disruption within the aortic wall using a particle-based approach.* Scientific reports, 2019. **9**(1): p. 1-17.

158. Huang, Y.-P., et al., *An optical coherence tomography (OCT)-based air jet indentation system for measuring the mechanical properties of soft tissues.* Measurement science and technology, 2008. **20**(1): p. 015805.

159. Mahdian, M., et al., *Tissue characterization using optical coherence tomography and cone beam computed tomography: a comparative pilot study.* Oral surgery, oral medicine, oral pathology and oral radiology, 2016. **122**(1): p. 98-103.

160. Real, E., et al., *Optical coherence tomography assessment of vessel wall degradation in thoracic aortic aneurysms.* Journal of biomedical optics, 2013. **18**(12): p. 126003.

161. Roccabianca, S., G.A. Ateshian, and J.D. Humphrey, *Biomechanical roles of medial pooling of glycosaminoglycans in thoracic aortic dissection.* Biomechanics and modeling in mechanobiology, 2014. **13**(1): p. 13-25.

162. Yang, Y., et al., *Investigation of optical coherence tomography as an imaging modality in tissue engineering.* Physics in Medicine & Biology, 2006. **51**(7): p. 1649.

163. Huang, D., et al., *Optical coherence tomography.* science, 1991. **254**(5035): p. 1178-1181.

164. Tucker-Schwartz, J. and M. Skala, *Contrast enhancement in optical coherence tomography*. 2012, Citeseer.

165. Rogowska, J., et al., *Optical coherence tomographic elastography technique for measuring deformation and strain of atherosclerotic tissues.* Heart, 2004. **90**(5): p. 556-562.

166. Chu, T., W. Ranson, and M.A. Sutton, *Applications of digital-image-correlation techniques to experimental mechanics.* Experimental mechanics, 1985. **25**(3): p. 232-244.

167. Fu, J., F. Pierron, and P.D. Ruiz, *Elastic stiffness characterization using three-dimensional full-field deformation obtained with optical coherence tomography and digital volume correlation.* Journal of biomedical optics, 2013. **18**(12): p. 121512.

168. Palanca, M., G. Tozzi, and L. Cristofolini, *The use of digital image correlation in the biomechanical area: a review.* International biomechanics, 2016. **3**(1): p. 1-21.

169. Pan, B., et al., *Two-dimensional digital image correlation for in-plane displacement and strain measurement: a review.* Measurement science and technology, 2009. **20**(6): p. 062001.

170. Bruck, H., et al., *Digital image correlation using Newton-Raphson method of partial differential correction.* Experimental mechanics, 1989. **29**(3): p. 261-267.

171. Sutton, M.A., J.J. Orteu, and H. Schreier, *Image correlation for shape, motion and deformation measurements: basic concepts, theory and applications*. 2009: Springer Science & Business Media.

172. Genovese, K., et al., *Full-surface deformation measurement of anisotropic tissues under indentation.* Medical engineering & physics, 2015. **37**(5): p. 484-493.

173. Lecompte, D., et al., *Quality assessment of speckle patterns for digital image correlation.* Optics and lasers in Engineering, 2006. **44**(11): p. 1132-1145.

174. Trabelsi, O., et al., *Patient specific stress and rupture analysis of ascending thoracic aneurysms.* Journal of biomechanics, 2015. **48**(10): p. 1836-1843.

175. Acosta Santamaría, V.A., et al., *Three-dimensional full-field strain measurements across a whole porcine aorta subjected to tensile loading using optical coherence tomography–digital volume correlation.* Frontiers in Mechanical Engineering, 2018. **4**: p. 3.

176. Prokop, M., et al., *Use of maximum intensity projections in CT angiography: a basic review.* Radiographics, 1997. **17**(2): p. 433-451.

177. Blaber, J., B. Adair, and A. Antoniou, *Ncorr: open-source 2D digital image correlation matlab software.* Experimental Mechanics, 2015. **55**(6): p. 1105-1122.

178. Reu, P., *The Art and Application of DIC.* Experimental Techniques, 2015.

179. Avril, S., *Aortic and arterial mechanics.* Cardiovascular Mechanics, 2019.

180. Sun, C., et al., *Digital image correlation–based optical coherence elastography.* Journal of biomedical optics, 2013. **18**(12): p. 121515.

181. Tong, J., et al., *Gender differences in biomechanical properties, thrombus age, mass fraction and clinical factors of abdominal aortic aneurysms.* European journal of vascular and endovascular surgery, 2013. **45**(4): p. 364-372.

182. Purslow, P., *Measurement of the fracture toughness of extensible connective tissues.* Journal of Materials Science, 1983. **18**(12): p. 3591-3598.

183. Vaishnav, R.N., et al., *Nonlinear anisotropic elastic properties of the canine aorta.* Biophysical Journal, 1972. **12**(8): p. 1008-1027.

184. Réthoré, J., F. Hild, and S. Roux, *Extended digital image correlation with crack shape optimization.* International Journal for Numerical Methods in Engineering, 2008. **73**(2): p. 248-272.

185. Danto, M.I. and S.L.Y. Woo, *The mechanical properties of skeletally mature rabbit anterior cruciate ligament and patellar tendon over a range of strain rates.* Journal of Orthopaedic Research, 1993. **11**(1): p. 58-67.

186. Haut, R., *Age-dependent influence of strain rate on the tensile failure of rat-tail tendon.* Journal of Biomechanical Engineering 1983.

187. Pioletti, D.P. and L.R. Rakotomanana, *On the independence of time and strain effects in the stress relaxation of ligaments and tendons.* Journal of biomechanics, 2000. **33**(12): p. 1729-1732.

188. Fung, Y.-C., *Mechanical properties and active remodeling of blood vessels*, in *Biomechanics*. 1993, Springer. p. 321-391.

189.   Kritharis, E.P., et al., *Effects of aneurysm on the mechanical properties and histologic structure of aortic sinuses.* The Annals of thoracic surgery, 2014. **98**(1): p. 72-79.